LUND UNIVERSITY

Connecting CMR and Physiology

Expanding the capabilities of cardiovascular magnetic resonance in quantifying physiology

Seemann, Felicia

2019

Document Version:
Publisher's PDF, also known as Version of record

Link to publication

Citation for published version (APA):
Seemann, F. (2019). *Connecting CMR and Physiology: Expanding the capabilities of cardiovascular magnetic resonance in quantifying physiology*. [Doctoral Thesis (compilation), Department of Biomedical Engineering]. Department of Biomedical Engineering, Lund university.

Total number of authors:
1

Creative Commons License:
CC BY

General rights
Unless other specific re-use rights are stated the following general rights apply:
Copyright and moral rights for the publications made accessible in the public portal are retained by the authors and/or other copyright owners and it is a condition of accessing publications that users recognise and abide by the legal requirements associated with these rights.

- Users may download and print one copy of any publication from the public portal for the purpose of private study or research.
- You may not further distribute the material or use it for any profit-making activity or commercial gain
- You may freely distribute the URL identifying the publication in the public portal

Read more about Creative commons licenses: https://creativecommons.org/licenses/

Take down policy
If you believe that this document breaches copyright please contact us providing details, and we will remove access to the work immediately and investigate your claim.

LUND UNIVERSITY

PO Box 117
221 00 Lund
+46 46-222 00 00

Download date: 23. Jun. 2024

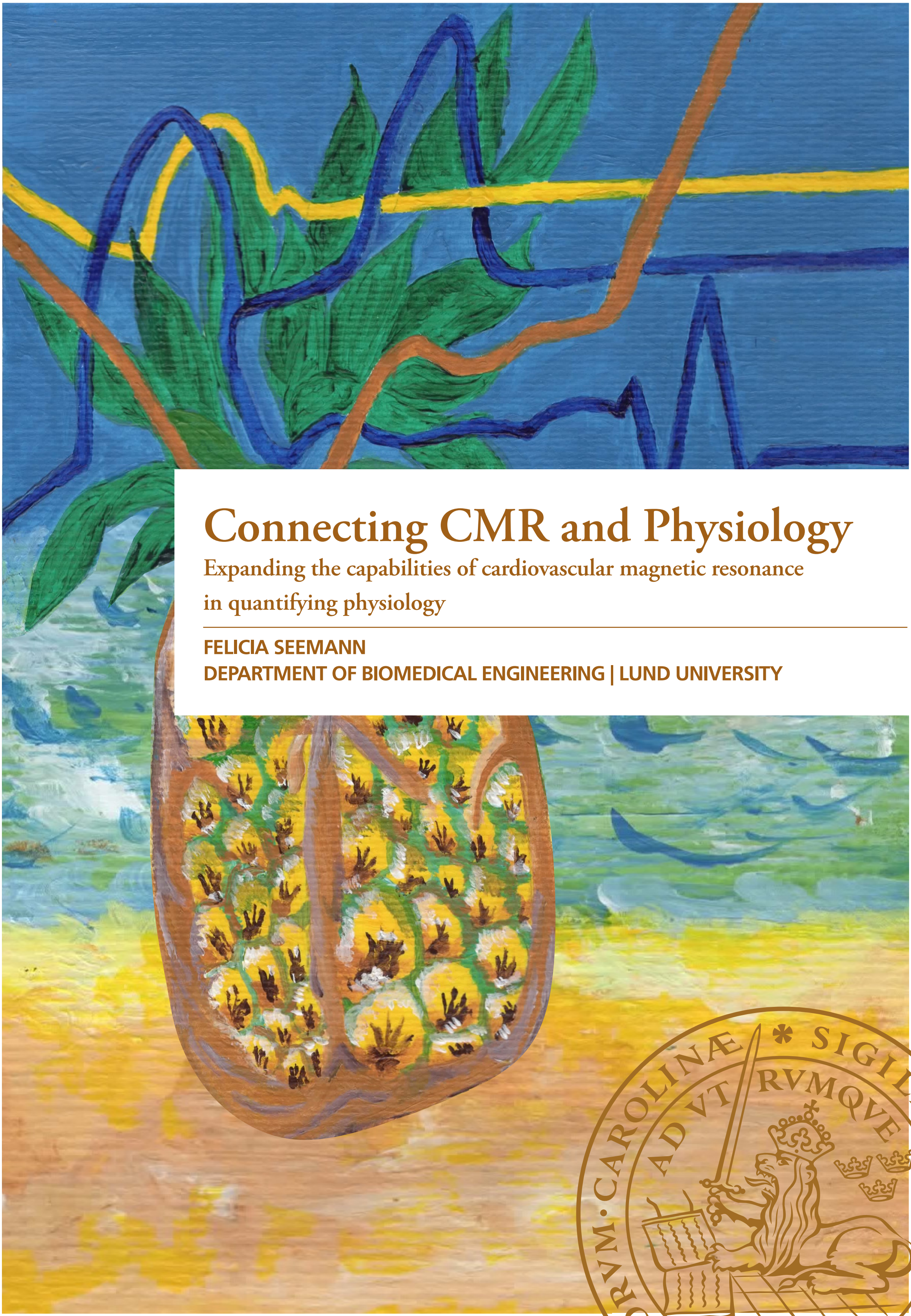

Connecting CMR and Physiology

Expanding the capabilities of cardiovascular magnetic resonance in quantifying physiology

FELICIA SEEMANN
DEPARTMENT OF BIOMEDICAL ENGINEERING | LUND UNIVERSITY

Connecting CMR and Physiology

Expanding the capabilities of cardiovascular magnetic resonance in quantifying physiology

Felicia Seemann

LUND
UNIVERSITY

Cover: *"Physiological Samba"*
Artist: Andrea Pettersson

© Felicia Seemann 2019

Typeset in LaTeX using a template by Berry Holl with modifications from Daniel Carrera

Lund University, Faculty of Engineering, Department of Biomedical Engineering
ISBN: 978-91-7895-328-8 (print), 978-91-7895-329-5 (pdf)
ISRN: LUTEDX/TEEM – 1120 – SE
Report-nr: 5/19

Printed in Sweden by Tryckeriet i E-huset, Lund University, Lund, Sweden, 2019

To my parents
–my father, who would sieze the day with his whole heart, always
–my mother, who just like thesis is *mais coração que carne e osso*

You are the foundation of everything I am and do. Thank you.

Contents

Preface iii

List of publications v

Abstract vii

Populärvetenskaplig sammanfattning ix

Resumo científico xi

Acknowledgements xiii

I Research context

1 Introduction 1
- 1.1 Cardiovascular physiology 2
- 1.2 Magnetic resonance imaging 15
- 1.3 Cardiovascular pressure measurements 20
- 1.4 Study motivations 23

2 Aims 25

3 Materials and methods 27
- 3.1 Study population 27
- 3.2 Cardiovascular magnetic resonance 28
- 3.3 Animal model 29
- 3.4 Pressure data analysis 29
- 3.5 Image analysis 30
- 3.6 Developed methods in this thesis 31
- 3.7 Statistical analysis 42

4 Results and comments 43
4.1 Study I: AV-plane displacement 43
4.2 Study II: Transmitral flow 47
4.3 Study III: Noninvasive pressure-volume loops 52
4.4 Study IV: Ventricular force-length loops 58

5 Conclusions 65

References 67

II Research papers

Author contributions 85

Errata 87

Study I: Time-resolved tracking of the atrioventricular plane displacement in Cardiovascular Magnetic Resonance (CMR) images 89

Study II: Valvular imaging in the era of feature-tracking: A slice-following CMR sequence to measure mitral flow 109

Study III: Noninvasive Quantification of Pressure-Volume Loops From Brachial Pressure and Cardiovascular Magnetic Resonance 127

Study IV: Longitudinal and radial forces in ventricular pumping mechanics and their contribution to stroke work 147

Preface

The work resulting in this thesis was performed at the Department of Biomedical Engineering, Faculty of Engineering, and the Department of Clinical Physiology, Medical Faculty, at Lund University in Lund, Sweden. Main supervisor was Associate Professor Einar Heiberg, Associate Professor Marcus Carlsson was co-supervisor, and colleagues in the Lund Cardiac MR group provided continuous guidance, feedback, interesting discussions, and invaluable reflections.

A six month research exchange under the supervision of Associate Professor Dana C. Peters and Assistant Professor Lauren A. Baldassarre was conducted at the Magnetic Resonance Research Center, Department of Radiology and Biomedical Imaging, at Yale University in New Haven, Connecticut, USA.

The studies and work in this thesis were funded by the Swedish Research Council, the Swedish Heart Lung Foundation, ALF Medical Faculty grants at Lund University, the European Commission within the 7th Framework Program for RTD, Novo Nordisk, the Swedish Heart Association, the Wallenberg Centre for Molecular Medicine at Lund University and Skåne University Hospital, VINNOVA, Medtech4Health, the National Institutes of Health, the 2017 ISMRM research exchange program, the Scandinavian Society of Clinical Physiology and Nuclear Medicine, the Swedish Society of Medical Research, Maggie Stephens Foundation, the Swedish Medical Association, Ernhold Lundströms Foundation, and the Swedish Society for Clinical Physiology.

List of publications

This thesis is based on the following studies:

I **Time-resolved tracking of the atrioventricular plane displacement in Cardiovascular Magnetic Resonance (CMR) images**

F. Seemann, U. Pahlm, K. Steding-Ehrenborg, E. Ostenfeld, D. Erlinge, J-L. Dubois-Rande, S. Eggert Jensen, D. Atar, H. Arheden, M. Carlsson, E. Heiberg
BMC Med Imaging, 2017. doi: 10.1186/s12880-017-0189-5.

II **Valvular imaging in the era of feature-tracking: A slice-following CMR sequence to measure mitral flow**

F. Seemann, E. Heiberg, M. Carlsson, R. A. Gonzales, L. A. Baldassarre, M. Qiu, D. C. Peters
J Magn Reson Imaging, 2019. doi: 10.1002/jmri.26971. In press.

III **Noninvasive Quantification of Pressure-Volume Loops From Brachial Pressure and Cardiovascular Magnetic Resonance**

F. Seemann, P. Arvidsson, D. Nordlund, S. Kopic, M. Carlsson, H. Arheden, E. Heiberg
Circ Cardiovasc Imaging, 2019. doi: 10.1161/circimaging.118.008493.

IV **Longitudinal and radial forces in ventricular pumping mechanics and their contribution to stroke work**

F. Seemann, J. Berg, K. Solem, R. Jablonowski, H. Arheden, M. Carlsson, E. Heiberg
Manuscript.

Abstract

The assessment of cardiovascular physiology is crucial to facilitate clinical diagnostics, treatment, and research. Physiology and anatomy can be assessed noninvasively using cardiovascular magnetic resonance (CMR), a versatile and reliable medical imaging modality free from ionizing radiation. CMR is capable of providing a vast amount of information such as displacement, velocity, flow, length, area, volume, and tissue properties. Considered the gold standard for noninvasive quantification of cardiac function and morphology, CMR is increasingly envisioned as a future one-stop-shop imaging examination for cardiovascular disease. However, quantification of important physiological aspects such as valvular motion, pressure, and force are still not accessible or readily available when using CMR.

The general aim of this thesis was therefore to expand the current capabilities of CMR to include new reliable methods and tools for quantification of the atrioventricular plane displacement, transmitral flow, pressure, and ventricular force-length loops, hence allowing a more complete assessment of subject-specific cardiovascular physiology that could potentially be achieved in a single noninvasive examination.

In this thesis, the current capabilities of CMR were expanded by developing and validating four new methods for quantification of physiology. In Study I, an imaging processing algorithm for feature-tracking of the atrioventricular plane displacement was proposed. The combination of this algorithm and a phase contrast CMR sequence was proposed in Study II to improve measurements of transvalvular flow, which are challenging due to the significant movement of the atrioventricular valves over the cardiac cycle. In Study III, CMR imaging, a noninvasive brachial pressure, and mathematical modelling was combined to enable a noninvasive quantification of left ventricular pressure-volume loops. Study IV used the atrioventricular plane displacement algorithm and the noninvasive pressure-volume loop technique to propose a novel method for evaluation of ventricular force-length loops, which was used to describe the energetics of longitudinal and radial pumping mechanics.

The proposed methods in Study I, II, and IV require only brachial pressure and images which are typically acquired during standard clinical CMR scanning. Addition of the sequence in Study II would prolong a CMR protocol by a few minutes, suggesting that the capabilities of CMR to evaluate cardiovascular physiology during a single noninvasive examination have been expanded, thus getting closer to the one-stop-shop vision for CMR.

Populärvetenskaplig sammanfattning

Hjärt-kärlsjukdom är den vanligaste dödsorsaken i världen. Tidig diagnos och individanpassad vård är viktigt för att kunna behandla hjärtsjuka patienter. Ny teknik kan möjliggöra framtagandet av nya och förbättrade underlag som behövs för diagnos och behandlingsplan av många hjärtsjuka patienter. Därför har nya analysverktyg som utökar mängden fysiologisk information som går att utvinna ur en enda medicinsk undersökning av hjärtat tagits fram. Detta kan potentiellt förbättra individanpassad vård och forskning då diagnostik, behandlingsplaner och forskningsundersökningar kan genomföras vid ett och samma tillfälle.

Magnetkameror kan användas för att ta medicinska bilder inuti kroppen med hög kvalitet utan varken kirurgiska ingrepp eller strålning. Hjärtbilder tagna med magnetkameror kan används för att utvärdera hjärtats anatomi och pumpförmåga. Utvärderingen sker med hjälp av datorprogram som bland annat kan mäta volymer, förskjutning, hastighet och blodflöden. Den tekniska utvecklingen har hittills inte tillåtit mätning av en del viktig information ur bilderna, som till exempel tryck och kraft. En annan utmaning har varit bildtagning av hjärtklaffarna eftersom de rör sig fram och tillbaka under hjärtslaget.

I denna avhandling har fyra nya metoder för att mäta kardiovaskulär fysiologi utifrån magnetresonansbilder av hjärtat utvecklats och verifierats. I första studien utvecklades ett verktyg som kan detektera och mäta hjärtklaffarnas rörelsemönster. I den andra studien kombinerades detta verktyg med en ny bildtagningsmetod för att kunna mäta blodflödet genom klaffarna. För att kunna få information om hur tryck och volym varierar över hjärtcykeln framställdes en ny metod som kombinerar bildanalys och matematisk modellering. I den fjärde och sista studien möjliggjordes utvärderingen av krafter som verkar i hjärtkammaren, som i sin tur kan användas för att beräkna olika aspekter av hur hjärtat förbrukar energi.

En magnetkameraundersökning tar i dagsläget ca 40-60 minuter. Bilderna som används i tre av studierna är sådana som samlas rutinmässigt, och att lägga till den nya bildtagningsmetoden framtagen i den andra studien utökar endast undersökningstiden med ett par minuter.

Tillsammans utvidgar dessa nya verktyg magnetkamerans förmåga för bedömningar av hjärtat utan att nämnvärt utöka undersökningstiden, vilket innebär att vi närmar oss verkligheten av en mer tidseffektiv, omfattande och individanpassad diagnostik av hjärtkärl-sjukdomar.

Resumo científico

A diversidade de informações sobre a fisiologia cardiovascular que podem ser avaliadas em um único exame de imagem está constantemente expandindo. Isso tem potencial para aprimorar tanto o tratamento dos pacientes quanto a aplicação no campo da pesquisa científica, pois os diagnósticos, os planejamentos dos tratamentos e as pesquisas poderão ser efetuados em uma única aquisição de exame.

A ressonância magnética é um método de imagem médica versátil que gera imagens de alta qualidade sem intervenções invasivas ou radiação ionizante. Na medicina cardiovascular, essas imagens podem ser usadas para avaliar a morfologia e o batimento cardíaco. A avaliação é feita com a ajuda de programas de computador e algoritmos que podem, entre outras coisas, medir volumes, deslocamento, velocidades e fluxo sangüíneo, além de detectar várias propriedades do tecido, como edema e fibrose.

Até o presente momento, os desenvolvimentos tecnológicos não tornaram possível a extração de algumas importantes informações fisiológicas das imagens, como por exemplo a quantificação da pressão e força. Outro desafio tem sido retratar as válvulas cardíacas, por causa de seu movimento durante o batimento cardíaco.

Nesta tese, quatro novos métodos para medir a fisiologia cardiovascular baseados em imagens de ressonância magnética cardíaca foram desenvolvidos e validados. No primeiro estudo, um algoritmo que pode medir o movimento das válvulas cardíacas foi desenvolvido. No segundo estudo, este algoritmo foi combinado com um novo método de aquisição de imagens para medir o fluxo sanguíneo através das válvulas. No estudo III, para extrair informações sobre como a pressão e o volume variam ao longo do ciclo cardíaco, combinou-se um método de análise de imagens com modelagem matemática. O quarto e último estudo permitiu a avaliação das forças que atuam dentro do ventrículo, as quais podem ser usadas para calcular o consumo de energia dos mecanismos de bombeamento do coração.

Um exame padrão de ressonância magnética cardíaca dura cerca de 40 a 60 minutos. As imagens usadas nos estudos I, III e IV já são coletadas em exames de rotina. Apenas poucos minutos são acrescentados ao tempo total do exame para a utilização do novo método de aquisição de imagens desenvolvido no segundo estudo.

Juntos, esses novos métodos ampliam a capacidade da ressonância magnética cardíaca, potentialmente possibilitando um diagnóstico individualizado mais abrangente e eficiente para doenças cardiovasculares.

Acknowledgements

There is much more behind this thesis than research and work. Its foundation lies in all encouragement, help, support, feedback, and questions I have received throughout the years. I am grateful for all of it, and would like to extend my special gratitude to the following:

My supervisors. **Einar Heiberg** for being a supportive and amazing supervisor. Your positivity and can-do attitude inspire and motivate me every time we talk. **Marcus Carlsson** for patiently teaching me physiology, never letting me get away without answering the hard questions, and helping me focus on the why. **Dana Peters** for teaching and encouraging me so much. Your genuine excitement about science and research inspire me every day. **Lauren Baldassarre**, for your enthusiastic mentorship that has opened up and improved my world. **Gustaf Söderlind** for encouraging me to go into research in the first place.

My colleagues. **Håkan Arheden** for tirelessly teaching me how to think, communicate, accept, and reflect. **Katarina Steding-Ehrernborg**, you have been my idol since the day I first met you. **Anthony Aletras** for all help and career coaching. **Ellen Ostenfeld**, for your contagious eagerness. **Erik Hedström**, pushing the time one can spend at the lounge is the most fun with you. **Henrik Engblom**, for always carrying that huge smile of yours. **Johannes Töger**, my wonderful role model for over a decade who now is an even more wonderful friend. **Mariam Al-Mashat** for all late night texting and moral support. **Ulrika Pahlm** for AV teamwork at its best. **David Nordlund**, the best neighbour I have ever had. **Jane Tufvesson**, for always helping me feel good about myself. **Per Arvidsson** for invaluable help with physiology, graphics, and quests for the perfect reference. **Jonas Liefke**, for not being afraid to suggest and organize new ideas. Everyone in the **Lund Cardiac MR Group**, **Medviso**, and **Syntach** for personal and professional development. It's been so much fun!

The coolest of friends. **Lisa**, **Andrea**, **Astrid**, and **Sofia**, for pumpkins, sauna, ice poles, cheese rolling, and more. **Hanna**, for being willing to burn no matter how far. **Malin**, for ensuring Thursdays at Retro before 19.00 and Monday tapas continues to happen. **Ferm** and **Björn**, you light up my world (like the 4th of July). **Teresia**, for IKEA and farm life. **Anna**, **Aninha**, **Rafa**, **Sarah**, and **Camila**, for keeping close despite the distance. **Lizzie, Eli, Nick, Josh, Vlad**, and **Kate**, my New Haven life would not have been the same without you.

My loving and supportive family. My parents **Michael** and **Luciene**, for simply everything. **Fredrik** and **Vix**, for cheering on me and my projects. I love that we are always a team. My grandmother **Liss**, for love and prioritizing to spend time with me. **Åsa** and **Andrea**, for sticking with us in sickness and health. **Mette** and **Tina**, for early on teaching me the true value and reasonable dosage of *vaniljsås*. **Keppas**, you coming to Skåne has brought me more joy than you could ever imagine. **Vovó Helena**, **Natália**, **Alexandre**, **Flávio**, **Lívia**, **Tadeu**, **Olívia**, e **Abaete**, obrigada por sempre me receber com amor e carinho, me proporcionar um segundo lar, e por terem me mostrado o valor da educação desde cedo. **Göran, Kerstin, Anna**, and **Petter**, for welcoming me into your family with open arms, and for sharing the best car parking experience ever with me.

Martin, my favourite person in the whole wide world. Thank you for our eventful high-speed up-side-down kind of life. I love you.

Lund, October 22nd 2019

Part I

Research context

Chapter 1

Introduction

> *Nothing in life is to be feared, it is only to be understood.*
> *Now is the time to understand more, so that we may fear less.*
>
> Marie Curie

Originating from ancient Greek, the word physiology means *the study of nature* and is the science of normal functions which sustain living systems. The word engineering is derived from Latin meaning *clever inventiveness*, and refers to the process of applying mathematics and natural sciences to develop novel or improved solutions to problems. One way of solving the problem of how to safely and reliably assess physiology can be to engineer new quantitative methods or tools. When developing such tools, it is just as important to understand the applied technology intended to solve the problem, as it is to understand the underlying physiological principles of the quantitative assessment itself.

With cardiovascular disease being the number one cause of death globally [1], the assessment of cardiovascular physiology is of great importance for both clinical and research purposes. For evaluation of cardiac function, physicians seek information on physiology and its interaction with anatomy. Examples of such sought information include the physical quantities of displacement, velocity, flow, length, area, volume, pressure, stiffness, force, and cardiovascular tissue properties acting within a specific anatomy. Over the last decades, cardiovascular magnetic resonance (CMR) imaging has emerged as a versatile and reliable clinical tool to assess such information.

CMR is already considered the gold standard for noninvasive quantification of cardiac function and morphology [2], and is increasingly envisioned as a future one-stop-shop cardiac imaging examination [3–5]. However, quantification of important physiological information such as longitudinal function and intracardiac pressure are still not accessible or readily available when using CMR. In this thesis, the intersection of physiology and engineering is therefore explored with the purpose of expanding the current capabilities of CMR in assessing cardiovascular physiology, thus getting closer to the reality of CMR as a one-stop-shop cardiovascular examination.

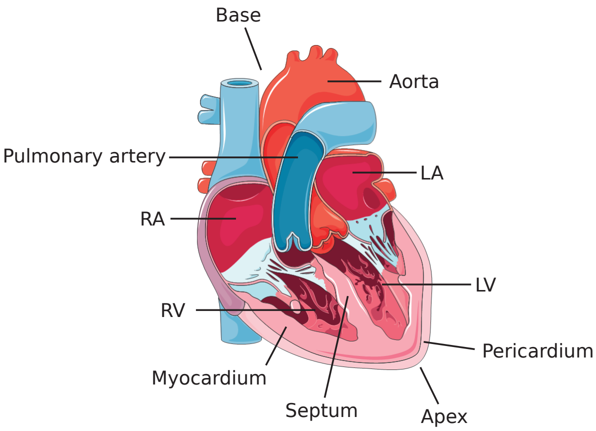

Figure 1.1: Schematic overview of the heart. RA, right atrium; RV, right ventricle; LA, left atrium; LV, left ventricle. *Image modified and used with permission from Servier Medical Art - Creative Commons Attribution 3.0 Unported Licence.*

1.1 Cardiovascular physiology

In order to function the body consumes oxygen and nutrients, and emits waste products such as carbon dioxide. These substances are transported by the blood via the circulatory system. Blood circulation is facilitated by the heart, a muscular organ that functions as a pump in order to supply enough blood volume over time as the metabolism demands. This demand is about 5 l/min at rest and up to 25 l/min during exercise [6, 7], and the cardiovascular system is designed to deliver this constantly over a lifetime.

1.1.1 The heart and the circulatory system

The human heart is located in the middle of the chest, slightly angled to the left. It is surrounded by the lungs and diaphragm, and enclosed by the pericardium. The pericardium is a double-layered, rubber-like fibrous sac surrounding the heart and its connected vessels, and is attached to the diaphragm and sternum [8]. The cavity between the pericardial layers contains pericardial fluid, which functions as a lubricant to suppress friction of the beating heart [9]. The top boundary of the heart points towards the head and is called the base, and the bottom boundary pointing towards the feet is called the apex. The apex and the base are essentially stationary over the heartbeat [10].

Between the base and the apex, the myocardium forms four chambers: two atria and two ventricles (Figure 1.1) which are separated by the atrioventricular (AV) plane, a fibrous plate containing the four cardiac valves (Figure 1.2).The valves are designed to allow one-way flow, and by opening and closing they govern the blood flow in and out of the ventricles. The left and the right side of the heart share a wall called a septum.

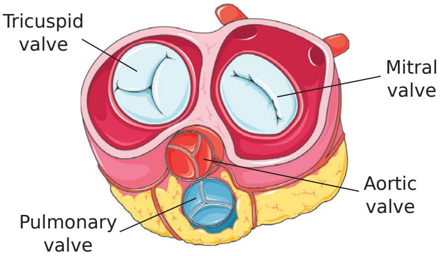
Tricuspid valve
Mitral valve
Aortic valve
Pulmonary valve

Figure 1.2: Illustration of the atrioventricular plane, in which the four cardiac valves are inserted. *Image modified and used with permission from Servier Medical Art - Creative Commons Attribution 3.0 Unported Licence.*

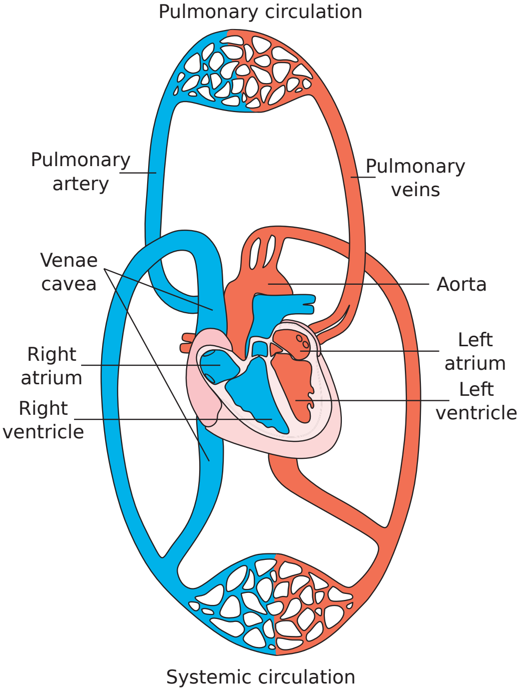
Pulmonary circulation
Pulmonary artery
Pulmonary veins
Venae cavea
Aorta
Left atrium
Right atrium
Left ventricle
Right ventricle
Systemic circulation

Figure 1.3: Schematic overview of cardiac anatomy and the circulatory systems. Oxygenated blood is represented in red and oxygen-depleted blood in blue. *Image modified and used with permission from Servier Medical Art - Creative Commons Attribution 3.0 Unported Licence.*

The circulatory system is a closed loop (Figure 1.3), a fact that was first described by William Harvey in 1628 [11]. Oxygen-depleted blood from the body flows to the heart via the superior and inferior caval veins and into the right atrium (RA). Blood from the RA flows through the tricuspid valve into the right ventricle (RV). The RV pumps blood through the pulmonary valve to the pulmonary circulation, where exchange of carbon dioxide and oxygen occurs. Oxygenated blood from the lungs returns via the pulmonary veins into the left atrium (LA), which flows through the mitral valve into the left ventricle (LV). The LV pumps blood across the aortic valve to the systemic circulation, ensuring blood supply to the body. Blood supply to the heart itself is secured via the coronary arteries which branch off from the aortic root.

1.1.2 Cardiac pumping mechanics

As any other fluid, blood complies with the laws of physics, and blood flow can be described as a driving pressure overcoming vascular resistance. This relation can be expressed in analogy with Ohm's Law as

$$R = \frac{\Delta P}{Q}$$

where Q denotes flow and ΔP is the pressure gradient over a resistance R. The systemic vascular resistance is about five-fold the pulmonary vascular resistance, meaning that the LV must generate five times more pressure than the RV. As a result, the myocaridial wall is significantly thicker in the LV than in the RV.

The myocardial wall is composed of layered muscle fibers called myocytes. The epicardium is the outermost surface of the heart, and the endocardium is the innermost layer of the cardiac chambers. The myocyte fiber orientation transitions continuously in helical structures from the apex to the base as well as from the epicardium to the endocardium [12–14]. The angulation of the epicardial and endocardial fibers are predominantly longitudinal in the apical-basal direction, while the midwall fibers are predominantly circumferentially oriented [15, 16], see Figure 1.4.

Electrical impulses generated in a region of the heart called the sinus node result in myocyte contraction. Each myocyte contracts in the direction in which it is aligned in the myocardium, and the coupling of all myocytes within the complex fiber structure results in a global ventricular shortening [12]. The combination of this fiber orientation and the shortening when the myocytes contract results in tension, pressure build-up, and tissue displacement [14]. A macroscopic way of describing ventricular shortening is by considering each myocyte as a contractile element represented as a vector with a length and a direction [17, 18]. By summing all vectors and decomposing them into two perpendicular components along the cardiac long-axis and short-axis, the overall ventricular shortening can be described as either longitudinal or radial.

Due to the predominantly longitudinal fiber orientation, the dominating effect of ventricular contraction is the displacement of the AV-plane [19, 20]. As the AV-plane moves

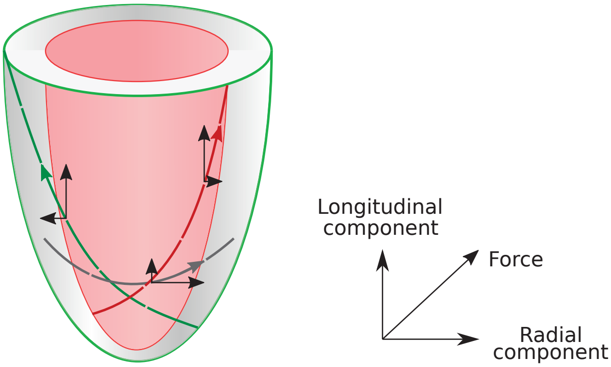
Longitudinal component
Force
Radial component

Figure 1.4: Schematic overview of a left ventricle represented as an ellipsoid. The epicardial (green), endocardial (red), and circumferential (gray) fiber bands and their contracting force decomposition into a longitudinal and radial components are illustrated with arrows.

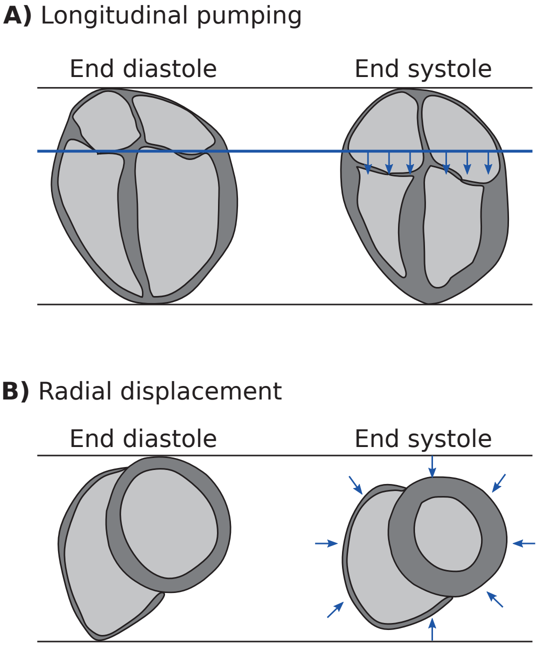
A) Longitudinal pumping
End diastole
End systole
B) Radial displacement
End diastole
End systole

Figure 1.5: Illustration of longitudinal and radial pumping mechanics. A) Longitudinal pumping refers to the atrioventricular plane displacement (blue arrows). While the apex and the base are essentially stationary (black horizontal lines), the valves descends towards the apex in systole, resulting in thickening of the myocardial wall. B) Radial pumping refers to the epicardial displacement, resulting in the slight change of epicardial radius when observing the ventricles in a short-axis view. The atrioventricular plane displacement is significantly larger than the epicardial displacement.

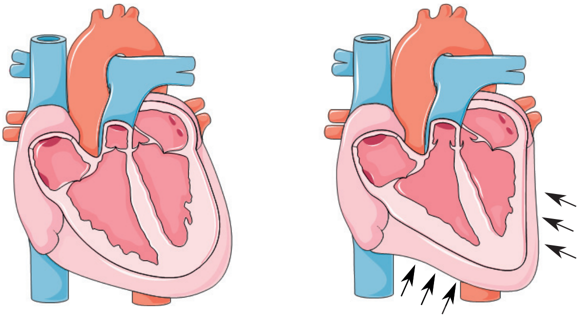

Figure 1.6: Common but incorrect illustration of cardiac pumping. The heart if often represented in an elliptical shape at end diastole (right), and transformed into a v-shaped morphology at end systole (left, indicated by black arrows). This pumping would results in a significant change of the outer boundaries of the heart. Also note that the cardiac valves are incorrectly represented at the same position. *Image modified and used with permission from Servier Medical Art - Creative Commons Attribution 3.0 Unported Licence.*

towards the essentially stationary apex, the ventricle shortens and pumps blood to the great vessels. Simultaneously, the fixated base results in lengthening and thus suction filling of the atria [21, 22]. As an analogy, consider the longitudinal pumping by shortening as a piston pump, while the atrial filling by suction as a syringe. Hence, longitudinal pumping facilitates filling and ejection of blood at the same time [23]. This process does however not result in a change of the total heart volume or epicardial displacement, which is instead accounted for by the radial pumping, see Figure 1.5.

The AV-plane displacement also results in a thickening of the myocardial wall, which during contraction will bulge in towards the ventricular lumen [10, 24]. This can be compared to flexing the biceps, where a longitudinal shortening will result in a thickening of the upper arm. Hence, if only observed in the short-axis perspective, it is easy to misinterpret the heart of having a predominantly squeezing pumping in the radial direction with a significant epicardial displacement and total heart volume variation as a result. In fact, although longitudinal pumping was described already by Leonardo da Vinci [25], this perception of a squeezing radial pumping is widespread, and several educational textbooks represent a beating heart that has a large total volume variation and with the apex moving in the longitudinal direction rather than the AV-plane [6, 26], see Figure 1.6.

This perception can probably be traced to open heart surgery, during which irregular motion is observed when the pericardium and other surrounding tissues in the thorax does not constrain the cardiac movement [27]. Noninvasive examinations in the intact chest have however shown that the total heart volume only varies 5-11% over the cardiac cycle [23, 28], and that the AV-plane displacement accounts for 60% of the LV and 80% of the RV stroke volume [10, 29]. Hence, longitudinal pumping is the main contributor to cardiac function and a reduced AV-plane displacement has been shown to be an independent predictor of adverse cardiac events and mortality [30, 31].

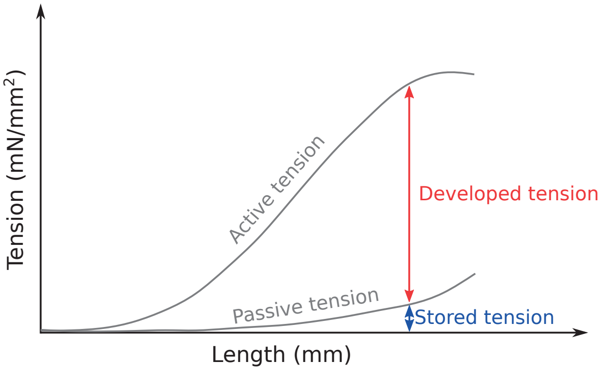

Figure 1.7: Schematic illustration of the active and passive tension in a myocardial fiber depending on its initial length before contraction. The passive tension at a given length can be interpreted as the stored tension in the myocyte at the beginning of contraction, while the difference in active and passive tension is the developed tension.

1.1.3 Myocardial tension

Both longitudinal and radial pumping mechanics is the result of contracting myocytes. The work performed by the contracting myocyte is a function of initial myocardial fiber length, and is bounded by an active and a passive tension generating component [32]. Passive tension describes the development of tension due to the stretching of the myocardium. The passive tension curve is non-linear, meaning that the increase in tension will be larger depending on the initial fiber length [33], similar to the exponential increase in tension in a balloon as it is being filled with air. On the other hand, myocyte contraction also generates an active tension, where the developed contractile force will be stronger the longer the myocardial fibers are stretched [34, 35]. This relationship does however only hold until a certain level of stretching, where the contractile capacity of the myocytes decreases, similar to an overextend rubber band [32]. The difference in these active and passive tension states describes total developed tension F in a myocyte (Figure 1.7) [36]. The amount of work W performed is calculated as

$$W = \int F \cdot dL$$

over the entire cardiac cycle, where dL is the myocardial fiber shortening relative to the initial length, which is called preload. Together, the intrinsic mechanisms of active and passive tension enable the heart to adapt its contractile force, and thereby the amount of blood it pumps, depending on the venous return. This ability of the heart to pump the amount of blood volume it receives is named the Frank-Starling mechanism, after the independent work by Otto Frank in 1895 and Ernest Starling in 1914 [37–39]. The amount of blood pumped will also depend on the afterload, i.e. the load the heart is pumping against, often quantified as the pressure in the great vessels.

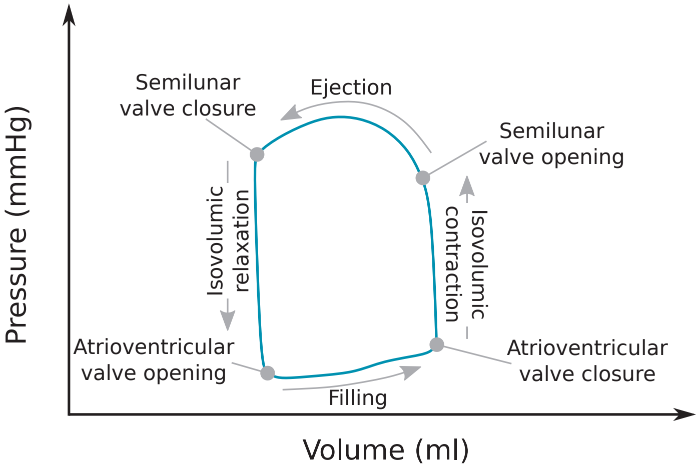
Pressure (mmHg)
Volume (ml)
Semilunar valve closure
Ejection
Semilunar valve opening
Isovolumic relaxation
Isovolumic contraction
Atrioventricular valve opening
Atrioventricular valve closure
Filling

Figure 1.8: Schematic illustration of the cardiac cycle in a ventricular pressure-volume loop. The pressure-volume loop is interpreted moving counter-clock wise, starting with end diastole which occurs in the bottom right corner at the closure of the atrioventricular valves.

When observing a cardiac chamber as a whole, the force-length relationship is extended and studied as the more easily quantified pressure-volume relationship

$$W = \int F \cdot dL = \int \frac{F}{A} \cdot (dL \cdot A) = \int P \cdot dV$$

where A is area, P is pressure, and dV the change in volume. The pressure-volume (PV) loop is a powerful functional representation of cardiac pumping as it provides energetic information of the performed work, contains information of myocardial stiffness and compliance, and enables a comprehensive overview of the cardiac cycle [36, 40–42].

1.1.4 The cardiac cycle

The cardiac cycle is the continuous and periodic process of emptying and filling of the cardiac chambers in order to pump blood and is divided into two main phases, systole and diastole. During systole the ventricles contract, thus ejecting blood into the systemic and pulmonary circulation through the semilunar valves, i.e. the aortic and tricuspid valves. Ventricular relaxation and filling occur during diastole. End diastole denotes the point of time where the ventricles are filled at their maximum and the atrioventricular valves, i.e. the mitral and tricuspid valve, close. End diastole is often the starting point when describing the cardiac cycle. The following sections describe the cardiac cycle, which is also illustrated by a ventricular PV loop in Figure 1.8 and as a modified Wiggers diagram in Figure 1.9.

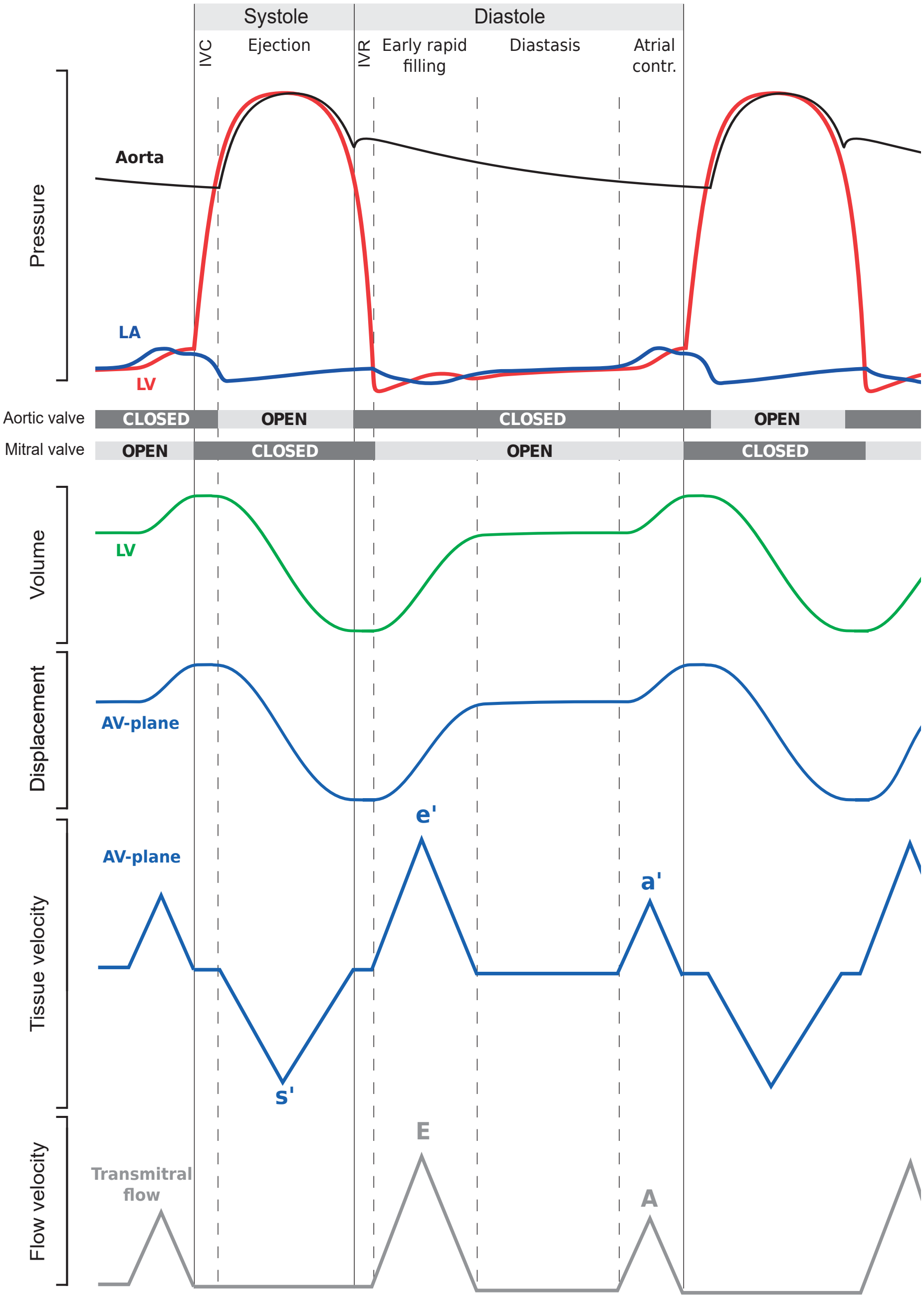
Systole
Diastole
IVC
Ejection
IVR
Early rapid filling
Diastasis
Atrial contr.
Pressure
Aorta
LA
LV
Aortic valve
CLOSED
OPEN
CLOSED
OPEN
Mitral valve
OPEN
CLOSED
OPEN
CLOSED
Volume
LV
Displacement
AV-plane
Tissue velocity
AV-plane
e'
a'
s'
Flow velocity
Transmitral flow
E
A

Figure 1.9: Schematic illustration of the variation in pressure, volume, atrioventricular (AV) plane displacement, AV-plane velocity, and AV-valve flow velocity in the left side of the heart over the cardiac cycle. IVC, isovolumetric contraction; IVR, isovolumetric relaxation. *Adapted with permission from Per Arvidsson [43].*

Systole

Isovolumetric contraction is the first phase of systole, which begins with filled ventricles and the closure of the atrioventricular valves. As the ventricles start contracting, the volume will remain constant since both the atrioventricular and semilunar valves are closed, resulting in a fast increase in pressure. The ventricular volume at this phase is called the end-diastolic volume (EDV).

Ejection starts when the pressure in the ventricles exceeds the pressure in the great vessels, resulting in the opening of the semilunar valves. The ventricular contraction pulls the AV-plane down towards the apex, a movement that simultaneously aids ventricular ejection and atrial filling [22]. The peak AV-plane velocity during the ejection is denoted s'. As blood is being ejected, the volume decreases, but the ventricles are still contracting and pressure continues to increase until peak ejection. At the peak ejection, the pressure in the great vessels exceeds the ventricular pressures, and is the point of time when the maximum blood flow velocity is passing through the semilunar valves. Blood will continue to flow after this event due to the inertia of the blood, but will decelerate [44]. The deceleration of blood eventually leads to a small backward flow of blood which forces the semilunar valves to close. The closure of the semilunar valves denotes end systole, and is the point of time when the ventricular volume is at its smallest, the AV-plane displacement is at its maximum distance from its initial position, and the atrial volume is at its largest. The ventricular volume at end systole is called the end-systolic volume (ESV).

Diastole

Isovolumetric relaxation is the first phase of diastole. With both the atrioventricular and the semilunar valves closed the ventricles starts to relax, which results in a maintained ventricular volume but fast decrease in pressure.

Early rapid filling is initiated when the pressure in the atria exceeds the pressure in the ventricles, resulting in the opening of the atrioventricular valves. A rapid inflow of blood from the atria to the ventricles follows. Simultaneously, the AV-plane ascends back towards the base [45–47]. Hence, ventricular filling is both driven by the blood pressure difference between the atrium and the ventricle, as well as by a passive transfer of blood volume as the AV-plane moves superiorly towards the heart base, causing atrial blood to be shuttled into the ventricle [48]. The blood flow velocity profile in this phase is called the E-wave, from which the peak blood flow velocity E and the peak AV-plane velocity e' can be appreciated.

Diastasis is the physiological equilibrium of ventricular volume, forces and flow [49]. In this phase, very little blood flows through the atrioventricular valves and the AV-plane remains essentially still. The duration of diastasis becomes shorter with an increase in heart rate, eventually resulting in a merge of the early rapid filling and the atrial contraction [50, 51].

Atrial contraction occurs towards the end of ventricular diastole, during which a small increase in atrial pressure will cause blood flow through the atrioventricular valves [52].

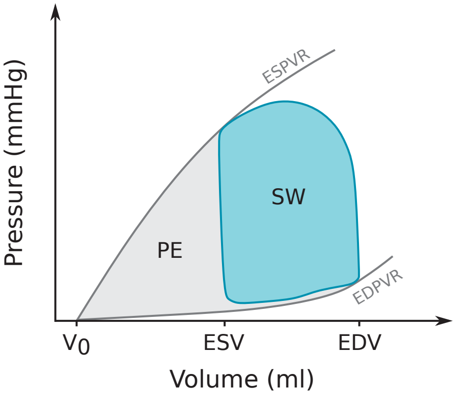

Figure 1.10: Schematic illustration of derivable hemodynamic parameters from a ventricular pressure-volume loop. PE, potential energy; SW, stroke work; ESV, end-systolic volume; EDV, end-diastolic volume; $ESPVR$, end-systolic pressure volume relationship; $EDPVR$, end-diastolic pressure volume relationship; V_0, ventricular volume at zero pressure.

A passive transfer of blood will also occur as the AV-plane is pulled up to its initial basal position [10, 29, 48]. Ventricular pressures will subsequently exceed atrial pressures, which after a short delay due to the inertia of blood, results in the closure of the atrioventricular valves. This valve closure denotes end diastole [26], thus concluding the cardiac cycle. The blood flow velocity profile in this phase is called the A-wave, from which the peak blood flow velocity A and the peak AV-plane velocity a' can be appreciated.

Hemodynamic parameters

When assessing cardiac function, different hemodynamic parameters are studied to aid in the overall subject evaluation. Many important hemodynamic parameters can be derived from the PV loop, see Figure 1.10. Information on EDV and ESV can be read on the x-axis in the PV loop representation. These values allow for calculation of the amount of ejected blood, i.e. the stroke volume (SV)

$$SV = EDV - ESV$$

as well as the ejection fraction (EF), a measure of the percent of the EDV that was ejected

$$EF = \frac{EDV - ESV}{EDV} = \frac{SV}{EDV}$$

The amount of blood pumped in one minute is called cardiac output (CO) and can be calculated as

$$CO = SV \cdot HR$$

where the heart rate HR is measured in beats per minute. Remembering that work can be calculated as the change in pressure multiplied by the change in volume, it follows that the

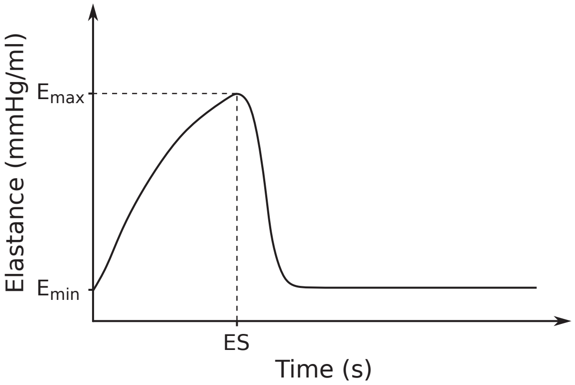

Figure 1.11: Illustration of the time-varying elastance curve shape. ES, end systole; E_{max}, maximum elastance; E_{min}, minimum elastance.

amount of energy consumed to eject blood, stroke work (SW), corresponds to the area within the PV loop

$$SW = \int P \cdot dV$$

The area bounded by the active and passive tension curves (ESPVR, EDPVR) and the leftmost side of the PV loop corresponds to the mechanical potential energy (PE) that the heart must overcome to eject blood [53]. Hence, the total pressure-volume area (PVA) corresponds to the ventricle's total energy consumption for one heartbeat

$$PVA = SW + PE$$

The PVA has been shown to be proportional to the total oxygen consumption of the ventricle [53].

1.1.5 Time-varying elastance

As the ventricle contracts and relaxes, the stiffness of the myocardium varies over time. In 1973, Suga et al introduced the concept of time-varying elastance $E(t)$ as a representation of this stiffness variation, defined as

$$E(t) = \frac{P(t)}{V(t) - V_0}$$

where $P(t)$ and $V(t)$ is the ventricular pressure and volume over time, respectively [54]. The parameter V_0 represents the ventricular volume at zero pressure, and can be interpreted as the minimum ventricular volume required for the ventricle to be able to generate pressure. Although V_0 fluctuates over the cardiac cycle [55], it can be approximated to a constant [55–57], making it possible to derive the time-varying elastance curve as the slope of the line connecting V_0 and the PV loop in each point of time.

The maximum elastance E_{max} occurs at end systole, meaning that the line connecting V_0 to end systole in the PV loop, the end-systolic pressure volume relation (ESPVR), is closely related to the active tension curve. Thus, E_{max} is interpreted as an index of ventricular contractility, which has been shown to be load-independent [54, 58]. The minimum elastance E_{min} occurs at end diastole, and the end-diastolic pressure volume relation (EDPVR) is therefore related to the passive tension curve and ventricular compliance. Myocardial compliance C can be calculated as the inverse of elastance

$$C(t) = \frac{1}{E} = \frac{V(t) - V_0}{P(t)}$$

Invasive recordings of ventricular pressure and volume has shown that the elastance curve has the same fundamental shape regardless of several healthy or pathological states, and in a variety of mammal species [54, 59, 60]. This consistency and the close association with the PV loop has motivated proposals of analytic equations mimicking the elastance curve shape [61, 62], which have been shown to be successful methods for coupling pressure and volume in mathematical models of the cardiovascular system [63–67]. Figure 1.11 illustrates the elastance curve shape.

1.1.6 Cardiovascular disease

Disturbances or defects in the cardiovascular system may result in pathophysiological processes, and lead to cardiovascular disease. In some cases, the disease may progress to a level where the heart is unable to supply the cardiac output demanded by metabolism, either acutely or chronically. In this case, the patient is diagnosed with heart failure, a serious clinical syndrome with a five-year mortality rate over 50% [68]. The overall mechanisms causing heart failure are often described as being due to as systolic or diastolic dysfunction, or a combination of both [69]. There are many underlying pathophysiologies that can lead to the development of heart failure, such as myocardial infarction and valvular dysfunction.

Systolic dysfunction

Systolic dysfunction is characterized by an impaired ventricular contraction, often caused by myocardial infarction. A decrease in contractility leads to an increase in ESV, followed by an increase in EDV, and a reduced SV, thus leading to a substantially reduced EF. This results in a narrower and shorter PV loop that is shifted to the right compared to a healthy PV loop (Figure 1.12). Systolic heart failure patients with a confirmed EF $< 40\%$ are diagnosed with heart failure with reduced ejection fraction (HFrEF) [69].

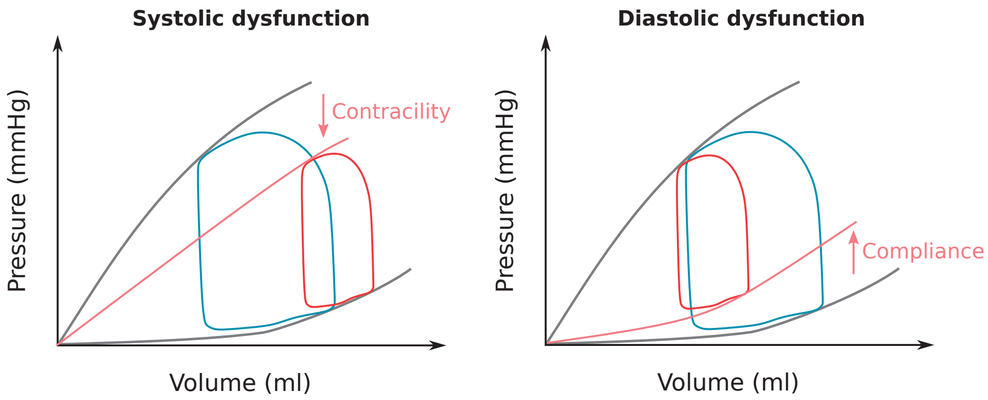

Figure 1.12: Illustration of a healthy pressure-volume loop (blue) in relation to pressure-volume loops in patients with systolic or diastolic dysfunction (red).

Diastolic dysfunction

Diastolic dysfunction is characterized by an impaired ability of ventricular relaxation and filling, often caused by hypertension, leading to decreased ventricular compliance affecting the preload [46]. An increased compliance results in an increase of end-diastolic pressure and a reduced EDV. Consequently, a reduction in ESV and SV follows, but with a maintained or slightly reduced ejection fraction. This results in a narrower and shorter PV loop that is shifted upwards and to the left compared to a healthy PV loop (Figure 1.12). Diastolic heart failure patients have an EF $> 40\%$ and are diagnosed with heart failure with preserved ejection fraction (HFpEF) [69]. Because they have an EF within the normal range, diagnosis of HFpEF cannot rely on measuring EF alone. Diagnosis of diastolic function is thus ideally evaluated by confirming an increased preload by cardiac catheterization. However, this is an invasive procedure and is therefore not routinely performed. Instead, the assessment is performed by studying a combination of ventricular inflow profiles, AV-plane velocity, and atrial volumes [70, 71].

Myocardial infarction

A common underlying cause of heart failure is myocardial infarction, which is the result of an occlusion in a coronary artery. This results in oxygen deprivation, or ischemia, of the part of the myocardium supplied with blood flow by the occluded artery, and may lead to structural damage or necrosis which affects the myocardial contractility [72].

Valvular dysfunction

Valvular dysfunction is also common in heart failure, both as the underlying cause or as a secondary consequence of another etiology. A cardiac valve is considered dysfunctional if it is insufficient or stenotic [73]. An insufficient valve allows transvalvular back-flow of blood, while a stenotic valve has a constricted opening that prevents normal blood flow. Transvalvular flow assessment is important in the treatment of these patients [73], but can be challenging due to the AV-plane displacement [74].

1.2 Magnetic resonance imaging

Magnetic resonance imaging (MRI) is a noninvasive technique free of ionizing radiation that was first implemented by Paul Lauterbur [75], followed by further developments on gradients by Peter Mansfield [76, 77]. Their discoveries were awarded the Nobel Prize in 2003.

1.2.1 Basic MR Physics

MRI can generate images in any cross-section of the body by utilizing the magnetic properties of hydrogen protons, which are mainly bounded to water and fat. The proton spins around its own axis, generating a magnetic moment with a positive and a negative pole. Thus, each hydrogen nucleus is a tiny magnet with a random spatial orientation. When subjected to a magnetic field $\overline{B_0}$, the proton spins will start precessing around the field direction. Due to the external magnetic field, the spins will tend to align with $\overline{B_0}$, thus creating a net magnetization vector $\overline{M}$. This magnetization $\overline{M}$ cannot be measured as it is, unless it is manipulated to deviate at an angle from the dominating $\overline{B_0}$ field.

This angulation of $\overline{M}$ is obtained by transmitting a radio frequency (RF) that resonates with the Larmor frequency of hydrogen protons, i.e. the angular frequency at which the spins precess, illustrated in Figure 1.13. The Larmor frequency f_0 depends on the gyromagnetic ratio γ, and the external field strength B_0, defined as

$$f_0 = \gamma \cdot B_0$$

with $\gamma = 42.6$ MHz/T for hydrogen protons. The transmitted RF pulse will induce a secondary magnetic field B_1 and reorient the net magnetization vector $\overline{M}$ to rotate around the B_0 field at a flip angle θ. Hence, $\overline{M}$ will go from having a single z-component to three components in the x, y and z direction (M_x, M_y, M_z). The flipped magnetization vector will with time return to its original position aligned with the B_0-field. This process is called relaxation and occurs independently in two planes; the longitudinal z-direction and in the transverse xy-plane. The regrowth of magnetization in the z-direction is exponential and can be described by the time constant T_1

$$M_z = M_z(0) \cdot e^{-t/T_1} + M_0 \left(1 - e^{-t/T_1}\right)$$

where $M_z(0)$ is the initial magnetization after excitation and M_0 is the magnitude of the equilibrium magnetization. Meanwhile, but independently from the T_1-relaxation, the

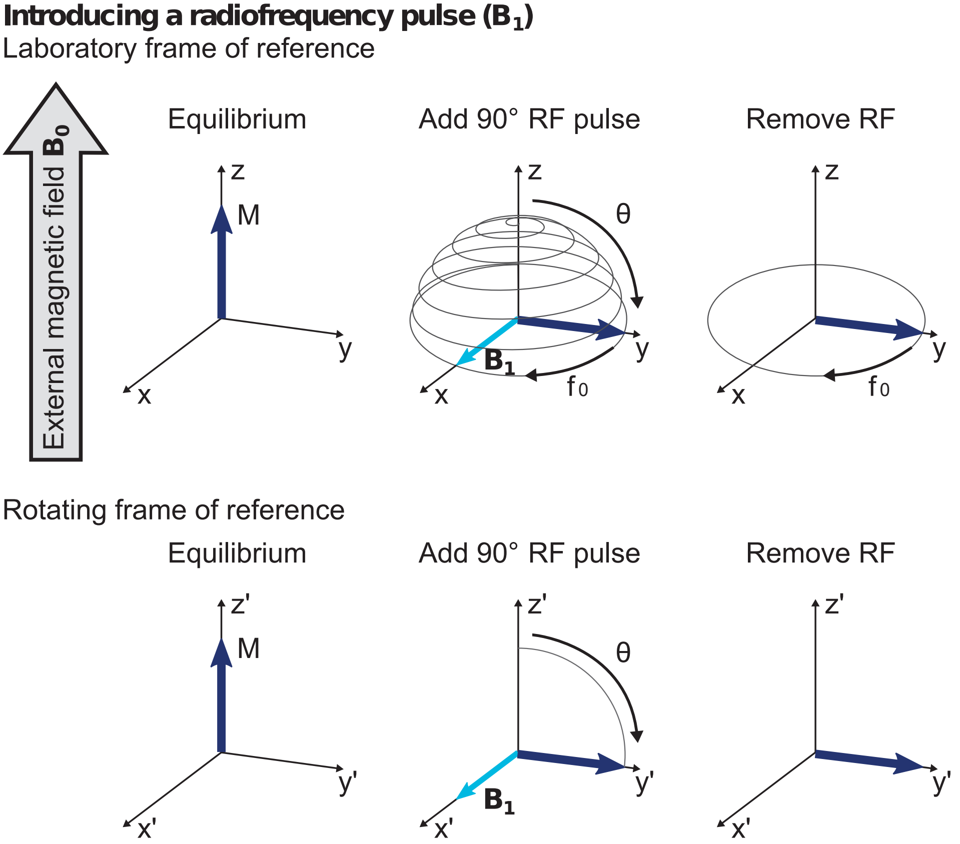
Introducing a radiofrequency pulse (B1)
Laboratory frame of reference
External magnetic field B0
Equilibrium
Add 90° RF pulse
Remove RF
z
M
y
x
θ
B1
f0
Rotating frame of reference
Equilibrium
Add 90° RF pulse
Remove RF
z'
M
y'
x'
θ
B1

Figure 1.13: Introduction of a 90° radio frequency (RF) pulse. At equilibrium the net magnetization vector $\overline{M}$ precesses with the frequency f_0 around the B_0-field in the z-direction. Application of an RF-pulse with angulation θ induces a secondary magnetic field B_1, resulting in a rotating descent of $\overline{M}$ to the transverse xy-plane. The flipped magnetization vector will return to precess around the B_0-field upon removal of the RF-pulse and thus the B_1 field. This process can either be studied in the laboratory frame of reference, or in a simplified rotating frame of reference without representation of the rotational component of the magnetization vector. *Adapted with permission from Per Arvidsson [43].*

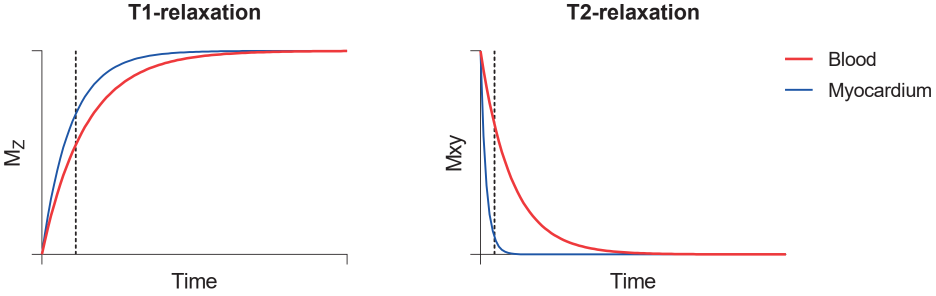

Figure 1.14: Example of T_1 and T_2 relaxation in myocardium (blue) and blood (red). The different T_1 and T_2 properties in the tissues will result in different relaxations of the magnetization in the z-direction and in the xy-plane. Thus, image acquisition at the time of the black dashed lines will yield contrast between the tissues. Note that the dashed lines are not represented at the same point of time in for the T_1 and T_2 relaxation, as these are two time independent processes.

dephasing of magnetization in the transversal xy-plane decay is exponentially described by the time constant T_2 as

$$M_{xy} = M_0 \cdot e^{-t/T_2}$$

The detailed behaviour of the net magnetization vector is described by the Bloch equations

$$\frac{d\overline{M}(t)}{dt} = \gamma \cdot \overline{M}(t) \times \overline{B}(t)$$

where $\overline{B}(t)$ is the magnetic field that the net magnetization $\overline{M}$ experiences [78].

As a flipped magnetization vector rotates in the xy-plane, electromagnetic radiation is emitted. This will induce an electric circuit in a receiver coil, allowing a voltage signal to be measured. Spatial information of this signal is obtained through frequency and phase encoding, by introducing a gradient in the magnetic field that slightly alters the frequency of the spins. Contrast is achieved since the molecular composition in different tissues have different T_1 and T_2 values, see Figure 1.14.

MR images are obtained by recording the generated frequency and phase signals and storing the information in a data matrix called k-space, and subsequently applying a Fourier transform. Depending on how the RF pulse, gradients and data sampling are performed, different static or dynamic images can be generated, containing information on for example anatomy, velocities, or tissue characteristics.

1.2.2 Cardiovascular magnetic resonance

When using MRI on the cardiovascular system, the method is called cardiovascular magnetic resonance (CMR). Typical field strengths in clinical CMR are 1.5T and 3T. In addition to the cardiac motion due to the pumping mechanism, the heart also moves inside the chest due to the respiration. Thus, to obtain high quality CMR images one must take into account the varying phases of the therefore monitored, or gated, simultaneously to imaging [79, 80].

The cardiac cycle is typically tracked by electrocardiogram (ECG) gating, which is used both as a triggering technique to determine when to start imaging and also to retrospectively organize the collected data according to the cardiac phase. For short imaging sequences up to about 15 s, respiratory motion is often suppressed by imaging at breath hold. Longer sequences are instead imaged at free breathing, typically employing respiratory gating, respiratory motion-compensation, or real-time imaging techniques [81–83].

CMR is considered the gold standard for assessing cardiac volumes, mass, and flow [2]. Images can be static or dynamic in time. Static CMR depicts a single image and is used to study anatomy or tissue characteristics. Dynamic CMR records a movie of the beating heart, called cine images, which are used to assess cardiac pumping. Furthermore, the depicted area may consist of single or multiple imaging planes. Commonly acquired sets of images to assess volume, mass, and function are long-axis cine images of the 2-chamber, 3-chamber, and 4-chamber views, and a multi-planar cine short-axis view covering the heart from base to apex, see Figure 1.15. Flow imaging is typically performed in a cross-sectional imaging plane perpendicular to the vessel of interest. Other examples of current capabilities of CMR imaging include measuring 4D flow, quantitative myocardial perfusion, fibrosis, edema, myocardial microstructure, and metabolism [16, 84–89].

1.2.3 Cine imaging and analysis

Length, area, and volume are measured in cine images acquired with a balanced steady-state-free-precession (bSSFP) sequence [90]. In short, by flipping the net magnetization vector back and forth around the z-direction, the transverse magnetization in the xy-plane is maintained at a steady-state over several heartbeats, allowing for a fast image acquisition with high contrast between blood and myocardium. Examples of long-axis and short-axis bSSFP images are shown in Figure 1.15.

Ventricular volumes are quantified by delineating the endocardial borders in a multi-planar short-axis stack, see Figure 1.15D. The delineated area in each slice is multiplied with the slice-thickness, yielding a volume. By summing the volumes of all delineated slices, the total volume of the ventricle in the depicted timeframe is calculated. This volumetric quantification method is called planimetry. The difference in volume between the end-diastolic and end-systolic timeframe yield the stroke volume. Multiplication of stroke volume and heart rate gives the cardiac output. Myocardial mass is measured by further delineating the epicardial borders.

1.2.4 Flow imaging and analysis

Flow is measured using phase contrast, a technique that encodes the relative tissue velocity in each pixel in either the through-plane or in-plane direction [74, 91, 92]. In short, a

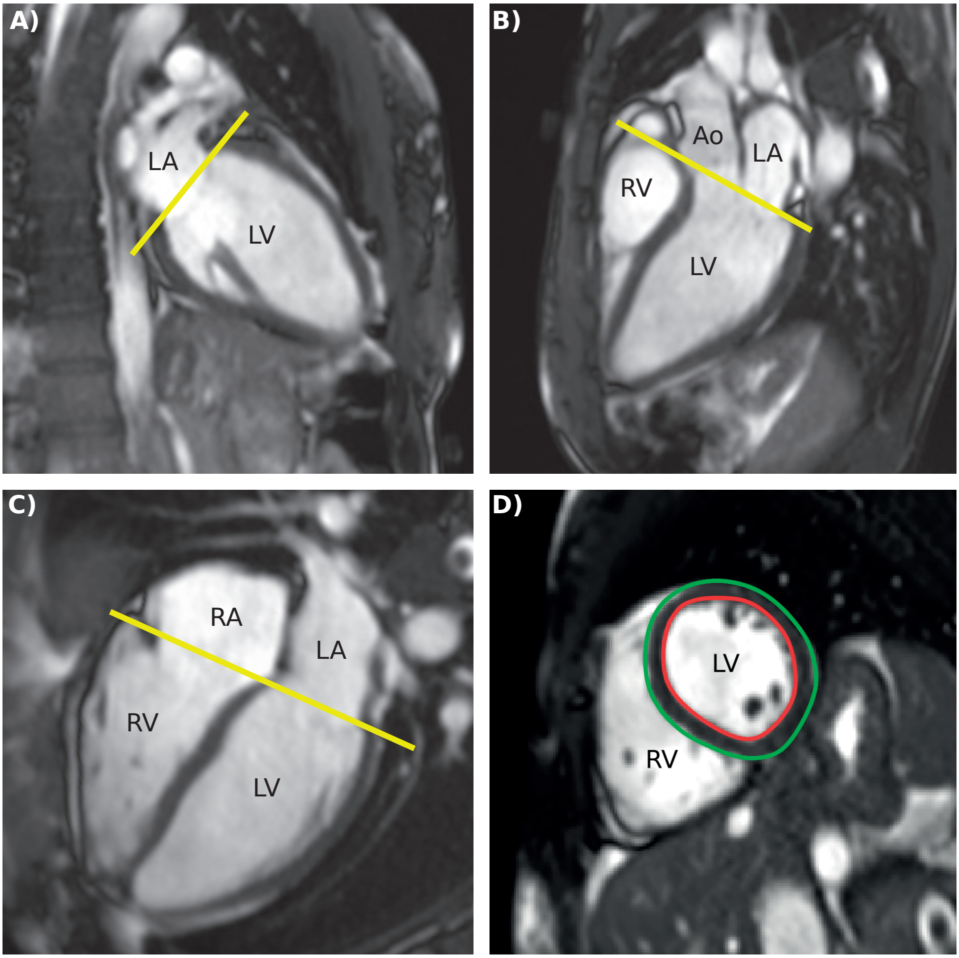

Figure 1.15: Example of long-axis and short-axis cine images at end diastole. **A)** Two chamber view showing the left atrium (LA) and left ventricle (LV). **B)** Three chamber view showing the LA, LV, right ventricle (RV), and the aorta (Ao). **C)** Four chamber view showing the LA, LV, RV, and right atrium (RA). **D)** Short-axis view showing the LV and RV. Yellow lines illustrates the AV-plane in each long-axis image. The outer green contour in the short-axis image marks the epicardial border, and the inner red contour the endocardial border.

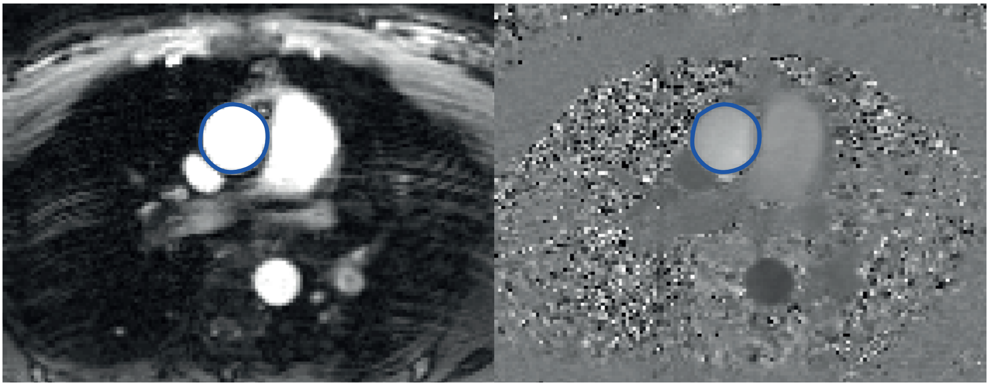

Figure 1.16: Example of a phase contrast image with through-plane flow encode direction above the aortic root (magnitude image to the left and phase image to the right). The blue delineation of the vessel is used to quantify aortic flow. The bright pixels in the phase image encode flow towards the head, and dark pixels denote flow in the opposite direction towards the feet.

bipolar pair of gradients is applied, resulting in an alteration in spin precession frequency and accumulation of phase. This accumulated phase shift will differ in static and moving tissue and is directly proportional to the tissue velocity [93]. The imaging technique generates two images, one anatomical magnitude image and one phase image from which the velocities are quantified, see Figure 1.16. Background phase offset error correction is performed to calibrate these velocities using either in static phantoms or by defining the velocity in static tissue to zero [94]. This calibration allows for both absolute velocity calculation in all pixels, and compensates for measurement errors due to gradient imperfections.

Flow is quantified from through-plane velocity encoded images as

$$Q = v \cdot A$$

where v is the mean velocity of the pixels within a delineated region of interest and A is the cross-sectional area of this delineation.

1.3 Cardiovascular pressure measurements

One of the main limitations of MRI is its inability to quantify absolute pressure. Relative pressure quantification and absolute quantification using CMR flow images and mathematical models have been proposed [66, 95–98], although the most established noninvasive pressure estimation is to calculate E/e' using echocardiogprahy [70, 71]. However, the accuracy of E/e' has been debated [99, 100], and invasive catheterizations remain the gold standard for measuring intracardiac pressure [101].

LV pressure catheterizations are typically performed by inserting a catheter into the carotid or femoral artery, which is then guided through the aorta into the LV using X-ray

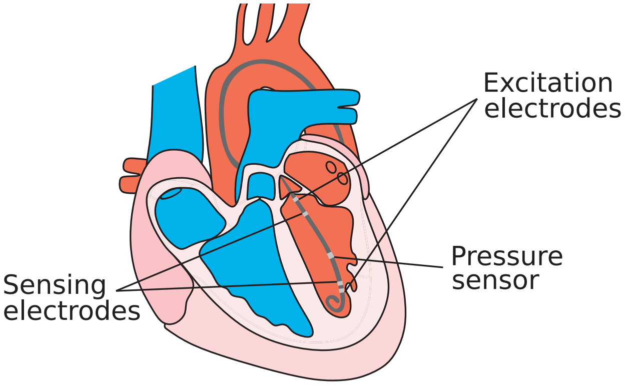

Figure 1.17: Illustration of a pressure-volume catheter inserted in a left ventricle via the aortic valve, with the tip of the catheter placed in the apex. *Image modified and used with permission from Servier Medical Art - Creative Commons Attribution 3.0 Unported Licence.*

angiography for visual guidance. The two main technologies for measuring intracardiac pressure are either solid-state pressure sensors or pressure transducers. Catheters combining simultaneous pressure and volume measurements, pressure-volume catheters, are also available. Noninvasive systolic and diastolic pressure in the systemic circulation are measured with sphygmomanometry as a clinical routine, and is performed by inflating a cuff around the upper arm [102].

1.3.1 Pressure-volume catheters

Pressure and volume can be measured simultaneously using a pressure-volume catheter, which consists of a pressure sensor and at least four volume electrodes, see Figure 1.17.

There are several different types of solid-state pressure sensors. A commonly used sensor for blood pressure measurements is the piezoelectric sensor consisting of a crystal and a diaphragm. When subjected to pressure, the diaphragm deforms, generating an electric voltage and a change in electrical potential. This electrical potential is measured and indicates the applied pressure on the sensor [103].

Volume is estimated by sending an alternating current between the excitation electrodes in the most apical and basal locations of the ventricle, creating an electrical field in the ventricle. The second most apical and basal electrodes are sensing electrodes that measure the change in voltage. Some catheters consist of more electrodes, allowing the user to activate the basal excitation and sensing electrodes that best correspond to the ventricular size. By utilizing Ohm's law, the conductance G (which is the inverse of resistance) is determined as

$$G = \frac{I}{U}$$

where U is voltage and I is current. As the electrical field passes through both blood and myocardium, the measured conductance G will contain information on the blood conductance G_b and the myocardial conductance G_m. By approximating the ventricular geometry to a cylinder, ventricular volume V can be estimated using Baan's equation

$$V = \frac{1}{\alpha}\rho L^2 \left(G - G_m\right)$$

where ρ is the blood resistivity, L is the distance between the sensing electrodes, and α is a constant correction factor [104, 105]. For accurate volumetric estimations, careful subject-specific calibration of α and G_m are important [106].

Another technology for volumetric catheter estimations is the admittance technique, which is an extension of the conductance catheter where the correction factor is not approximated to a constant. Admittance catheters measure both capacitance and resistivity, and estimate volume by separating myocardial conductance G_m and blood conductance G_b. This separation is performed utilizing the capacitive properties of myocardium which delays the measured voltage relative the input voltage. This allows for volumetric estimation by Wei's equation

$$V = \frac{1}{1 - \frac{G_b}{\gamma}} \cdot \rho L^2 G_b$$

where γ is a nonlinear dynamic field correction factor [107].

1.3.2 Pressure transducer catheters

Pressure transducer catheterizations are performed using a fluid filled tube connected to a transducer [108]. The ventricular pressure variation is transmitted through the fluid, which deforms an impermeable silicon diaphragm in the transducer. The transducer senses this deformation and converts it to an electrical signal that can be digitized. For accurate pressure quantification, it is important that the transducer is located and calibrated with atmospheric pressure at the same level as the heart. To avoid too much damping in the system, it is desirable to limit the length of the fluid-filled tube and make sure there are no air bubbles in the tube.

1.3.3 Cuff sphygmomanometry

Noninvasive brachial pressure is measured by inflating a cuff around the upper arm at the same height as the heart, see Figure 1.18. The pressure from the cuff will force the brachial artery to collapse, thus preventing blood flow. The cuff pressure is then slowly released, and a stethoscope is used to listen for the restoration of flow. The sound of the blood starting to flow again occurs when the cuff pressure is equal to the brachial systolic pressure. The diastolic brachial pressure is read when the sound of flow fades completely, as the cuff pressure is no longer impeding flow. Digital versions of the cuff sphygmomanometer employ automatic detection of systolic and diastolic pressure using oscillometric measurements.

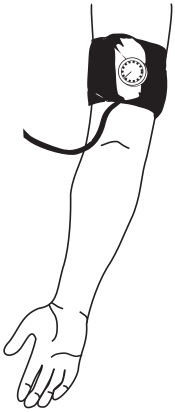

Figure 1.18: Illustration of a cuff for brachial pressure measurement.

1.4 Study motivations

CMR is a powerful imaging modality which is considered the gold standard for quantification of cardiac volumes and flow, and is also capable of characterizing tissue properties. While CMR is widely used clinically for subject-specific cardiovascular assessment, there are still physiologically important parameters with clinical value that are currently not accessible or readily available when using CMR. This motivates the work on expanding the current capabilities of CMR further, and thus getting closer to the reality of CMR as a one-stop-shop cardiovascular medical examination. In this thesis, work has been performed to engineer and validate reliable methods for quantification of physiology that remains inaccessible using CMR. The specific motivations for each study were:

Study I

A reduced AV-plane displacement is an independent predictor of major adverse cardiac events and mortality [30, 31]. AV-plane displacement is clinically measured in echocardiography, but not in CMR [109]. Manual measurements take 10-20 minutes to perform and are observer dependent. Algorithms for AV-plane tracking have been proposed [110–116]. There are however no validated and readily available tools for AV-plane displacement quantification that only require user input in a single timeframe, motivating the need for such algorithm.

Study II

Valvular imaging is challenging due to the AV-plane movement, as a short-axis slice will not depict the same tissue in all phases. Quantification of mitral regurgitation is however increasingly important [73, 117, 118], and is currently quantified by comparing measured stroke volume in short-axis and aortic flow images [109]. This procedure does not give any information about the flow profile through the valve. Slice-following methods for valvular imaging have been proposed [119–124], but there is currently no retrospectively gated phase contrast sequence available that adapts to the mitral valve movement already at the scanner. There is therefore a need for a sequence that can accurately measure transmitral flow over the entire cardiac cycle.

Study III

The PV loop has been shown to have clinical utility and critical clinical relevance in cardiovascular research [40, 41, 125, 126], and allows for quantification of hemodynamic parameters such as stroke work, total cardiac energy consumption, and contractility which are inaccessible with noninvasive techniques [26, 42]. Although volumes can be accurately measured with CMR, the generation of PV loops also require absolute pressure which is not quantifiable from CMR images. A noninvasive method to quantify PV loops is therefore motivated as is allows for a more comprehensive physiological assessment without subjecting patients to invasive catheterization procedures that carry risk.

Study IV

The contribution of longitudinal and radial pumping mechanics to stroke volume is $\sim$60% and $\sim$40% [10, 29]. Stroke volume does however not contain any information on the cardiac energy consumption, which is evaluated by calculating stroke work from the PV loop. Longitudinal and radial pumping is not reflected in the PV loop representation, leaving their contribution to stroke work unknown. The longitudinal and radial contributions to stroke work could potentially be determined from force-length relationships, but require a method for assessing global ventricular force-length loops describing longitudinal and radial pumping. Development of such a method could potentially expand our understanding of ventricular energy consumption, provide a deeper understanding of cardiac pumping mechanics, improve patient care, and lead the way forward for future cardiovascular treatments.

Chapter 2

Aims

The overall aim of this thesis was to expand the capabilities of CMR by proposing reliable methods and tools for quantification of the atrioventricular plane displacement, transmitral flow, pressure-volume loops, and ventricular force-length loops, hence allowing a more complete assessment of subject-specific cardiovascular physiology achievable in a single noninvasive examination. The specific aim of each individual study was:

Study I

To develop, validate, and provide a method that automatically tracks and quantifies the left and right ventricular atrioventricular plane displacement in CMR images.

Study II

To develop and validate a phase contrast CMR imaging sequence that employs feature-tracking in order to depict the mitral valve throughout the heartbeat, and to test the feasibility of measuring transmitral flow in these images.

Study III

To develop and experimentally validate a model-based framework for noninvasive pressure-volume loop estimation using CMR images and brachial blood pressure, and, as a proof-of-concept, to apply the model to healthy controls and patients with heart failure.

Study IV

To develop and experimentally validate a methodology to calculate ventricular force-length loops describing the longitudinal and radial pumping mechanics from CMR images, and to explore their contribution to stroke work in healthy controls and heart failure patients.

Chapter 3

Materials and methods

The most effective way to do it, is to do it.

Amelia Earhart

In order to expand the capabilities of CMR in quantifying cardiovascular physiology, new noninvasive tools for image acquisition and post-processing were developed and validated. The main features of each study is summarized in Table 3.1.

	Study I	**Study II**	**Study III**	**Study IV**
Physiology of interest	AV-plane displacement	Transmitral flow	PV loops	Ventricular force-length loops
Developed method	Image analysis algorithm	Pulse sequence	Image based model	Image based model
Validation method	Corresponding manual measurements	Phantom and corresponding SV measurements	Animal model	Animal model

Table 3.1: Overview of the included studies. AV, atrioventricular; PV, pressure-volume; SV, stroke volume.

3.1 Study population

A total of 220 subjects was included in this thesis, and consisted of 69 healthy controls, 32 elite endurance athletes, and 119 patients. Written informed consent was obtained from all study participants. Inclusions were performed at eleven different centers, and approved by the associated ethical review broad at each respective site.

Study I

Inclusions in Study I were retrospective, and comprised 81 patients with first time ST-elevation myocardial infarction from the multi-center clinical cardioprotection trial MITOCARE [127], previously published data from 40 healthy controls [128, 129], and 32 elite endurance athletes [128].

Study II

Inclusions in Study II were prospective, comprising of 10 patients with findings of mitral regurgitation and 16 healthy controls.

Study III

In Study III, previously published data from 13 healthy controls [130], and 28 patients with heart failure with reduced ejection fraction were included retrospectively [131]. The etiology of the heart failure was either ischemic heart disease (n = 14) or dilated cardiomyopathy (n = 14).

Study IV

Study IV included 12 healthy controls and 10 patients with dilated ischemic cardiomyopathy, and were a subset of the subjects in Study III.

3.2 Cardiovascular magnetic resonance

Cardiovascular magnetic resonance was performed on all subjects. Imaging was performed on either Siemens, Philips or GE systems at 1.5T or 3T with retrospective ECG-triggered gating.

For functional assessment, cine images in the long-axis and short-axis views were acquired using bSSFP at end-expiration. Typical imaging parameters were TR / TE / $\theta =$ 3.1 ms / 1.5 ms /60°, 890 Hz/pixel, matrix size 256x192, FOV 360 mm, voxel size 1.5x1.5x8 mm, no slice gap, 30 calculated phases.

Flow images were acquired using gradient echo 2D phase contrast with through-plane flow encoding. Typical aortic root imaging parameters were VENC = 180 cm/s, TR / TE / $\theta = 4.9$ ms / 2.7 ms / 20°, 3 bipolar pairs per segment, matrix size 208x168, FOV 330 mm, 1 average, voxel size 1.6x2.0x5 mm, 35 calculated phases, acquired at free breathing. Typical mitral valve imaging parameters were VENC = 150 cm/s, TR / TE / $\theta = 5.1$ ms / 4.0 ms / 15°, matrix size 224x208, FOV 350 mm, voxel size 1.5x1.5x8 mm, 3 bipolar pairs per phase, 22 calculated phases, acquired at end-expiration.

3.3 Animal model

A porcine model was used for optimization and validation purposes in Study III and IV. A total of 18 swine (7 males, weight 51 ± 11 kg) experiments were included. Five underwent invasive pressure-volume catheterization at baseline and 13 underwent both pressure catheterization and CMR. In the cohort that underwent CMR, 7 experiments were performed at baseline and 6 were performed at one week post-induction of myocardial infarction. Myocardial infarction was induced via a percutaneous insertion of a balloon in the left anterior descending artery followed by a 40 min occlusion and 1.5 h of reperfusion, as previously described [132]. The swine were not their own controls, meaning that the animals examined at baseline were not the same as those with induced myocardial infarction.

Invasive LV catheterization was performed using either a PV conductance catheter (Transonic, Ithaca, NY, USA) or a fluid-filled transducer catheter connected to a PowerLab transducer system (ADInstruments, Dunedin, New Zealand). Pressure calibration was performed prior to catheter insertion by defining a zero pressure reference environment at the same level as the heart. The PV catheter was calibrated by holding the pressure sensor just below the surface of a water filled container. Calibration of the transducer catheter was performed by exposing the transducer to atmospheric pressure.

Catheters were inserted into the LV through the aortic valve, accessed via the femoral or carotid artery. Simultaneously to LV pressure recordings, systolic and diastolic blood pressures were measured three times with noninvasive cuff sphygmomanometry in the tail. Typical time for pressure recording was five minutes. CMR was performed within three hours of the pressure recordings.

Anaesthesia was maintained on isoflurane gas throughout both pressure recordings and CMR, with care taken to not introduce significant hemodynamic alterations during the time of the measurements.

The experimental protocols were submitted and approved by the Swedish Agricultural Board.

3.4 Pressure data analysis

In order to enable analysis of the recorded LV pressures together with the data obtained from CMR, a reference pressure curve over one heartbeat was calculated. Customized software that automatically detected the beginning of each heartbeat in the recorded pressure data was developed for this purpose. The reference pressure curve was defined as the average of all detected heartbeats, and was synchronized so that the steepest negative slope occurred simultaneously with the end-systolic timeframe in the CMR data, see Figure 3.1. The peak systolic LV pressure, $LVP_{systole}$, was defined as the maximum value in the reference pressure curve, and the LV end-diastolic pressure, $LVP_{diastole}$, was defined as the last data point in the pressure curve. The mean of the three measured systolic and diastolic tail blood pressures were used as reference for noninvasive pressures, respectively.

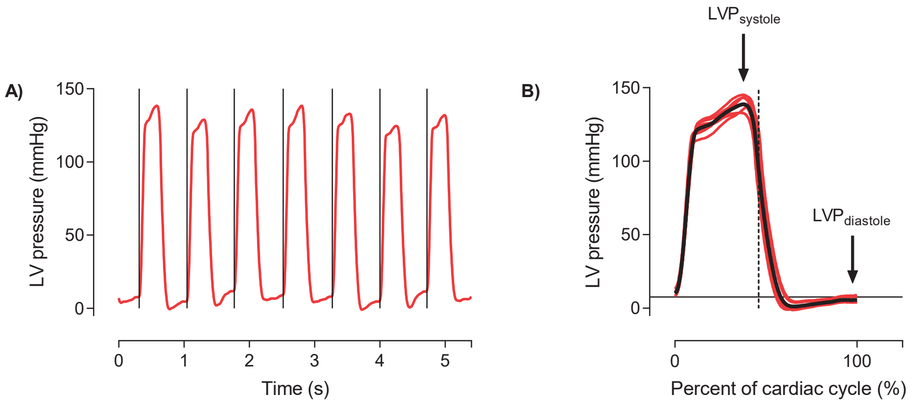

Figure 3.1: Reference pressure curve definition. **A**) Automatic detection of end diastole in a recorded signal of left ventricular (LV) pressure, shown as vertical black lines. **B**) Detected LV pressure of all heartbeats in red, and the mean LV pressure curve in black. The mean curve was used as reference pressure curve for validation purposes. The peak systolic pressure $LVP_{systole}$ was defined as the maximum pressure in the reference curve, and the end-diastolic pressure $LVP_{diastole}$ was defined as is the last data point in the reference curve (shown as a horizontal black line). The steepest negative slope is shown as a vertical dashed line, which was considered the end-systolic time.

3.5 Image analysis

CMR images were analyzed semi-automatically in the freely available software Segment (http://segment.heiberg.se) [133–135], with manual corrections performed as necessary.

LV volume and mass were measured in the short-axis cine images by contouring the LV endocardial and epicardial borders. Papillary muscles and LV outflow tract were included in the blood volume. Basal slices were included by cross-referencing from long-axis images and if 50% or more of the blood volume was surrounded by myocardium. Volume and mass were calculated by summation of the delineated slices in each respective timeframe. End diastole and end systole were defined as the timeframes with largest and smallest LV cavity volumes, respectively.

Longitudinal AV-plane displacement was measured in long-axis cine images of the 2-chamber, 3-chamber and 4-chamber views. The LV and RV AV-plane displacements were calculated as described by Carlsson et al [10, 29]. First, eight AV-plane insertion points were placed in all timeframes in the basal compact myocardium, see Figure 3.2A. The AV-plane was defined by the end-diastolic points in each long-axis view, and the perpendicular displacement of each point relative to this plane was computed. The LV AV-plane displacement was subsequently calculated as the average displacement in the six points pertaining to the LV myocardium. RV AV-plane displacement was defined as the average of the two septal points together with the two points pertaining to the RV myocardium. Radial displacement was calculated as the change in radius of the epicardial delineation over time in the short-axis slices, see Figure 3.2B.

Flow quantification was performed by drawing regions of interest along the borders of the aortic root and mitral valve, respectively. Phase offset background corrections were performed by indicating regions of static tissue.

3.6 Developed methods in this thesis

The overall features of the four proposed methods for quantification or cardiovascular physiology in this thesis are summarized in Table 3.1. The concepts and technical solutions employed for development and validation are briefly described below. The reader is kindly directed to each individual study for in-depth details on the respective technical implementations.

3.6.1 AV-plane displacement

In Study I, development and validation of a semi-automatic algorithm that performs time-resolved tracking of the AV-plane in CMR images was proposed. The algorithm requires manual definition of eight AV-plane input points at end diastole. A linear fit of these input points define the AV-plane in each long-axis view. Subsequently, each point is tracked individually using iterative feature-tracking by normalized cross-correlation [136].

First, an area of interest is extracted around the input point. A predefined area of search is then placed in the following timeframe. The position of this search area was established using a statistical model of the expected movement of each point, which was calculated from 40 subjects using principal component analysis. The best corresponding match of the input point within the area of search was determined using normalized cross-correlation. Iteratively, a new area of interest is extracted around this tracked point, whose best fit is sought in the area of search defined for the following timeframe. This procedure is illustrated in Figure 3.3, and is repeated by proceeding forward in time until reaching the last timeframe. To improve robustness, the entire tracking was performed a second time moving backwards in time. The resulting forward and backward tracked displacement curves were then merged as a weighted sum of the curves. The final displacement curves of the eight tracked points were used to calculate AV-plane displacement. AV-plane velocity at the peak emptying (s’) and peak filling (e’) was calculated as the slope of the approximated line over the AV-plane displacement in these timeframes, see Figure 3.4.

The size of the area of interest and area of search for each point were optimized in a training set of 40 subjects by optimizing correlation R, bias, and standard deviation (SD) between manual and algorithm AV-plane displacements. A exhaustive search over a range of possible combination of area sizes was performed with a 10-fold cross-validation.

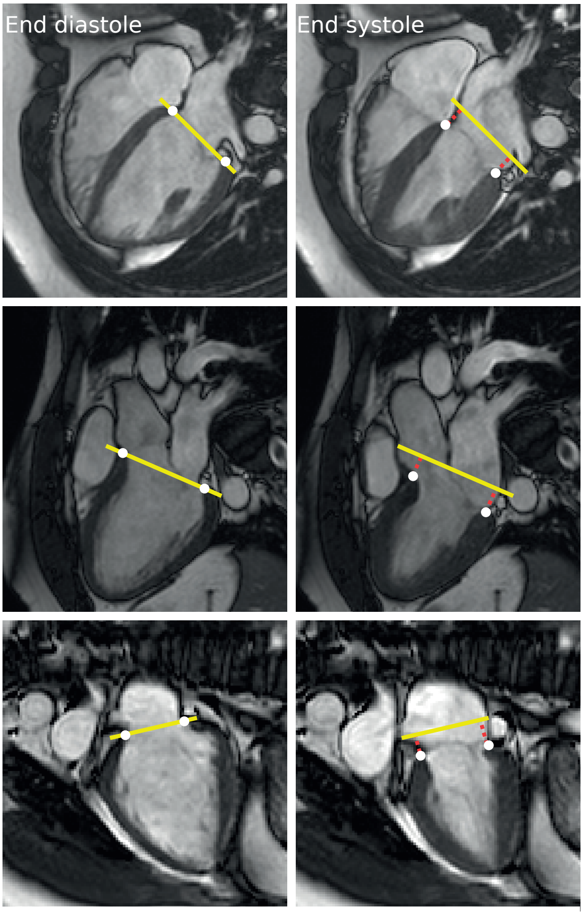

A) Longitudinal displacement

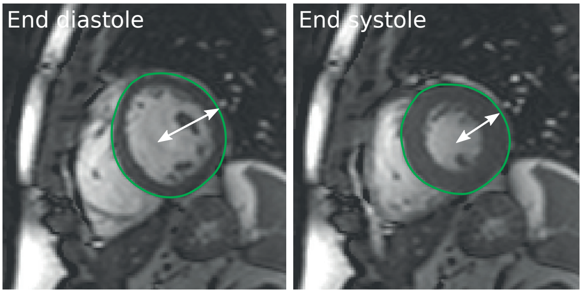

B) Radial displacement

Figure 3.2: Longitudinal and radial displacement calculations in the left ventricle. **A)** Longitudinal displacement was defined as the atrioventricular (AV) plane displacement. The basal LV myocardial insertion points (white circles) were indicated in all timeframes. The perpendicular distance (red dotted lines) from the end-diastolic AV-plane (yellow line) position to the points was calculated. The average displacement of the six points was considered the global longitudinal displacement. **B)** Radial displacement was calculated as the average change in radius (white double arrow) of the epicardial delineations (green) in each short-axis slice.

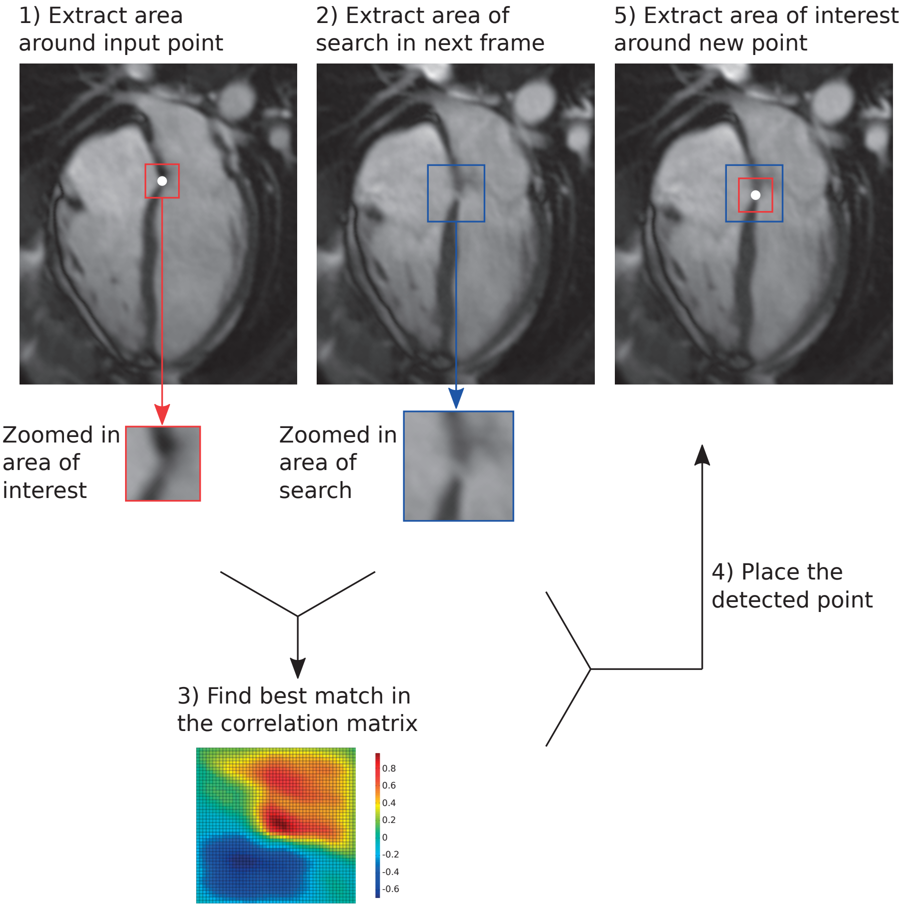
1) Extract area around input point
2) Extract area of search in next frame
5) Extract area of interest around new point
Zoomed in area of interest
Zoomed in area of search
4) Place the detected point
3) Find best match in the correlation matrix
0.8
0.6
0.4
0.2
0
-0.2
-0.4
-0.6

Figure 3.3: Illustration of the feature-tracking. 1) An area of interest is extracted around the input point. 2) A predefined area of search is then extracted in the following timeframe. 3) The normalized cross-correlation is taken between the two areas is performed. The best match of the area of interest within the area of search corresponds to the largest value in the correlation matrix. 4) Place a new point in the detected location. 5) Extract a new area of interest around the detected point. Repeat the procedure for all timeframes.

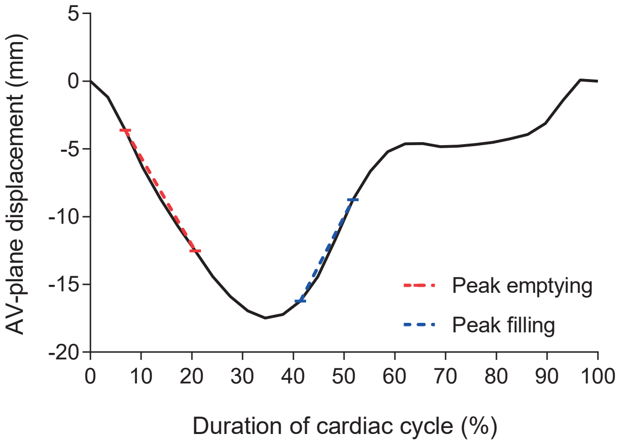

Figure 3.4: The atrioventricular (AV) plane velocities at peak emptying (s') and peak filling (e') were calculated as the slope of the approximated lines over these phases, respectively illustrated in red and blue.

Validation and observer variability

Validation of the algorithm was performed in a test set of 113 subjects by comparing the AV-plane displacement calculated by the algorithm with corresponding manual measurements. Inter-observer variability analysis of was performed in 20 patients.

3.6.2 Transmitral flow

In Study II, a mitral valve flow imaging sequence that prospectively updates the imaging slice location according to the valvular movement is proposed. The concept of slice-following was proposed by Kozerke et al, and was employed using spin labeling and ECG prospective gating in sequences which are no longer available for the CMR community [119, 120]. The proposed slice-following sequence is a modified retrospectively gated phase contrast gradient echo cine that is acquired over a single breath hold. The overall procedure on how to obtain slice-following is shown in Figure 3.5. The change in slice position was determined by performing offline AV-plane displacement analysis in a 4-chamber cine using the algorithm from Study I. The displacement was then saved to a file on the scanner, which is retrieved by the slice-following sequence, allowing for real-time updates of the imaging slice position based on the cardiac phase. For reference, a static phase contrast image planned at the end-systolic mitral valve location was acquired.

Mitral flow was quantified by delineating the mitral valvular borders in each timeframe. A portion of the LV filling, or mitral stroke volume (SV), originates from the movement of the mitral valve rather than pressure driven blood flow. This means that the mitral SV cannot be quantified directly by measuring the blood flow velocities reflected in the E and A waves. The passive transfer of blood volume from the LA to the LV due to the valvular

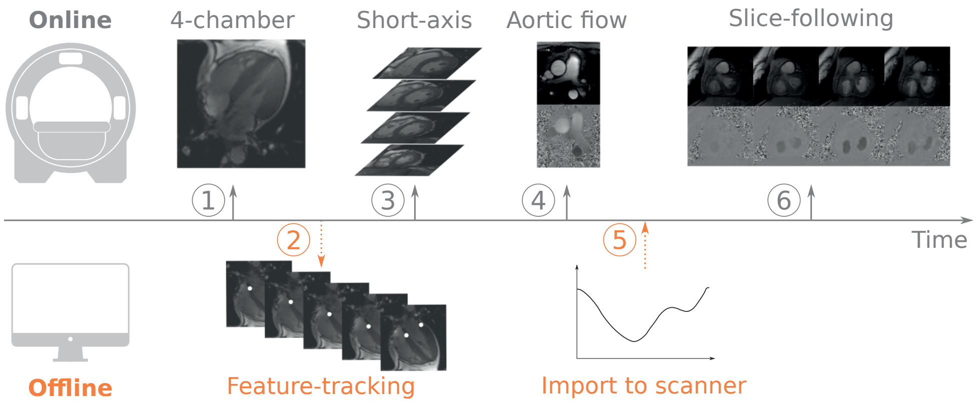

Figure 3.5: Workflow to obtain slice-following images. **1)** Acquire a 4-chamber cine image. **2)** Export the 4-chamber to offline and track the atrioventricular (AV) plane displacement using the algorithm in Study I. **3-4)** While AV-plane tracking is being performed, continue scanning the short-axis cine stack and aortic flow. **5)** Import the tracked displacements into the phase contrast slice-following sequence. **6)** Run the slice-following sequence. The time between the acquisition of the 4-chamber cine and the slice-following sequence was 5-10 minutes during which other sequences can be acquired.

through-plane motion must be taken into account, so that the phase images reflect both pressure driven and passively transferred blood [119, 121, 137]. A through-plane motion correction was therefore performed by subtracting the AV-plane velocity $AVPV$ from the velocities v in the phase images in each timeframe, resulting in the calculation of flow Q through the delineated area A as

$$Q(t) = (v(t) - AVPV(t)) \cdot A(t)$$

Mitral SV was then calculated as the diastolic forward flow volume. Mitral regurgitant volume was calculated directly from the slice-following images as the systolic backward flow volume, see Figure 3.6, as well as indirectly by computing the difference in mitral and aortic SV.

Validation and observer variability

Validation of quantitative flow measurements was performed by comparing mitral SV with planimetric SV from short-axis images and aortic SV from aortic flow images. Mitral regurgitant volumes measured in patients were compared with the current recommended quantification method as the difference in planimetric and aortic SV [109]. Furthermore, the programmed slice positioning update functionality was validated in a 3D printed cone shaped phantom by measuring the depicted slice radius and comparing it to the known analytical expression of radius as a function of height at each imaged position, see Figure 3.7. Inter-observer and intra-observer variability analysis of mitral SV was performed in ten healthy controls.

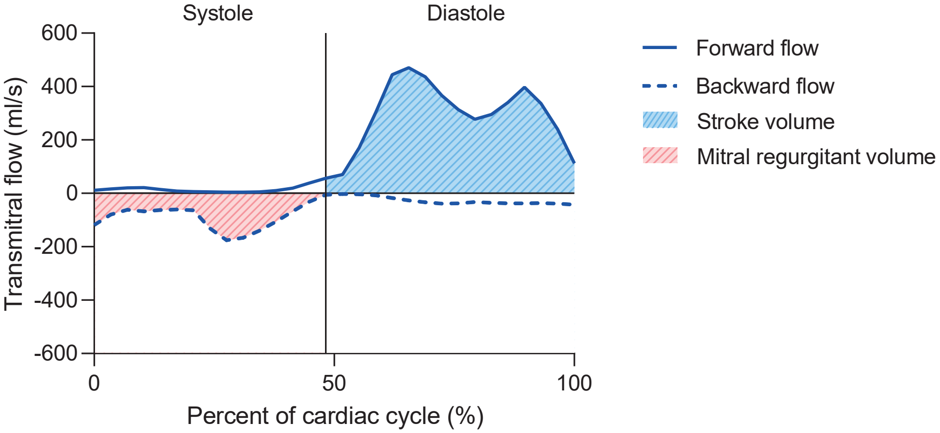

Figure 3.6: Illustration of stroke volume and mitral regurgitant volume quantification. Stroke volume was calculated as the amount of forward diastolic flow volume (blue area). Mitral regurgitant volume was calculated directly from the slice-following images as the backward systolic flow volume (pink area).

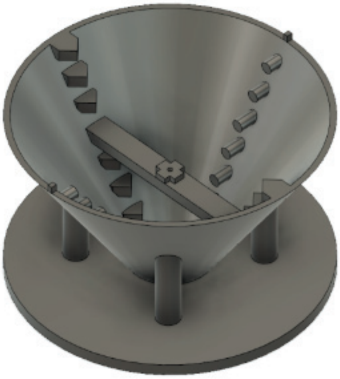

Figure 3.7: Three-dimensional rendering of the motionless phantom to confirm the programmed slice location. The 3D printed cone was 7 cm in height, with a 12 cm top diameter and 3 cm bottom diameter. A horizontal bar with 5 mm in thickness was located midway at the height 3.5cm, where the cone diameter was 7.5cm. The center of the cone in both height and width was marked with an elevated cross on top of the bar.

3.6.3 Noninvasive pressure-volume loops

In Study III, a noninvasive method for computation of pressure-volume loops was developed and validated. The method is based on the double-Hill equation, a mathematical model mimicking the intrinsic shape of the time-varying elastance as

$$E(t) = k \cdot \frac{g_1}{1+g_1} \cdot \frac{1}{1+g_2} + E_{min}$$

where

$$g_1 = \left(\frac{t}{\tau_1}\right)^{n_1}$$

$$g_2 = \left(\frac{t}{\tau_2}\right)^{n_2}$$

$$k = \frac{E_{max} - E_{min}}{max\left(\frac{g_1}{1+g_1} \cdot \frac{1}{1+g_2}\right)}$$

The model parameters n_1, n_2, τ_1, and τ_2 were experimentally optimized from a training set of 875 elastance curves derived as the fraction of pressure and volume measured invasively using a PV conductance catheter in five swine. Optimization was performed by minimizing the 1-norm between the double-Hill equation and the invasive elastance curve using the Nelder-Mead simplex method.

For each subject, the elastance curve was scaled in amplitude and time using LV volume curves measured from short-axis cine CMR images and the approximation of peak LV systolic pressure from noninvasive brachial systolic and diastolic blood pressure (SBP, DBP) proposed by Kelly et al [138] as

$$\frac{2}{3}SBP + \frac{1}{3}DBP$$

together with a user estimation of the LV end-diastolic pressure. The parameter V_0 was approximated to zero. Multiplication of elastance and volume yielded individualized pressure-volume loops, see Figure 3.8. Subsequently, six hemodynamic parameters were computed from the PV loop.

Stroke work SW was calculated as the area within the PV loop, and mechanical potential energy PE was defined as the area within the triangle bounded by the x-axis, a vertical line at the end-systolic volume, and the ESPVR-line which intercepts V_0 and the end-systolic LV pressure, see Figure 3.9. These parameters allow computation of the ventricular energy efficiency as

$$\eta = \frac{SW}{SW + PE} = \frac{SW}{PVA}$$

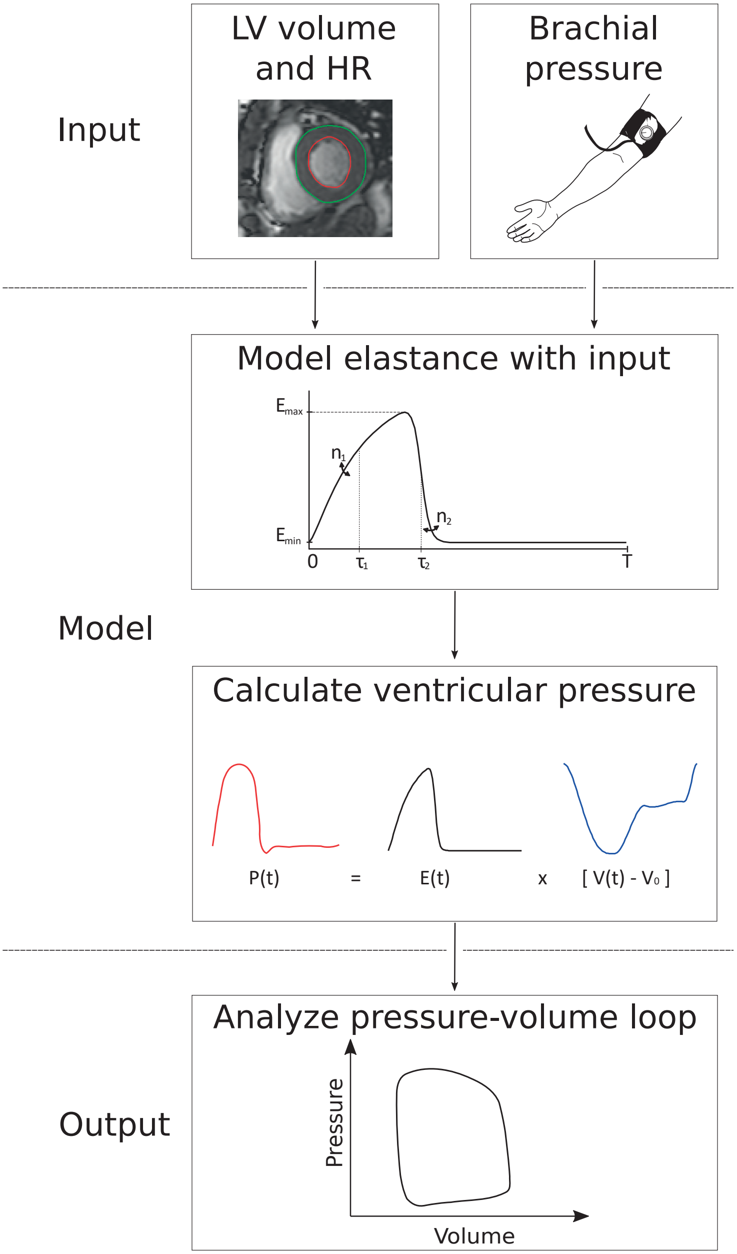
Input
LV volume and HR
Brachial pressure
Model elastance with input
E_max
n_1
n_2
E_min
0
τ_1
τ_2
T
Model
Calculate ventricular pressure
P(t)
=
E(t)
x
[V(t) - V₀]
Output
Analyze pressure-volume loop
Pressure
Volume

Figure 3.8: Pressure-volume (PV) loops were generated from measurements of left ventricular (LV) volume and heart rate (HR) obtained from cardiovascular magnetic resonance and noninvasive cuff brachial pressure. The elastance model was scaled in amplitude and time by this input. LV pressure $P(t)$ was subsequently calculated as the product of elastance $E(t)$ and volume $V(t)$, enabling the visualization of the pressure-volume loop.

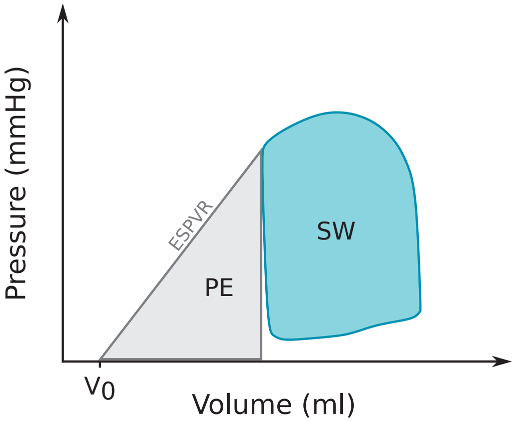

Figure 3.9: Illustration of the areas used for calculation of stroke work (SW) and potential energy (PE). Contractility was calculated as the slope of the approximated end-systolic pressure volume relation $(ESPVR)$.

and contractility as the slope of the ESPVR. Mean external power MEP delivered by the ventricle was calculated as

$$MEP = SW \cdot \frac{HR}{60}$$

where HR is the heart rate. Furthermore, the consumption of energy per ejected volume EEV was calculated as

$$EEV = \frac{PVA}{SV}$$

A sensitivity analysis on the impact of the quantified hemodynamic parameters depending on the LV end-diastolic and peak systolic pressures was performed.

Validation

The PV loop method was validated by studying the derived hemodynamic parameters. Experimental validation was performed in nine swine experiments using invasive pressure measurements and LV volume from CMR images (seven performed at baseline and two performed one week post induction of myocardial infarction). Moreover, a proof-of-concept was performed by applying the method to 13 human healthy controls and 28 heart failure patients, and studying the cohort differences in the derived hemodynamic parameters.

3.6.4 Ventricular force-length loops

In Study IV, a noninvasive method for computation of LV force-length loops describing global longitudinal and radial pumping mechanics is proposed, which can subsequently be used to quantify the longitudinal and radial contribution to stroke work. The contact force exerted by the blood pressure on the ventricular wall in the longitudinal and radial

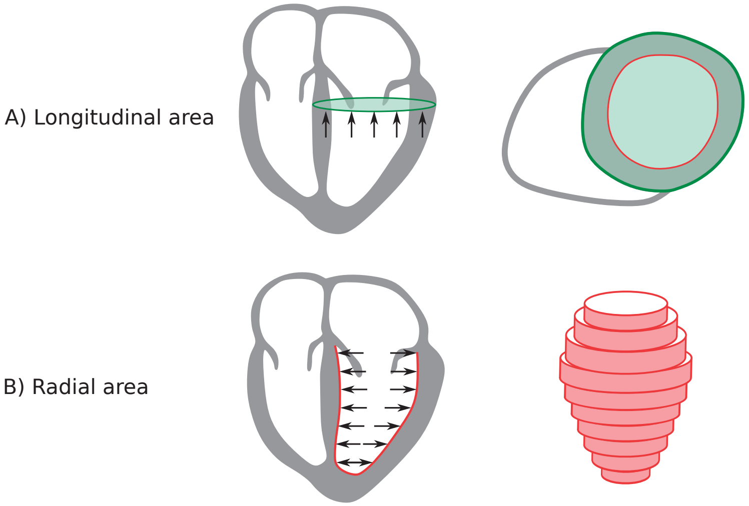

Figure 3.10: Schematic illustration of the areas on which the longitudinal and radial contact forces act. **A)** The longitudinal forces, illustrated by black arrows, act upon the largest cross-sectional epicardial area (green) at each point of time. **B)** The radial forces act upon the endocardial surface area (red) at each point of time, calculated in each short-axis slice as the circumference multiplied with the slice thickness.

directions were calculated using the fundamental physical relationship between force F, pressure P and area A

$$F = P \cdot A$$

which together with the length of the tissue displacement L allow for calculation of work W as the area within the respective force-length loops

$$W = \int F \cdot dL$$

LV pressure was invasively measured in swine, and noninvasively computed using the method in Study III in human healthy subjects and heart failure patients with ischemic dilated cardiomyopathy. Longitudinal force was defined as the LV pressure multiplied with the largest cross-sectional LV epicardial short-axis area in each timeframe, see Figure 3.10A. Radial force was calculated as LV pressure multiplied with the surface area of the endocardial delineations in short-axis cine images, calculated in each slice as the circumference multiplied with the slice thickness, see Figure 3.10B. The rationale behind these contact areas are illustrated and discussed in Figure 3.11.

AV-plane displacement was considered the longitudinal length, while the epicardial displacement in the radial direction was considered radial length. Longitudinal and radial stroke work was calculated as the area within each respective force-length loop.

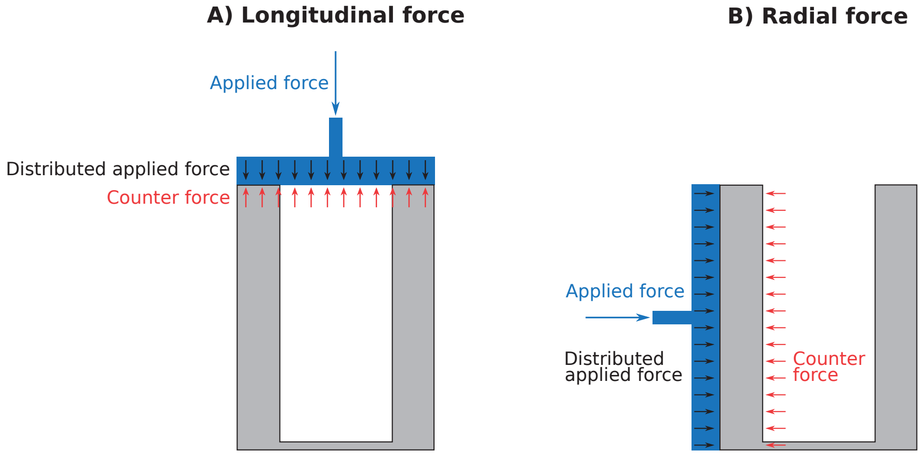

Figure 3.11: Schematic illustration of the areas upon which the longitudinal and radial forces act in a simplified ventricular model as a cylinder. The myocardial wall is highlighted in gray, and an imaginary piston applying an external force on the myocardium is shown in blue. An external applied force (blue arrow) will be distributed over the piston area (black arrows), generating a pressure inside the ventricle. The piston experiences counter forces (red arrows) along the contact area of the piston according to Newton's third law. **A)** Illustration of an isolated longitudinal contraction. As both the myocardium and the blood pool experience shortening in this direction, it follows that the piston pushes over the entire epicardial cross-sectional area. If the piston would only slide along the endocardial border, the longitudinal area upon which the counter forces act would be smaller and correspond to the largest endocardial cross-sectional area. The myocardium would in this case however remain in the exact same shape and position over the cardiac cycle. Since this is not how the left ventricle behaves, it is the epicardial cross-sectional area must be taken into account when calculating the longitudinal force. **B)** Illustration of an isolated radial contraction. The imagined radial piston pushes along the epicardial border of the ventricle, yielding an epicardial displacement, thickening and inward motion of the endocardial border, and a decrease in blood lumen. The generated blood pressure will then exert counter forces on the endocardial surface area. The thickness and movement of the apical myocardium was considered negligible in this study.

Furthermore, the longitudinal contribution to stroke volume was calculated as the end-systolic AV-plane displacement multiplied with the mean of the two largest basal cross-sectional epicardial short-axis areas at end diastole, as previously proposed by Carlsson et al [10]. The remaining amount of stroke volume was considered the radial contribution to stroke volume. This allows calculation of the amount of work per ejected volume WEV corresponding to the two different pumping mechanics as

$$WEV_{long} = \frac{SW_{long}}{SV_{long}}$$

and

$$WEV_{rad} = \frac{SW_{rad}}{SV_{rad}}$$

where SW is stroke work and SV is stroke volume.

Validation

The force-length loop model was validated by comparing the sum of longitudinal and radial SW to the conventionally quantification of SW as the area within the PV loop. Experimental validation was performed in 13 swine (seven performed at baseline and six performed one week post induction of myocardial infarction). Validation was also performed on human subjects (twelve healthy controls and ten heart failure patients) using noninvasive PV loops.

3.7 Statistical analysis

Statistical analysis was performed in the software GraphPad Prism (GraphPad Software Inc, La Jolla, CA, USA). The relationship between the quantified parameters was assessed by linear regression, Pearson R or Spearman ρ were reported. Agreement between methods was described by Bland-Altman analysis and intraclass correlation coefficient (ICC) [139, 140]. Agreement was considered poor for ICC = 0.0-0.3, weak for ICC = 0.31-0.50, moderate for ICC = 0.51-0.70, strong for ICC = 0.71-0.90, and excellent for ICC = 0.91-1.00 [140]. Differences between cohorts were tested with a parametric paired t-test or a Mann-Whitney test. The threshold for statistical significance was set at $p < 0.05$.

Chapter 4

Results and comments

> *All sorts of things can happen when you're open*
> *to new ideas and playing around with things.*
>
> Stephanie Kwolek

4.1 Study I: AV-plane displacement

The proposed algorithm was implemented as a freely available module in Segment (http://segment.heiberg.se) and was applicable in multi-center and multi-vendor data. The average time for tracking and was 0.6 s per subject. An example of a time-resolved LV AV-plane displacement obtained by the tracking algorithm and manual measurements is shown in Figure 4.1, revealing similar curves.

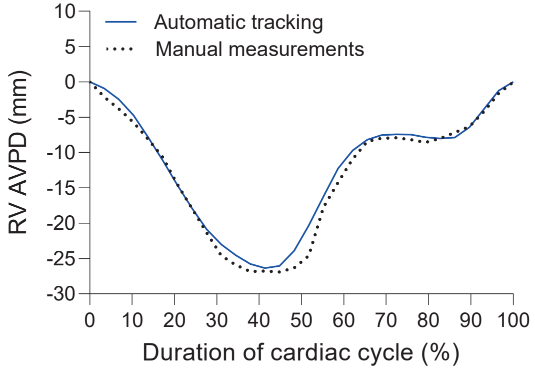

Figure 4.1: Example of a right ventricular (RV) atrioventricular plane displacement (AVPD) in a healthy control obtained with the proposed algorithm (blue line) and from manual measurements (black dotted line).

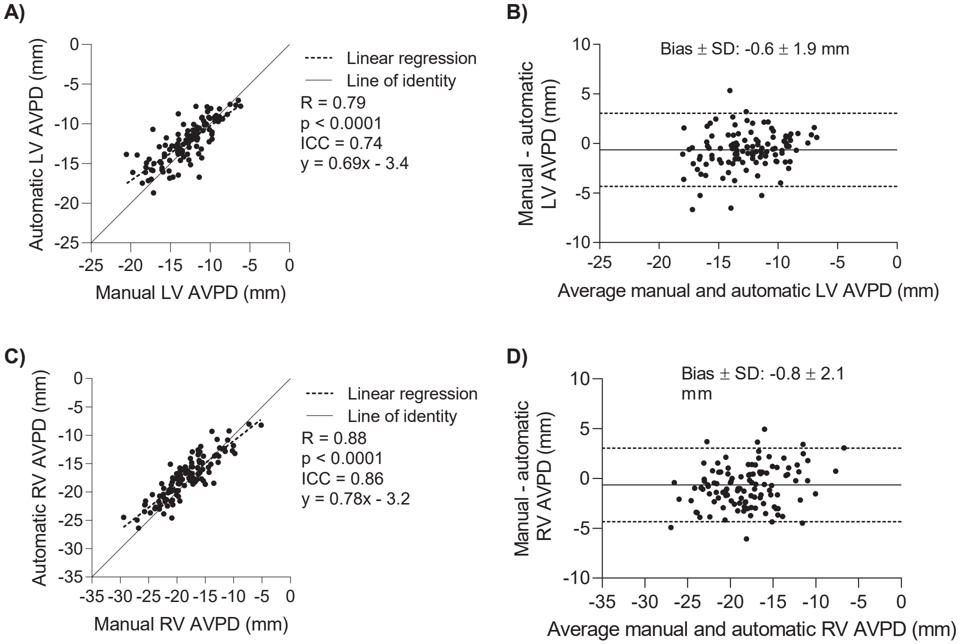

Figure 4.2: Comparison of manual and automatic end-systolic atrioventricular plane displacement (AVPD). **A**) Scatter plot of the left ventricular (LV) AVPD. **B**) Bland-Altman plot of the LV AVPD. Bias and limits of agreement are represented as solid and dashed lines, respectively. **C**) Scatter plot of the right ventricular (RV) AVPD. **D**) Bland-Altman plot of the RV AVPD. ICC: intraclass correlation coefficient; SD: standard deviation.

Displacement

Comparison of the tracked displacement to manual measurements in 113 subjects revealed a strong agreement with a bias below pixel resolution for both LV and RV AV-plane displacements, as shown in Figure 4.2. The results were consistent with the inter-observer variability of manual AV-plane displacement measurements at end systole in the LV and RV, see Table 4.1.

The sensitivity of the algorithm performance with regard to the input points was investigated by performing the tracking using input points provided by two different users. The difference in the resulting end-systolic AV-plane displacement, i.e. the inter-observer variability of the algorithm, was low for both the LV and the RV, see Table 4.1. This suggests that there was little sensitivity to input point positioning within the algorithm.

The iterative point tracking determines the point position in the current timeframe by finding the best possible match of the structure surrounding the tracked point in the previous timeframe. A failed tracking in one timeframe will therefore result in the search for another structure than the initially indicated by the input point, resulting in error propaga-

	Pearson R	Bias ± SD (mm)
LV manual inter-observer	0.95	-0.6 ± 0.7
RV manual inter-observer	0.95	-0.5 ± 1.4
LV algorithm inter-observer	0.91	0.1 ± 0.6
RV algorithm inter-observer	0.98	0.0 ± 0.7

Table 4.1: Manual and algorithm inter-observer variability analysis for end-systolic atrioventricular plane displacement. LV, left ventricle; RV, right ventricle; SD, standard deviation.

tion. A failure might occur at any time if the target structure is hard to identify in the following timeframe. Previously proposed algorithms for AV-plane tracking have approached this problem by placing input points in several timeframes [110, 112], interactive corrections with repeated tracking procedures [115]. In this study, principal component analysis and the merging of forward and backward tracking was used to minimize the potential error propagation, reducing the required input points to the end-diastolic timeframe only. However, as in any automatic image analysis tool, errors do occur from time to time, which is why monitoring and manual corrections remain important for research and clinical use.

Velocity

The peak AV-plane velocities during systole (s') and early rapid filling (e') were calculated as an approximation of the slope of the AV-plane displacement at peak emptying and peak filling in 20 patients. Agreements between manual and automatic measurements were weak for the LV but strong for the RV, see Figure 4.3. A trend of underestimation of high velocities was present for s' and e' in both ventricles. Note that s' is reported as a negative value, since the AV-plane moves downwards in systole.

The reason for less accurate AV-plane velocities compared to displacements is that displacements can be measured directly from the tracked points. In contrast, velocity quantification relies on the derivative of the displacement curve which introduces noise. Furthermore, the depicted AV-plane is often somewhat blurred at the time of s' and e' where velocities are high, which may difficult tracking in these timeframes. The quantification of LV e' in the 4-chamber view has however been improved in a later study where spline smoothing and calculation of the entire velocity curve was performed [141].

Summary

In summary, the proposed algorithm in Study I tracks the AV-plane in long-axis cine images. The calculated displacements were consistent with manual inter-observer variability, but the peak AV-plane velocities were less accurately estimated by the algorithm. Overall, the implemented module enables an observer-independent and less time-consuming method of tracking the AV-plane in CMR images.

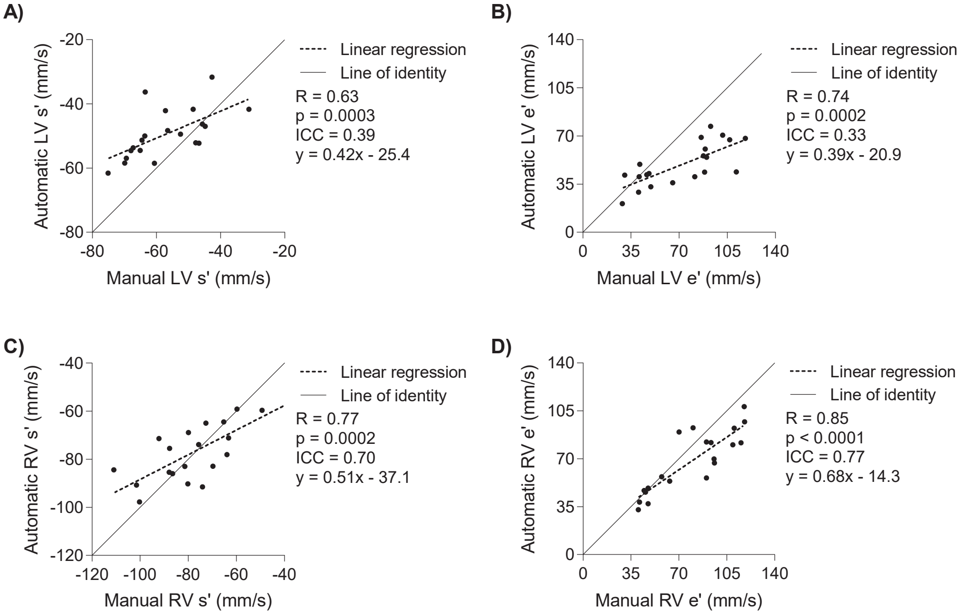

Figure 4.3: Scatter plots of manual and automatic peak atrioventricular plane velocities during systole (s') and the early rapid filling (e'). **A**) Left ventricular (LV) s'. **B**) Left ventricular e'. **C**) Right ventricular (RV) s'. **D**) Right ventricular e'. ICC: intraclass correlation coefficient.

4.2 Study II: Transmitral flow

Application of the slice-following phase contrast sequence was feasible in all subjects. Examples of mitral flow measured in a healthy subject and a patient with mitral regurgitation is shown in Figure 4.4.

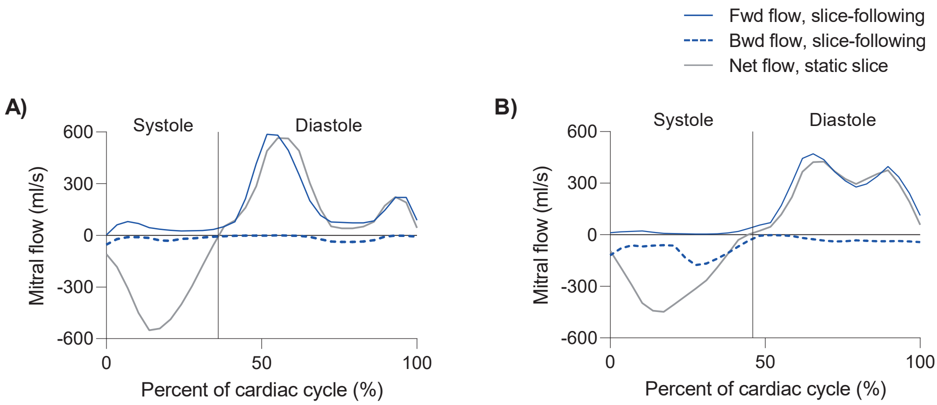

Figure 4.4: Example of mitral flow profiles in **A**) a healthy subject and **B**) a patient with mitral regurgitation. Forward (fwd) and backward (bwd) transmitral flow measured with slice-following phase contrast are shown as solid and dashed blue lines, respectively. The net flow measured with static phase contrast is shown as a solid grey line, and does not distinguish flow accelerated towards the left ventricular outflow tract from mitral regurgitation.

Mitral flow profiles detected by slice-following phase contrast were in line with what was physiologically expected. Diastolic flow had clear E and A waves and were similar in slice-following and static phase contrast images. However, significant differences in systolic flow were detected between the two methods ($p = 0.003$). In healthy controls, systolic blood flow in the LV proceeds superiorly towards the LV outflow tract. Regurgitant flow across the mitral valve proceeds in the same direction. Slice-following phase contrast was able to distinguish physiologically healthy LV outflow tract flow from regurgitant flow across the mitral valve. This represents an important advancement, enabling a quicker detection of mitral regurgitation.

Mitral stroke volume

Figure 4.5 shows comparisons of mitral SV quantified with and without slice-following against aortic and planimetric SV in healthy subjects. Since only trace amounts of mitral regurgitation is expected in healthy subjects, it is implied that mitral, aortic, and planimetric SV should be approximately equal. Mitral SV was quantified as the forward diastolic flow volume, as diastolic backward flow was not assumed to regurgitate back to the LA, but was rather assumed to reflect the rotating vortex ring formation at the LV inflow tract [131].

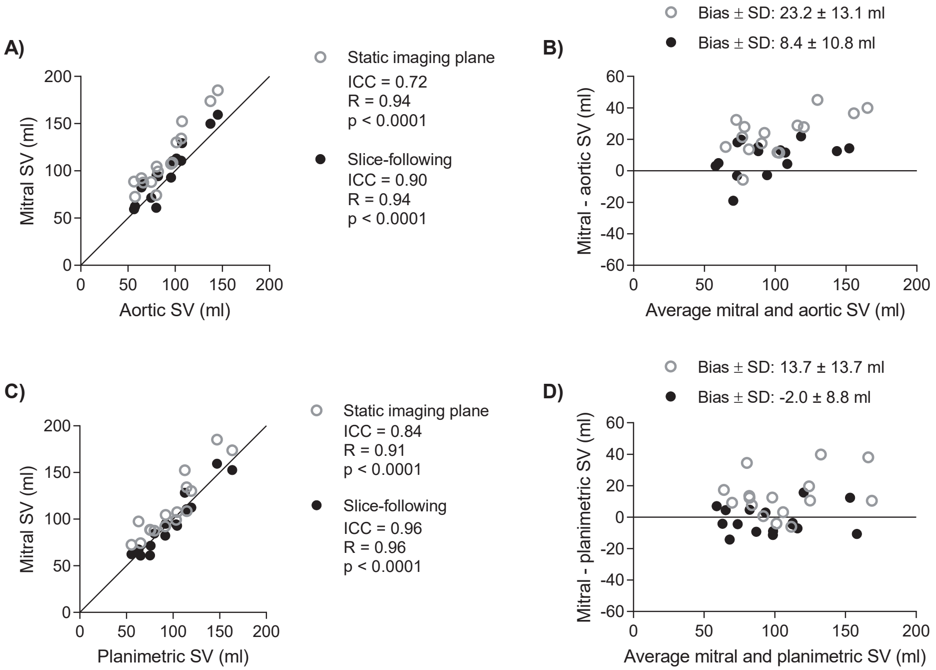

Figure 4.5: Mitral stroke volume (SV) measured with slice-following phase contrast (black dots) and static (gray circles) imaging planes compared to aortic and planimetric SV in healthy subjects. **A**) Scatter plot of mitral and aortic SV. Black line represents the line of identity. **B**) Bland-Altman plot for mitral and aortic SV. **C**) Scatter plot of mitral and planimetric SV. **D**) Bland-Altman plot for mitral and planimetric SV.

There was strong agreement between mitral and aortic SV measurements using both slice-following and static phase contrast in the healthy subjects. The larger mitral SV compared to aortic SV is in part explained by the aortic flow slice imaging position above the branching of the coronary arteries, meaning coronary arterial flow ($\sim$4% of the SV) is not accounted for in aortic flow measurements. Mitral and planimetric SV revealed excellent agreement using slice-following and strong agreement using static slices in healthy subjects.

Because planimetric and mitral SV should be equal even in the presence of mitral regurgitation, quantification using slice-following phase contrast provides more accurate SV data than aortic flow. Planimetric and mitral SV were similar when studying all 26 subjects with slice-following ($p = 0.36$), but not for static phase contrast where the difference was significant ($p = 0.0003$), see Table 4.2.

Furthermore, Table 4.2 shows that planimetric SV did not differ from mitral SV quantified with through-plane motion corrected slice-following, but there was a discrepancy of approximately 14% using uncorrected slice-following. This shows that the passive transfer of blood due to the AV-plane displacement is a significant source of LV filling, confirming

	Stroke volume (ml)	p-value
Planimetry	99 ± 36	
Mitral, slice-following	101 ± 43	p = 0.36
Mitral, slice-following uncorrected	87 ± 38	p = 0.0001
Mitral, static	115 ± 48	p = 0.0003

Table 4.2: Quantified stroke volumes as mean ± standard deviation in all subjects. P-values indicates differences to planimetric stroke volume, calculated using paired parametric t-tests.

	ICC	Bias ± SD (ml)
Mitral SV, intra-observer	0.99	-0.9 ± 3.3
Mitral SV, inter-observer	0.98	3.9 ± 3.8

Table 4.3: Intra-observer and inter-observer variability analysis for mitral stroke volume (SV) quantification from slice-following phase contrast images. ICC, intraclass correlation coefficient; SD, standard deviation.

previous work by Carlhäll et al [48]. This means that the amount of LV filling cannot be quantified directly by measuring the E and A waves since blood transferred passively due to AV-plane displacement must also be taken into account, which further emphasizes the previously reported importance of performing through-plane motion correction when quantifying valvular flow [119, 120, 137]. The overestimation in mitral SV using static imaging confirms previous work with retrospective valve tracking in 4D flow images [121, 123]. This is in part explained by larger areas being delineated in the more mid ventricular short-axis slices, in combination with the slice position being closer to the vena contracta of the mitral inflow. In short, the vena contracta is the point where the narrowest diameter and highest flow velocity occur in a jet, which is located downstream relative to the inflow orifice. Other potential explanations could be that the motion correction is performed on a valvular level rather than at the static image slice location, or that the static imaging slice is placed over the inflow vortex ring. Rotating blood in the vortex ring could potentially pass through the imaging plane more than once over the cardiac cycle, and would in this case be accounted for multiple times.

Observer variability of the delineated regions of interest used for mitral SV quantification revealed excellent agreement and low bias in both intra-observer and inter-observer variability analysis, see Table 4.3. This suggests that image processing for transmitral flow quantification with slice-following phase contrast is highly reproducible.

Mitral regurgitation

The conventional method for quantifying mitral regurgitant volumes using CMR is to calculate the difference in planimetric and aortic SV [109]. Slice-following could potentially be used to quantify mitral regurgitant volumes. Direct quantification as the systolic backward flow and indirect quantification as the difference in mitral and aortic SV revealed

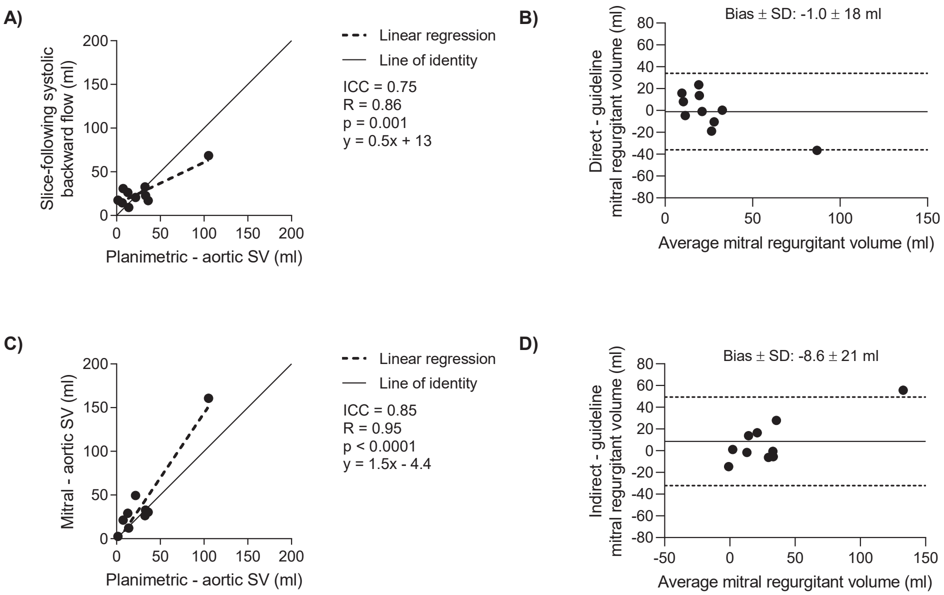

Figure 4.6: Mitral regurgitant volumes quantified in 10 patients. Direct and indirect measurements from slice-following phase contrast were compared with current guidelines as the difference in planimetric and aortic stroke volume (SV). **A**) Scatter plot for the direct method defining mitral regurgitant volume as the systolic backward flow. **B**) Bland-Altman plot for the direct method. Solid line represent the bias and dashed lined the limits of agreement. **C**) Scatter plot for the indirect method defining mitral regurgitant volume as the difference in mitral and aortic SV. **D**) Bland-Altman plot for the indirect method.

strong agreements with the conventional method, but the limits of agreement spanned over 60 ml, see Figure 4.6. An important source of error using the direct method is the through-plane flow encoding, meaning that it cannot accurately measure regurgitant jets if their angulation relative to the imaging plane is larger than ∼10% [142]. The indirect approach could be beneficial as both mitral and aortic SV are measured with phase contrast, reducing image processing time since SV quantification from flow images is less time consuming than planimetry. Additional studies on patients with varying degrees of mitral regurgitation are however warranted to establish the robustness of the sequence in measuring regurgitant volumes.

Implementation details

The programmed slice positioning functionality disclosed a bias of -0.01 ± 0.03 mm between the measured radii and analytically calculated cone radii at different programmed slice positions, see Figure 4.7. This suggests that the imaging slice moves according to the provided displacement input.

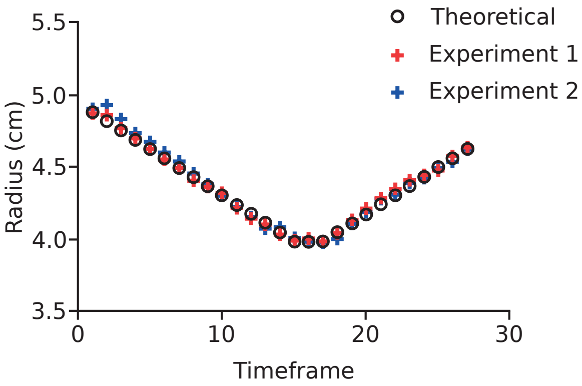

Figure 4.7: Cone radii measured in two phantom experiments in red and blue, demonstrating accurate slice-following compared to the theoretical radii at the programmed slice locations at both 1.5T and 3T.

The offline image analysis took 5-10 minutes, from the export of the 4-chamber to the import of the displacement cruve. This separation in time between the offline analysis and the slice-following imaging is a source of error since the AV-plane displacement may vary in this period of time, for example due to variation in breath-hold position or heart rate.

Summary

In summary, Study II presents a phase contrast CMR sequence with slice-following that is able to follow and depict the mitral valve in all phases. The sequence is feasible in healthy subjects and patients, providing flow patterns which are in line with what is physiologically expected. Mitral SV quantification was accurate when applying through-plane motion correction, revealing that the blood being passively transferred into the LV due to the AV-plane displacement correspond to ∼14%, and must be taken into account when measuring LV filling. The sequence is also able to detect mitral regurgitant flow provided that the backward systolic flow is not too angled relative to the mitral valve.

4.3 Study III: Noninvasive pressure-volume loops

The proposed PV loop model was implemented in Segment (http://segment.heiberg.se) and was applicable to both experimental and human subject data. Examples of generated PV loops are shown in Figure 4.8. The mean PV loops derived from the healthy controls and heart failure cohorts (Figure 4.8B) represented expected physiological differences, where the heart failure PV loop indicates a dilated LV with decreased SV that is pumping against a higher pressure compared to controls. Furthermore, a decreased contractility and increased total energy consumption can be derived from the heart failure PV loop. Note that both loops are represented at the same end-diastolic pressure, as the magnitude of this parameter was not estimated in this study.

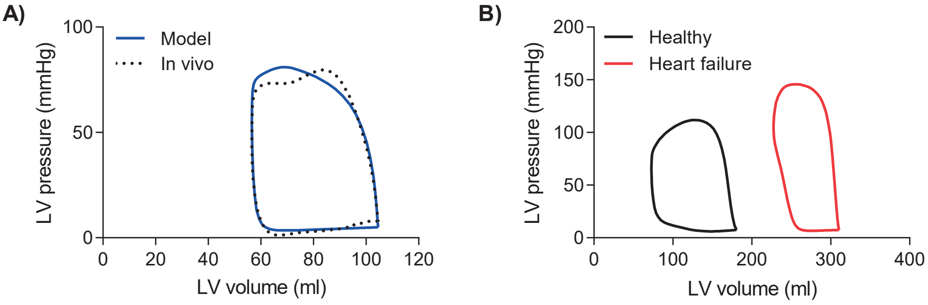

Figure 4.8: Example of left ventricular pressure-volume (PV) loops. **A)** Corresponding PV loops generated by the proposed model (blue line) and from experimental *in vivo* measurements (black dotted line). **B)** Mean model generated PV loops in the healthy controls (black) and heart failure patients (red). Both loops are represented at the same end-diastolic pressure to since this parameter was unknown in the studied cohorts. Heart failure patients are expected to have a higher end-diastolic pressure than healthy controls.

Elastance curve shape

An example of the proposed mathematical double-Hill representation of the time-varying elastance is shown together with its corresponding invasively measured elastance curve in Figure 4.9.

The foundation of the proposed model to derive subject-specific PV loops is the remarkable consistency of the the time-varying elastance curve shape regardless of loading conditions in several pathological states and in a variety of mammal species [54, 59, 60]. This normalized elastance curve shape was defined by the optimized double-Hill equation parameters n_1, n_2, τ_1, τ_2, as shown in Table 4.4. These experimentally optimized values were slightly different from those previously proposed by Mynard et al, who derived their parameter values using literature values [64]. Furthermore, this study optimized τ_2 as a function of the end-systolic time rather than the duration of the entire cardiac cycle. The reason to do so was that τ_2 describes the point in time where the elastance curve transi-

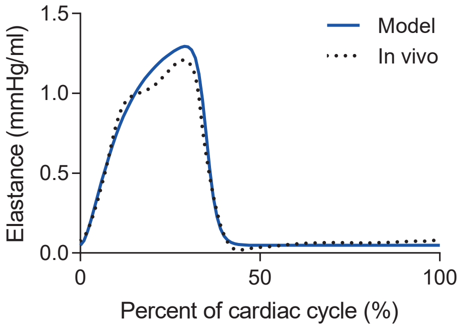

Figure 4.9: Example of left ventricular time-varying elastance represented as an optimized and subject-specifically scaled double-Hill equation (blue line) with a corresponding experimental *in vivo* measurement (black dotted line).

tions from being concave to convex. This time point occurs shortly after end systole, and was therefore considered a more robust temporal event as the diastolic duration varies with heart rate [51].

Parameter	Value
n_1	1.63
n_2	24.2
τ_1 (s)	$0.113 \cdot \mathrm{T}_{cycle}$
τ_2 (s)	$1.035 \cdot \mathrm{T}_{ES}$

Table 4.4: Optimized double-Hill equation parameters that were used in the time-varying elastance model. T_{cycle}: duration of the cardiac cycle, T_{ES}: end-systolic time.

A subject-specific elastance curve was obtained by scaling the optimized elastance shape in amplitude and time. Temporal events were extracted from the LV volume-time curve obtained from CMR images, while the amplitude scaling was defined by the end-diastolic and peak systolic LV pressures ($LVP_{diastole}$, $LVP_{systole}$). The values of these pressure parameters were based on a user assumption and an approximation from brachial pressure, respectively. A sensitivity analysis of the PV loop derived hemodynamic parameters was performed by varying the amplitude scaling. Manipulation of the parameter $LVP_{diastole}$ between 0-15 mmHg had a low impact on the PV loop derived hemodynamic parameters. This strengthens the robustness of the proposed model, as $LVP_{diastole}$ requires a user assumption that can be hard to estimate. Current echocardiography guidelines could potentially be used to perform this LV filling pressure estimation [71], although their accuracy has been debated [99, 100]. Manipulation of $LVP_{systole}$ as the invasively measured $LVP_{systole} \pm 10$ mmHg did also disclose a low error and variability. This suggests that the precision of the peak systolic approximation suffices for the proposed model, even if

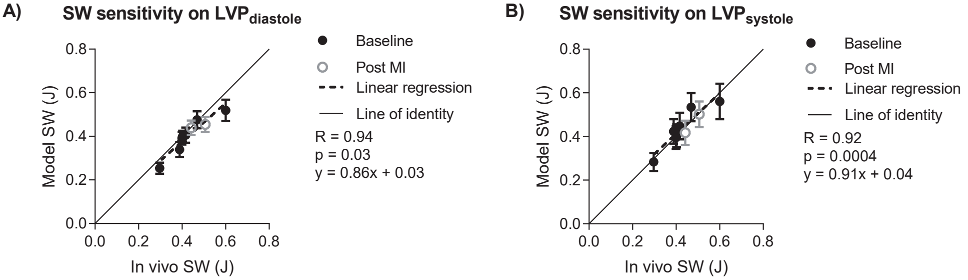

Figure 4.10: Sensitivity analysis of the model generated stroke work (SW) in the experimental cohort. **A)** Sensitivity in diastolic pressure ($LVP_{diastole}$) ranging 0-15 mmHg. **B)** Sensitivity in peak systolic pressure ($LVP_{systole}$) ranging as the invasively measured $LVP_{systole} \pm 10$ mmHg. Average SW is represented by dots, range as vertical bars. Black dots represent experiments performed at baseline, open grey circles represent experiments performed one week post induction of myocardial infarction (MI).

the brachial pressure was not measured simultaneously to the CMR image acquisition. Applanation tonometry could however potentially further improve this approximation [143]. Stroke work was most the sensitive parameter, and is shown in Figure 4.10.

Another parameter that is crucial in calculating the time-varying elastance curve but that is not present in the double-Hill equation is V_0. V_0 represents the ventricular volume at zero pressure, and is a theoretical parameter that cannot be measured directly. It is instead approximated as the point where the line connecting end systole in several consecutively measured PV loops, the ESPVR-line, intersects the volume axis. The ESPVR is however not perfectly linear and V_0 has also been shown to fluctuate over the cardiac cycle [144]. Hence, although a fixed V_0 is extensively used in cardiovascular modeling [55–57, 63–65, 145], it should not be forgotten that it is indeed a model approximation that could potentially be further improved.

PV loop derived hemodynamic parameters

The experimental validation of the model is shown in Figure 4.11. The agreement between model derived and *in vivo* measurements was moderate for potential energy, strong for stroke work, and excellent for ventricular efficiency. This suggests that the model generated PV loops correspond well with *in vivo* measured PV loops, even though the *in vivo* measured pressures were not recorded simultaneously to the CMR examination. The reason for this was that the required equipment for pressure catheterization lacked MR compliance. Care was however taken to maintain the animals at a similar physiological state during and between the two examinations.

The hemodynamic parameters derived from model generated PV loops demonstrated differences between the healthy control and heart failure cohorts which were in line with previous findings [146, 147], see Figure 4.12. Patients had a decreased ventricular effi-

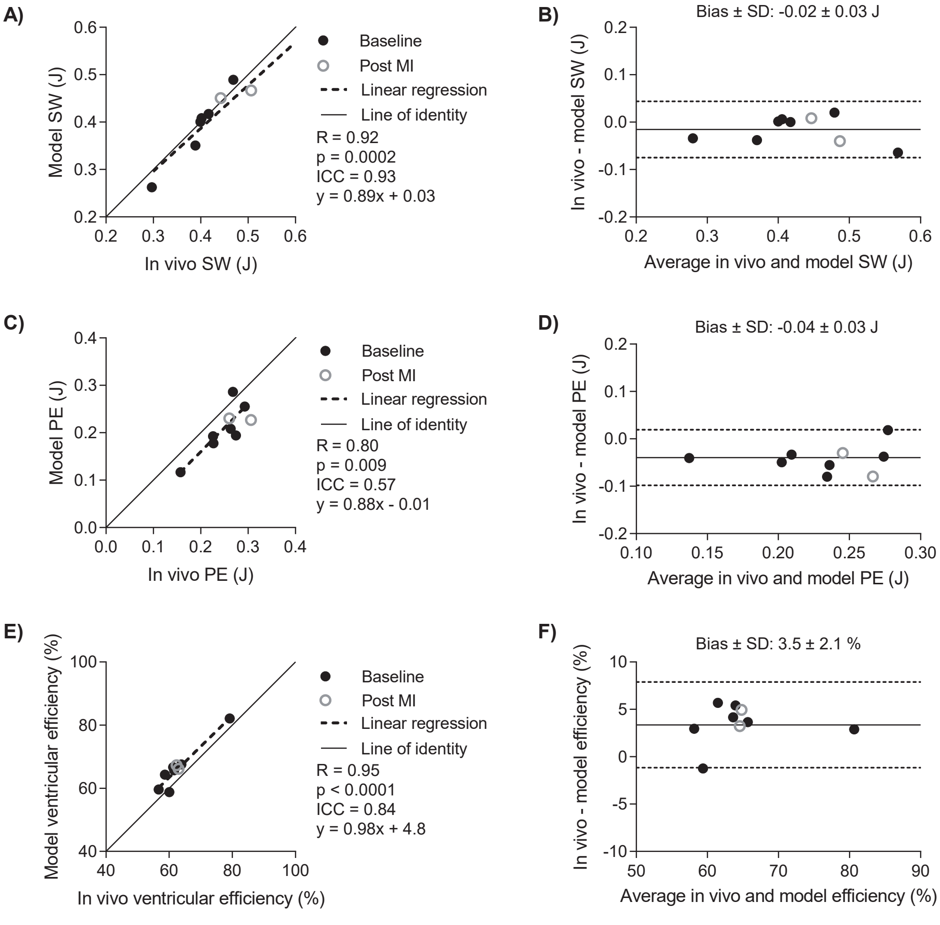

Figure 4.11: Comparison between model derived and *in vivo* measured hemodynamic parameters. Black dots represent experiments performed at baseline, open grey circles represent experiments performed one week post induction of myocardial infarction (MI). **A**) Scatter plot for stroke work ((SW)). **B**) Bland-Altman plot for SW. Solid line represent the bias and dashed lined the limits of agreement. **C**) Scatter plot for potential energy ((PE)). **D**) Bland-Altman plot for PE. **E**) Scatter plot for ventricular efficiency. **F**) Bland-Altman plot for ventricular efficiency.

ciency and contractility, increased potential energy and energy per ejected volume, while no differences were observed in stroke work and mean external power. Although PV loop analysis has been pointed out of having relevance and utility in cardiovascular research [40, 41, 125], it remains to be investigated if there is an added clinical and prognostic value of this noninvasive PV loop assessment. The added value of evaluating ventricular efficiency instead of ejection fraction is however uncertain, as these parameters correlated strongly in the studied cohorts ($\rho = 0.99$).

Ejection fraction is however not decreased in all cardiac disease, where for example about half of the heart failure patients present with a preserved ejection fraction [69]. This justifies the search for additional hemodynamic parameters which could characterize and aid the diagnosis of these patients. Noninvasive PV loops and parameters such as potential energy, contractility, and energy per ejected volume may therefore allow for a low risk and cost-effective way of deriving a more comprehensive physiological analysis from standard CMR examinations.

Summary

In summary, Study III presents a validated method to obtain subject-specific PV loops noninvasively. The method is based on a mathematical representation of the time-varying elastance and generates accurate representations of PV loops and its associated hemodynamic parameters, which might enable the ability to expand the current capabilities in noninvasive physiological assessment of patients.

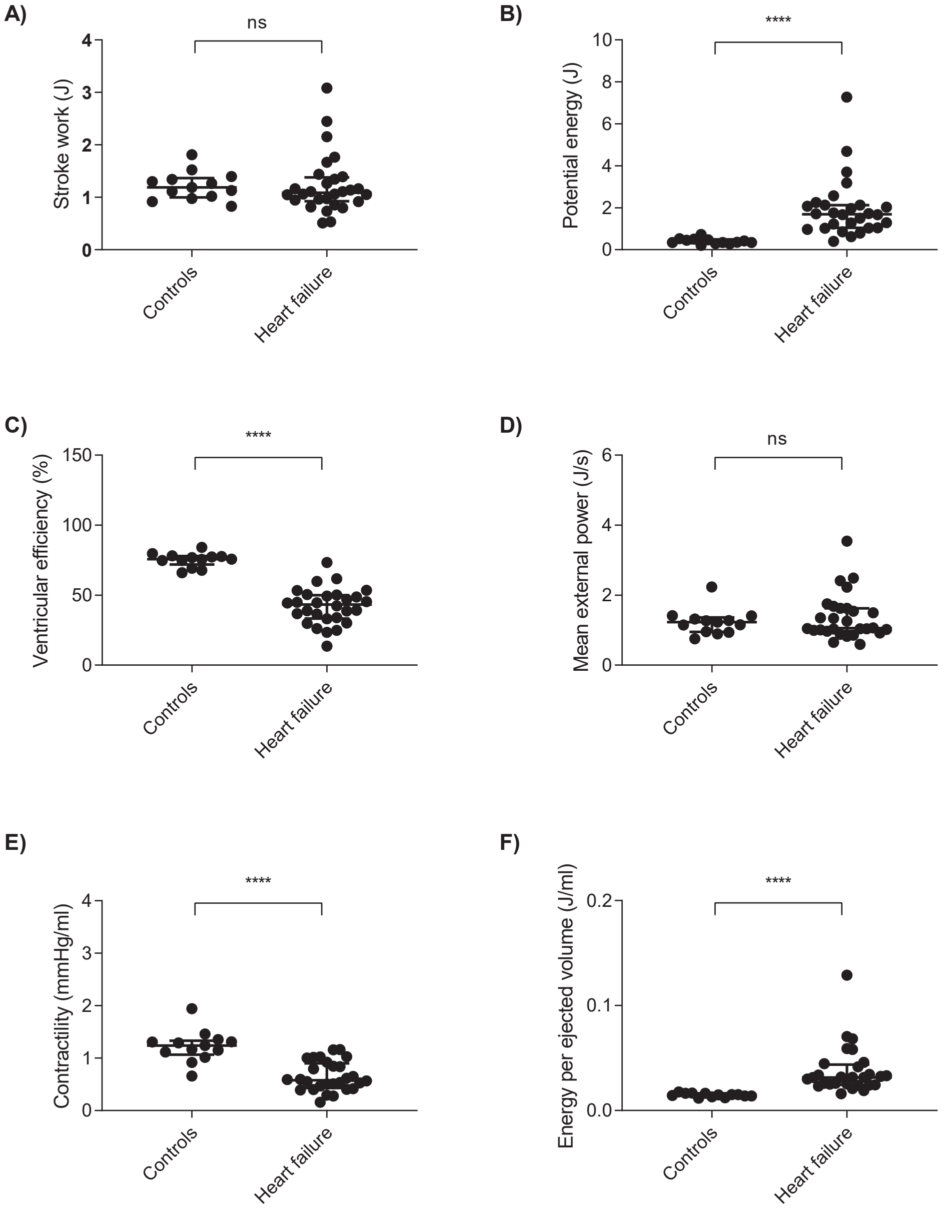

Figure 4.12: Comparison between model derived and *in vivo* measured hemodynamic parameters in healthy controls and heart failure patients. The average parameter of each subject when ranging end-diastolic pressure between 0-15 mmHg are represented as dots. Horizontal lines indicate median and interquartile range for each cohort. The studied hemodynamic parameters are **A**) stroke work, **B**) mechanical potential energy, **C**) ventricular efficiency, **D**) mean external power, **E**) contractility, and **F**) energy per ejected volume. Non significant differences between cohorts are denoted ns, **** indicates $p < 0.0001$.

4.4 Study IV: Ventricular force-length loops

The proposed ventricular force-length loop model was implemented as a module in Segment (http://segment.heiberg.se) and was applicable to both experimental and subject data. Examples of two generated force-length loops are shown in Figure 4.13.

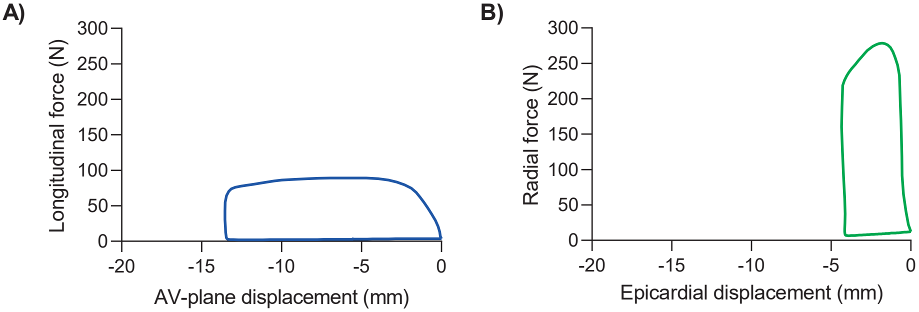

Figure 4.13: Example of generated force-length loops in a heart failure patient. **A**) Longitudinal force-length loop in blue. **B**) Radial force-length loop in green. Longitudinal and radial contributions to stroke work were calculated as the area within each respective loop.

Displacements are presented as negative values, enabling a loop interpretation in analogy with a conventional pressure-volume loop. The bottom right corner at displacement zero marks end diastole, which is followed by the isovolumetric contraction characterized by a steep increase in force but no displacement. There is a decrease in force and increase in displacement during the ejection until end systole, which occurs at the top left corner of the loop. The isovolumetric relaxation is characterized by a fast decrease in force and no displacement. Finally, diastole is characterized by low forces and the tissue returning to its original position at displacement zero.

Longitudinal and radial contribution to stroke work

The concept of longitudinal and radial stroke work was validated by comparing their sums to the total stroke work derived from pressure-volume loops. The excellent agreement and low bias between these measures are shown in Figure 4.14, suggesting that the proposed longitudinal and radial stroke work calculations using ventricular force-length loops holds. The same endocardial contours and LV pressures were used to calculate both force-length loops and PV loops. Force-length loops did however require additional measurements of the AV-plane displacement and epicardial delineations which were not used to derive the PV loop, thus reducing the bias introduced by the overlay in data used in both the proposed and reference methods.

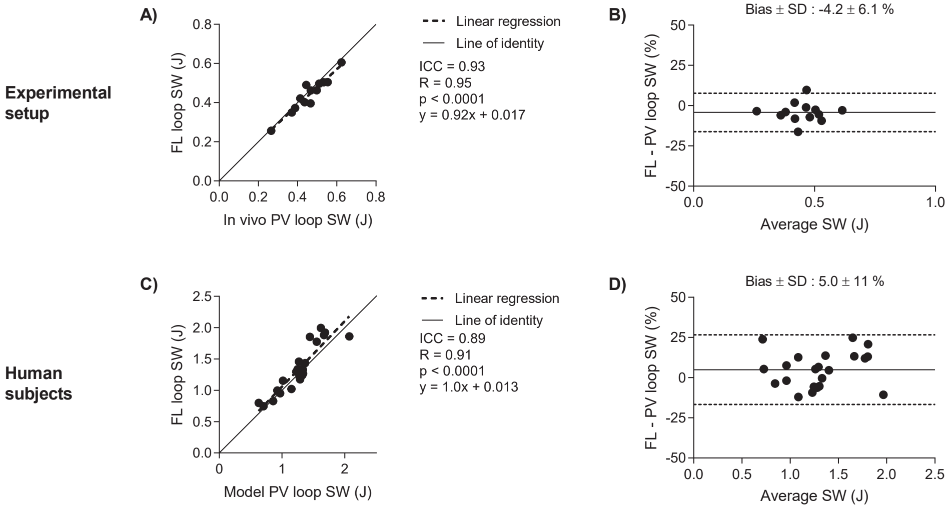

Figure 4.14: Validation of stroke work (SW) derived from force-length (FL) loops compared with SW derived from pressure-volume (PV) loops. Invasively measured PV loops were used in the experimental setup (top row), and noninvasive PV loops in the human subjects (bottom row). The FL loop derived SW was calculated as the sum of the area within the longitudinal and radial FL loops. **A**) Scatter plot for the experimental setup. **B**) Bland-Altman plot for the experimental setup. Solid line represents the bias and dashed lined the limits of agreement. **C**) Scatter plot for human subjects. **D**) Bland-Altman plot for human subjects.

	Longitudinal SW (%)	Radial SW (%)
Swine, baseline	49 ± 8	51 ± 8
Swine, post MI	51 ± 7	49 ± 7
Healthy controls	48 ± 4	52 ± 4
Patients	44 ± 6	56 ± 6

Table 4.5: Longitudinal and radial contribution to stroke work (SW) in swine and man.

Longitudinal and radial pumping were found to contribute approximately equally to the total ventricular stroke work in all cohorts, see Table 4.5. There were no differences in total, longitudinal, or radial stroke work between healthy and diseased in the cohorts, see Table 4.6 and Table 4.7. The finding that longitudinal and radial work contribute equally, and that this equal distribution was maintained between healthy subjects and patients, supports previous finding reported in Study III. Furthermore, Arbab-Zadeh et al has previously reported no differences in stroke work in healthy sedentary seniors and master athletes [148]. The contribution of longitudinal pumping to stroke volume was also maintained at ~60% in healthy subjects, elite athletes, and patients with dilated cardiomyopathy in another study [10]. The slight but non-significant shift in work distribution in healthy controls and patients is due to the dilated ventricles and thus larger radial surface areas, as well as the decreased in AV-plane displacement.

	Baseline	Post-MI	p-value
Total SW (J)	0.42 ± 0.1	0.5 ± 0.1	$p = 0.18$
Longitudinal SW (J)	0.20 ± 0.05	0.25 ± 0.05	$p = 0.14$
Radial SW (J)	0.21 ± 0.06	0.24 ± 0.06	$p = 0.53$

Table 4.6: Quantified stroke work (SW) in the experiments performed at baseline and one week post myocardial infarction (MI). Total SW was derived from experimentally measured pressure-volume loops. Longitudinal and radial SW were derived from their respective force-length loops.

	Controls	Patients	p-value
Total SW (J)	1.3 ± 0.3	1.2 ± 0.4	$p = 0.54$
Longitudinal SW (J)	0.65 ± 0.2	0.60 ± 0.2	$p = 0.58$
Radial SW (J)	0.70 ± 0.2	0.75 ± 0.2	$p = 0.54$

Table 4.7: Quantified stroke work (SW) in healthy controls and patients with ischemic dilated cardiomyopathy. Total SW was derived from noninvasively quantified pressure-volume loops using the method proposed in Study III. Longitudinal and radial SW were derived from their respective force-length loops.

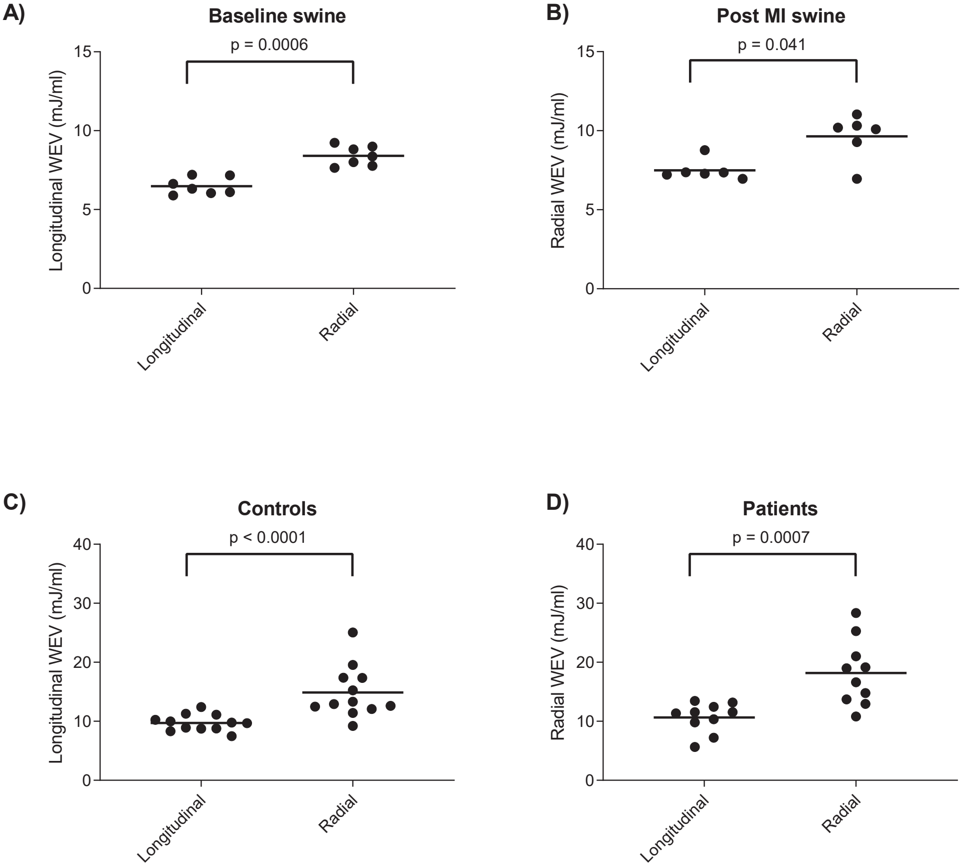

Figure 4.15: Comparison of longitudinal and radial work per ejected volume (WEV) in the experimental setup (top row) and human subjects (bottom row). **A**) Baseline swine. **B**) Swine post myocardial infarction (MI). **C**) Healthy subjects. **D**) Heart failure patients.

Work per ejected volume

With longitudinal pumping mechanics being the major contributor to stroke volume and a reduced AV-plane displacement being an independent predictor of major cardiac events [30], it might at first be surprising that longitudinal and radial pumping contributes equally to stroke work. A more intuitive interpretation might instead be to study the work per ejected volume. The work per ejected volume was lower in longitudinal pumping compared to radial pumping (Figure 4.15), meaning that the longitudinal pumping is more energy efficient in delivering stroke volume. This is explained by the larger portion of stroke volume being generated by the AV-plane displacement, while the same amount of work is required for both pumping mechanisms. The work per ejected volume increased in swine one week post myocardial infarction ($p = 0.014$), meaning that the longitudinal pumping became less energy efficient. Longitudinal pumping did however remain more energy efficient than radial pumping. No difference was observed between controls and patients with dilated ischemic cardiomyopathy. This is explained by the increase in epicardial cross-sectional area in the dilated LV, resulting in a maintained longitudinal contribution to both stroke volume and stroke work, although the AV-plane displacement decreased. Future longitudinal experimental studies where infarcted swine are their own baseline controls might explain this mechanism further. The infarct location is however not expected to impact the global AV-plane displacement within a week of myocardial infarction [149].

Ventricular forces

Peak forces and displacements are summarized in Table 4.8 and Table 4.9. There were differences between controls and patients, but not in the experimental setup. These quantified forces are however not to be regarded as two single global contracting forces facilitating cardiac pumping. On the contrary, the contracting myocardium generates tension and thereby blood pressure. According to Newton's third law, the pressurized blood will then exert a contact force on the myocardium, which is what was computed with the proposed model. A great variety of forces act within the complex myocardial structure, translating from a molecular level to microscopic fiber orientations, and macroscopic anatomical geometries. These forces are thus challenging to measure *in vivo*, and intracardiac forces such as peak driving force, elastic recoil, active relaxation, and hydraulic forces have therefore often been studied in their isolated forms [45, 150–155]. The division of longitudinal and radial forces and their resulting stroke work are thus to be viewed as a piece of a puzzle rather than a global description of the forces behind the intricate cardiac pumping mechanics.

	Baseline	Post-MI	p-value
Peak longitudinal force (N)	31 ± 4	34 ± 5	$p = 0.45$
Peak AVPD (mm)	9.3 ± 1.7	9.9 ± 0.9	$p = 0.63$
Peak radial force (N)	91 ± 12	100 ± 10	$p = 0.23$
Peak average epicardial displacement (mm)	1.6 ± 0.4	1.9 ± 0.5	$p = 0.18$

Table 4.8: Quantified peak forces and displacements in the longitudinal and radial directions, obtained in the experimental cohort performed at baseline and one week post myocardial infarction (MI). AVPD: atrioventricular plane displacement.

	Controls	Patients	p-value
Peak longitudinal force (N)	56 ± 10	86 ± 16	$p < 0.0001$
Peak AVPD (mm)	16 ± 2	9 ± 2	$p < 0.0001$
Peak radial force (N)	188 ± 38	271 ± 45	$p = 0.0003$
Peak average epicardial displacement (mm)	2.4 ± 0.4	1.7 ± 0.5	$p = 0.0011$

Table 4.9: Quantified peak forces and displacements in the longitudinal and radial directions, obtained in healthy controls and patients with dilated ischemic cardiomyopathy. AVPD: atrioventricular plane displacement.

Summary

In summary, Study IV presents a validated method to obtain subject-specific ventricular force-length loops in the longitudinal and radial directions. The method is based on longitudinal and radial tissue displacements as well as the relationship between force, pressure, and area. The generated force-length loops allows for quantification of longitudinal and radial contributions to stroke work, enabling physiological investigations on ventricular energy consumption and efficiency.

Chapter 5

Conclusions

The most damaging phrase in the language is: ”It’s always been done that way.”

Grace Hopper

In this thesis, the following advancements in subject-specific assessment of cardiovascular physiology using CMR have been developed, validated, and demonstrated to be feasible:

- Semi-automatic quantification of the atrioventricular plane displacement (**Study I**)
- Direct measurement of transmitral flow (**Study II**)
- Noninvasive pressure-volume loops (**Study III**)
- Quantification of longitudinal and radial force-length loops (**Study IV**)

The proposed methods and tools in Study I, II and IV require brachial pressure and images which are typically acquired during standard clinical CMR scanning, and adding the sequence proposed in Study II would prolong the protocol by a few minutes. This suggests that the capabilities of CMR in evaluating cardiovascular physiology during a single noninvasive examination haven been expanded, thus getting closer to the reality of CMR as a one-stop-shop.

I didn't want to just know names of things.
I remember really wanting to know how it all worked.

Elizabeth Blackburn

References

[1] World Health Organization. Fact sheet: Cardiovascular diseases (CVDs). 2017.

[2] Salerno M., Sharif B., Arheden H., Kumar A., Axel L., Li D., and Neubauer S. Recent Advances in Cardiovascular Magnetic Resonance: Techniques and Applications. *Circulation. Cardiovascular imaging*, 10(6), 2017.

[3] Blackwell G. The Evolving Role of MRI in the Assessment of Coronary Artery Disease. *The American Journal of Cardiology*, 75(11):74D–78D, 1995.

[4] Poon M., Fuster V., and Fayad Z. Cardiac magnetic resonance imaging: a ”one-stop-shop” evaluation of myocardial dysfunction. *Current opinion in cardiology*, 17 (6):663–70, 2002.

[5] Baritussio A., Scatteia A., and Bucciarelli-Ducci C. Role of cardiovascular magnetic resonance in acute and chronic ischemic heart disease. *The International Journal of Cardiovascular Imaging*, 34(1):67–80, 2018.

[6] Widmaier E. P., Raff H., and Strang K. T. *Vander's Human Physiology The Mechanisms of Body Function*. McGraw-Hill Education, 14th edition, 2016.

[7] Åstrand P.-O., Cuddy T. E., Saltin B., and Stenberg J. Cardiac output during submaximal and maximal work. *Journal of Applied Physiology*, 19(2):268–274, 1964.

[8] Watkins M. W. and LeWinter M. M. Physiologic Role of the Normal Pericardium. *Annual Review of Medicine*, 44(1):171–180, 1993.

[9] Holt J. P. The normal pericardium. *The American Journal of Cardiology*, 26(5): 455–465, 1970.

[10] Carlsson M., Ugander M., Mosen H., Buhre T., and Arheden H. Atrioventricular plane displacement is the major contributor to left ventricular pumping in healthy adults, athletes, and patients with dilated cardiomyopathy. *AJP: Heart and Circulatory Physiology*, 292(3):H1452–H1459, 2006.

[11] Harvey W. *Exercitatio Anatomica de Motu Cordis et Sanguinis in Animalibus*. Frankfurt, 1628.

[12] Ingels N. B. Myocardial fiber architecture and left ventricular function. *Technology and health care : official journal of the European Society for Engineering and Medicine*, 5(1-2):45–52, 1997.

[13] Torrent-Guasp F., Ballester M., Buckberg G. D., Carreras F., Flotats A., Carrió I., Ferreira A., Samuels L. E., and Narula J. Spatial orientation of the ventricular muscle band: Physiologic contribution and surgical implications. *The Journal of Thoracic and Cardiovascular Surgery*, 122(2):389–392, 2001.

[14] Coghlan C. and Hoffman J. Leonardo da Vinci's flights of the mind must continue: cardiac architecture and the fundamental relation of form and function revisited. *European Journal of Cardio-Thoracic Surgery*, 29:S4–S17, 2006.

[15] Greenbaum R. A., Ho S. Y., Gibson D. G., Becker A. E., and Anderson R. H. Left ventricular fibre architecture in man. *Heart*, 45(3):248–263, 1981.

[16] Nielles-Vallespin S., Khalique Z., Ferreira P. F., de Silva R., Scott A. D., Kilner P., McGill L.-A., Giannakidis A., Gatehouse P. D., Ennis D., Aliotta E., Al-Khalil M., Kellman P., Mazilu D., Balaban R. S., Firmin D. N., Arai A. E., and Pennell D. J. Assessment of Myocardial Microstructural Dynamics by In Vivo Diffusion Tensor Cardiac Magnetic Resonance. *Journal of the American College of Cardiology*, 69(6): 661–676, 2017.

[17] Sallin E. A. Fiber Orientation and Ejection Fraction in the Human Left Ventricle. *Biophysical Journal*, 9(7):954–964, 1969.

[18] Arts T., Reneman R. S., and Veenstra P. C. A model of the mechanics of the left ventricle. *Annals of biomedical engineering*, 7(3-4):299–318, 1979.

[19] Henein M. Y. and Gibson D. G. Normal long axis function. *Heart*, 81(2):111–113, 1999.

[20] Henein M. Y. and Gibson D. G. Long axis function in disease. *Heart*, 81(3):229–231, 1999.

[21] Bowman A. W. and Kovács S. J. Left atrial conduit volume is generated by deviation from the constant-volume state of the left heart: a combined MRI-echocardiographic study. *American Journal of Physiology-Heart and Circulatory Physiology*, 286(6):H2416–H2424, 2004.

[22] Steding-Ehrenborg K., Carlsson M., Stephensen S., and Arheden H. Atrial aspiration from pulmonary and caval veins is caused by ventricular contraction and secures 70% of the total stroke volume independent of resting heart rate and heart size. *Clinical Physiology and Functional Imaging*, 33(3):233–240, 2013.

[23] Bowman A. W. and Kovács S. J. Assessment and consequences of the constant-volume attribute of the four-chambered heart. *American Journal of Physiology-Heart and Circulatory Physiology*, 285(5):H2027–H2033, 2003.

[24] Ugander M., Carlsson M., and Arheden H. Short-axis epicardial volume change is a measure of cardiac left ventricular short-axis function, which is independent of myocardial wall thickness. *American Journal of Physiology-Heart and Circulatory Physiology*, 298(2):H530–H535, 2010.

[25] Wandt B. Long-axis contraction of the ventricles: a modern approach, but described already by Leonardo da Vinci. *Journal of the American Society of Echocardiography : official publication of the American Society of Echocardiography*, 13(7):699–706, 2000.

[26] Braunwald E., Zipes D. P., and Libby P. *Heart Disease: A textbook of Cardiovascular Medicine*. Saunders Company, Philadelphia; London, 6th edition, 2001.

[27] Maksuti E. *Imaging and modeling the cardiovascular system*. Universitetsservice US-AB, Stockholm, 2016.

[28] Carlsson M., Cain P., Holmqvist C., Stahlberg F., Lundback S., and Arheden H. Total heart volume variation throughout the cardiac cycle in humans. *American journal of physiology. Heart and circulatory physiology*, 287(1):243–50, 2004.

[29] Carlsson M., Ugander M., Heiberg E., and Arheden H. The quantitative relationship between longitudinal and radial function in left, right, and total heart pumping in humans. *AJP: Heart and Circulatory Physiology*, 293(1):H636–H644, 2007.

[30] Rangarajan V., Chacko S. J., Romano S., Jue J., Jariwala N., Chung J., and Farzaneh-Far A. Left ventricular long axis function assessed during cine-cardiovascular magnetic resonance is an independent predictor of adverse cardiac events. *Journal of Cardiovascular Magnetic Resonance*, 18(1):35, 2016.

[31] Romano S., Judd R. M., Kim R. J., Kim H. W., Klem I., Heitner J. F., Shah D. J., Jue J., and Farzaneh-Far A. Left Ventricular Long-Axis Function Assessed with Cardiac Cine MR Imaging Is an Independent Predictor of All-Cause Mortality in Patients with Reduced Ejection Fraction: A Multicenter Study. *Radiology*, 286(2):452–460, 2018.

[32] Walley K. R. Left ventricular function: time-varying elastance and left ventricular aortic coupling. *Critical Care*, 20(1):270, 2016.

[33] Lee E.-J., Peng J., Radke M., Gotthardt M., and Granzier H. L. Calcium sensitivity and the Frank–Starling mechanism of the heart are increased in titin N2B region-deficient mice. *Journal of Molecular and Cellular Cardiology*, 49(3):449–458, 2010.

[34] Allen D. G. and Kentish J. C. The cellular basis of the length-tension relation in cardiac muscle. *Journal of molecular and cellular cardiology*, 17(9):821–40, 1985.

[35] Kentish J. C., ter Keurs H. E., Ricciardi L., Bucx J. J., and Noble M. I. Comparison between the sarcomere length-force relations of intact and skinned trabeculae from rat right ventricle. Influence of calcium concentrations on these relations. *Circulation Research*, 58(6):755–768, 1986.

[36] Westerhof N., Stergiopulos N., and Noble M. I. *Snapshots of Hemodynamics*. Springer, London, 2nd edition, 2010.

[37] Frank O. On the dynamics of cardiac muscle (Translation). *American Heart Journal*, 58(2):282–317, 1959.

[38] Patterson S. W. and Starling E. H. On the mechanical factors which determine the output of the ventricles. *The Journal of Physiology*, 48(5):357–379, 1914.

[39] Patterson S. W., Piper H., and Starling E. H. The regulation of the heart beat. *The Journal of Physiology*, 48(6):465–513, 1914.

[40] Burkhoff D., Mirsky I., and Suga H. Assessment of systolic and diastolic ventricular properties via pressure-volume analysis: a guide for clinical, translational, and basic researchers. *AJP: Heart and Circulatory Physiology*, 289(2):H501–H512, 2005.

[41] Kass D. A. and Maughan W. L. From 'Emax' to pressure-volume relations: a broader view. *Circulation*, 77(6):1203–12, 1988.

[42] Borlaug B. A. and Kass D. A. Invasive Hemodynamic Assessment in Heart Failure. *Heart Failure Clinics*, 5(2):217–228, 2009.

[43] Arvidsson P. *Physiological aspects on intracardiac blood flow*. Lund, Sweden, 2017.

[44] Noble M. I. M. The Contribution of Blood Momentum to Left Ventricular Ejection in the Dog. *Circulation Research*, 23(5):663–670, 1968.

[45] Helmes M., Trombita´s K., and Granzier H. Titin Develops Restoring Force in Rat Cardiac Myocytes. *Circulation Research*, 79(3):619–626, 1996.

[46] Kovács S. J. Diastolic Function in Heart Failure. *Clinical Medicine Insights: Cardiology*, 9s1:CMC.S18743, 2015.

[47] Kovacs, S. J. J., Barzilai B., and Perez J. E. Evaluation of diastolic function with Doppler echocardiography: the PDF formalism. *Am J Physiol Heart Circ Physiol*, 252(1):178–187, 1987.

[48] Carlhäll C., Wigström L., Heiberg E., Karlsson M., Bolger A. F., and Nylander E. Contribution of mitral annular excursion and shape dynamics to total left ventricular volume change. *American Journal of Physiology-Heart and Circulatory Physiology*, 287 (4):H1836–H1841, 2004.

[49] Zhang W., Chung C. S., Shmuylovich L., and Kovács S. J. Is left ventricular volume during diastasis the real equilibrium volume, and what is its relationship to diastolic suction? *Journal of Applied Physiology*, 105(3):1012–1014, 2008.

[50] Kilner P. J., Henein M. Y., and Gibson D. G. Our tortuous heart in dynamic mode–an echocardiographic study of mitral flow and movement in exercising subjects. *Heart and vessels*, 12(3):103–10, 1997.

[51] Chung C. S. Duration of diastole and its phases as a function of heart rate during supine bicycle exercise. *AJP: Heart and Circulatory Physiology*, 287(5):H2003–H2008, 2004.

[52] Carlsson M. *Aspects on cardiac pumping*. Lund, Sweden, 2007.

[53] Suga H. Total mechanical energy of a ventricle model and cardiac oxygen consumption. *The American journal of physiology*, 236(3):498–505, 1979.

[54] Suga H., Sagawa K., and Shoukas a. a. Load independence of the instantaneous pressure-volume ratio of the canine left ventricle and effects of epinephrine and heart rate on the ratio. *Circulation research*, 32:314–322, 1973.

[55] Sagawa K. The end-systolic pressure-volume relation of the ventricle: definition, modifications and clinical use. *Circulation*, 63(6):1223–1227, 1981.

[56] Stevenson D., Revie J., Chase J., Hann C. E., Shaw G. M., Lambermont B., Ghuysen A., Kolh P., and Desaive T. Algorithmic processing of pressure waveforms to facilitate estimation of cardiac elastance. *BioMedical Engineering OnLine*, 11(1):28, 2012.

[57] Stevenson D., Revie J., Chase J. G., Hann C. E., Shaw G. M., Lambermont B., Ghuysen A., Kolh P., and Desaive T. Beat-to-beat estimation of the continuous left and right cardiac elastance from metrics commonly available in clinical settings. *BioMedical Engineering OnLine*, 11(1):73, 2012.

[58] Oommen B., Karamanoglu M., and Kovács S. J. Modeling Time Varying Elastance: The Meaning of “Load-Independence”. *Cardiovascular Engineering*, 3(4):123–130, 2003.

[59] Georgakopoulos D., Mitzner W. A., Chen C. H., Byrne B. J., Millar H. D., Hare J. M., and Kass D. A. In vivo murine left ventricular pressure-volume relations by miniaturized conductance micromanometry. *The American journal of physiology*, 274 (4 Pt 2):1416–22, 1998.

[60] Senzaki H., Chen C. H., and Kass D. A. Single-beat estimation of end-systolic pressure-volume relation in humans. A new method with the potential for noninvasive application. *Circulation*, 94(10):2497–506, 1996.

[61] Stergiopulos N., Meister J. J., and Westerhof N. Determinants of stroke volume and systolic and diastolic aortic pressure. *The American journal of physiology*, 270(6 Pt 2):2050–9, 1996.

[62] Lankhaar J.-W., Rövekamp F. A., Steendijk P., Faes T. J. C., Westerhof B. E., Kind T., Vonk-Noordegraaf A., and Westerhof N. Modeling the Instantaneous Pressure–Volume Relation of the Left Ventricle: A Comparison of Six Models. *Annals of Biomedical Engineering*, 37(9):1710–1726, 2009.

[63] Broomé M., Maksuti E., Bjällmark A., Frenckner B., and Janerot-Sjöberg B. Closed-loop real-time simulation model of hemodynamics and oxygen transport in the cardiovascular system. *BioMedical Engineering OnLine*, 12(1):69, 2013.

[64] Mynard J. P., Davidson M. R., Penny D. J., and Smolich J. J. A simple, versatile valve model for use in lumped parameter and one-dimensional cardiovascular models. *International Journal for Numerical Methods in Biomedical Engineering*, 28(6-7):626–641, 2012.

[65] Maksuti E., Westerhof N., Westerhof B. E., Broomé M., and Stergiopulos N. Contribution of the Arterial System and the Heart to Blood Pressure during Normal Aging - A Simulation Study. *PloS one*, 11(6):e0157493, 2016.

[66] Casas B., Lantz J., Viola F., Cedersund G., Bolger A. F., Carlhäll C.-J., Karlsson M., and Ebbers T. Bridging the Gap between Measurements and Modelling: A Cardiovascular Functional Avatar. *Scientific Reports*, 7(6214), 2017.

[67] Segers P., Stergiopulos N., and Westerhof N. Quantification of the Contribution of Cardiac and Arterial Remodeling to Hypertension. *Hypertension*, 36(5):760–765, 2000.

[68] Henkel D. M., Redfield M. M., Weston S. A., Gerber Y., and Roger V. L. Death in Heart Failure. *Circulation: Heart Failure*, 1(2):91–97, 2008.

[69] Yancy C. W., Jessup M., Bozkurt B., Butler J., Casey D. E., Drazner M. H., Fonarow G. C., Geraci S. A., Horwich T., Januzzi J. L., Johnson M. R., Kasper E. K., Levy

W. C., Masoudi F. A., McBride P. E., McMurray J. J., Mitchell J. E., Peterson P. N., Riegel B., Sam F., Stevenson L. W., Tang W. W., Tsai E. J., and Wilkoff B. L. 2013 ACCF/AHA Guideline for the Management of Heart Failure. *Circulation*, 128(16), 2013.

[70] Nagueh S. F., Mikati I., Kopelen H. A., Middleton K. J., Quiñones M. A., and Zoghbi W. A. Doppler estimation of left ventricular filling pressure in sinus tachycardia. A new application of tissue doppler imaging. *Circulation*, 98(16):1644–50, 1998.

[71] Nagueh S. F., Smiseth O. A., Appleton C. P., Byrd B. F., Dokainish H., Edvardsen T., Flachskampf F. A., Gillebert T. C., Klein A. L., Lancellotti P., Marino P., Oh J. K., Alexandru Popescu B., and Waggoner A. D. Recommendations for the Evaluation of Left Ventricular Diastolic Function by Echocardiography: An Update from the American Society of Echocardiography and the European Association of Cardiovascular Imaging. *European Heart Journal – Cardiovascular Imaging*, 17(12): 1321–1360, 2016.

[72] Thygesen K., Alpert J. S., Jaffe A. S., Simoons M. L., Chaitman B. R., and White H. D. Third Universal Definition of Myocardial Infarction. *Circulation*, 126(16): 2020–2035, 2012.

[73] Baumgartner H., Falk V., Bax J. J., De Bonis M., Hamm C., Holm P. J., Iung B., Lancellotti P., Lansac E., Rodriguez Muñoz D., Rosenhek R., Sjögren J., Tornos Mas P., Vahanian A., Walther T., Wendler O., Windecker S., Zamorano J. L., and ESC Scientific Document Group. 2017 ESC/EACTS Guidelines for the management of valvular heart disease. *European heart journal*, 38(36):2739–2791, 2017.

[74] Srichai M. B., Lim R. P., Wong S., and Lee V. S. Cardiovascular Applications of Phase-Contrast MRI. *American Journal of Roentgenology*, 192(3):662–675, 2009.

[75] Lauterbur P. C. Image Formation by Induced Local Interactions: Examples Employing Nuclear Magnetic Resonance. *Nature*, 242(5394):190–191, 1973.

[76] Mansfield P. Multi-planar image formation using NMR spin echoes. *Journal of Physics C: Solid State Physics*, 10(3):L55–L58, 1977.

[77] Mansfield P. and Pykett I. Biological and medical imaging by NMR. *Journal of Magnetic Resonance (1969)*, 29(2):355–373, 1978.

[78] Bloch F. Nuclear Induction. *Physical Review*, 70(7-8):460–474, 1946.

[79] Lanzer P., Botvinick E. H., Schiller N. B., Crooks L. E., Arakawa M., Kaufman L., Davis P. L., Herfkens R., Lipton M. J., and Higgins C. B. Cardiac imaging using gated magnetic resonance. *Radiology*, 150(1):121–127, 1984.

[80] Ehman R., McNamara M., Pallack M., Hricak H., and Higgins C. Magnetic resonance imaging with respiratory gating: techniques and advantages. *American Journal of Roentgenology*, 143(6):1175–1182, 1984.

[81] Sayin O., Saybasili H., Zviman M. M., Griswold M., Halperin H., Seiberlich N., and Herzka D. A. Real-time free-breathing cardiac imaging with self-calibrated through-time radial GRAPPA. *Magnetic Resonance in Medicine*, 77(1):250–264, 2017.

[82] Manke D., Nehrke K., and Börnert P. Novel prospective respiratory motion correction approach for free-breathing coronary MR angiography using a patient-adapted affine motion model. *Magnetic Resonance in Medicine*, 50(1):122–131, 2003.

[83] Steeden J. A., Kowalik G. T., Tann O., Hughes M., Mortensen K. H., and Muthurangu V. Real-time assessment of right and left ventricular volumes and function in children using high spatiotemporal resolution spiral bSSFP with compressed sensing. *Journal of Cardiovascular Magnetic Resonance*, 20(1):79, 2018.

[84] Dyverfeldt P., Bissell M., Barker A. J., Bolger A. F., Carlhäll C.-J., Ebbers T., Francios C. J., Frydrychowicz A., Geiger J., Giese D., Hope M. D., Kilner P. J., Kozerke S., Myerson S., Neubauer S., Wieben O., and Markl M. 4D flow cardiovascular magnetic resonance consensus statement. *Journal of cardiovascular magnetic resonance : official journal of the Society for Cardiovascular Magnetic Resonance*, 17(1):72, 2015.

[85] Engblom H., Tufvesson J., Jablonowski R., Carlsson M., Aletras A. H., Hoffmann P., Jacquier A., Kober F., Metzler B., Erlinge D., Atar D., Arheden H., and Heiberg E. A new automatic algorithm for quantification of myocardial infarction imaged by late gadolinium enhancement cardiovascular magnetic resonance: experimental validation and comparison to expert delineations in multi-center, multi-vendor patient data. *Journal of Cardiovascular Magnetic Resonance*, 18(1):27, 2016.

[86] Peters D. C., Wylie J. V., Hauser T. H., Kissinger K. V., Botnar R. M., Essebag V., Josephson M. E., and Manning W. J. Detection of Pulmonary Vein and Left Atrial Scar after Catheter Ablation with Three-dimensional Navigator-gated Delayed Enhancement MR Imaging: Initial Experience 1. *Radiology*, 243(3):690–695, 2007.

[87] Everett R., Stirrat C., Semple S., Newby D., Dweck M., and Mirsadraee S. Assessment of myocardial fibrosis with T1 mapping MRI. *Clinical Radiology*, 71(8): 768–778, 2016.

[88] Aletras A. H., Kellman P., Derbyshire J. A., and Arai A. E. ACUT2E TSE-SSFP: A hybrid method for T2-weighted imaging of edema in the heart. *Magnetic Resonance in Medicine*, 59(2):229–235, 2008.

[89] van Ewijk P. A., Schrauwen-Hinderling V. B., Bekkers S. C. A. M., Glatz J. F. C., Wildberger J. E., and Kooi M. E. MRS: a noninvasive window into cardiac metabolism. *NMR in Biomedicine*, 28(7):747–766, 2015.

[90] Carr J. C., Simonetti O., Bundy J., Li D., Pereles S., and Finn J. P. Cine MR angiography of the heart with segmented true fast imaging with steady-state precession. *Radiology*, 219(3):828–34, 2001.

[91] Nayler G. L., Firmin D. N., and Longmore D. B. Blood Flow Imaging by Cine Magnetic Resonance. *Journal of Computer Assisted Tomography*, 10(5):715–722, 1986.

[92] Nayak K. S., Nielsen J.-F., Bernstein M. A., Markl M., D. Gatehouse P., M. Botnar R., Saloner D., Lorenz C., Wen H., S. Hu B., Epstein F. H., N. Oshinski J., and Raman S. V. Cardiovascular magnetic resonance phase contrast imaging. *Journal of Cardiovascular Magnetic Resonance*, 17(1):71, 2015.

[93] Hahn E. L. Detection of sea-water motion by nuclear precession. *Journal of Geophysical Research*, 65(2):776–777, 1960.

[94] Gatehouse P. D., Rolf M. P., Graves M. J., Hofman M. B., Totman J., Werner B., Quest R. A., Liu Y., von Spiczak J., Dieringer M., Firmin D. N., van Rossum A., Lombardi M., Schwitter J., Schulz-Menger J., and Kilner P. J. Flow measurement by cardiovascular magnetic resonance: a multi-centre multi-vendor study of background phase offset errors that can compromise the accuracy of derived regurgitant or shunt flow measurements. *Journal of Cardiovascular Magnetic Resonance*, 12(1): 5, 2010.

[95] Ebbers T., Wigström L., Bolger A. F., Engvall J., and Karlsson M. Estimation of relative cardiovascular pressures using time-resolved three-dimensional phase contrast MRI. *Magnetic resonance in medicine*, 45(5):872–9, 2001.

[96] Buyens F., Jolivet O., De Cesare A., Bittoun J., Herment A., Tasu J.-P., and Mousseaux E. Calculation of left ventricle relative pressure distribution in MRI using acceleration data. *Magnetic Resonance in Medicine*, 53(4):877–884, 2005.

[97] Krittian S. B., Lamata P., Michler C., Nordsletten D. A., Bock J., Bradley C. P., Pitcher A., Kilner P. J., Markl M., and Smith N. P. A finite-element approach to the direct computation of relative cardiovascular pressure from time-resolved MR velocity data. *Medical Image Analysis*, 16(5):1029–1037, 2012.

[98] Quail M. A., Steeden J. A., Knight D., Segers P., Taylor A. M., and Muthurangu V. Development and validation of a novel method to derive central aortic systolic pressure from the MR aortic distension curve. *Journal of Magnetic Resonance Imaging*, 40(5):1064–1070, 2014.

[99] Michaud M., Maurin V., Simon M., Chauvel C., Bogino E., and Abergel E. Patients with high left ventricular filling pressure may be missed applying 2016 echo guidelines: a pilot study. *The International Journal of Cardiovascular Imaging*, 2019.

[100] Park J.-H. and Marwick T. H. Use and Limitations of E/e' to Assess Left Ventricular Filling Pressure by Echocardiography. *Journal of Cardiovascular Ultrasound*, 19(4): 169, 2011.

[101] Nagueh S. F. Non-invasive assessment of left ventricular filling pressure. *European Journal of Heart Failure*, 20(1):38–48, 2018.

[102] Pickering T. G. Recommendations for Blood Pressure Measurement in Humans and Experimental Animals: Part 1: Blood Pressure Measurement in Humans: A Statement for Professionals From the Subcommittee of Professional and Public Education of the American Heart Association Cou. *Circulation*, 111(5):697–716, 2005.

[103] Yunus N. A. M., Halin I. A., Sulaiman N., Ismail N. F., and Sheng O. K. Valuation on mems pressure sensors and device applications. *International Journal of Electrical, Computer, Energetic, Electronic and Communication Engineering*, 9(8), 2015.

[104] Baan J., Jong T. T. A., Kerkhof P. L. M., Moene R. J., van Dijk A. D., van der Velde E. T., and Koops J. Continuous stroke volume and cardiac output from intraventricular dimensions obtained with impedance catheter. *Cardiovascular Research*, 15(6):328–334, 1981.

[105] Salo R. W., Wallner T. G., and Pederson B. D. Measurement of Ventricular Volume by Intracardiac Impedance: Theoretical and Empinrcal Approaches. *IEEE Transactions on Biomedical Engineering*, BME-33(2):189–195, 1986.

[106] Nielsen J. M., Kristiansen S. B., Ringgaard S., Nielsen T. T., Flyvbjerg A., Redington A. N., and Bøtker H. E. Left ventricular volume measurement in mice by conductance catheter: evaluation and optimization of calibration. *American Journal of Physiology-Heart and Circulatory Physiology*, 293(1):H534–H540, 2007.

[107] Chia-Ling Wei, Valvano J., Feldman M., Altman D., Kottam A., Raghavan K., Fernandez D., Reyes M., Escobedo D., and Pearce J. Evidence of Time-Varying Myocardial Contribution by In Vivo Magnitude and Phase Measurement in Mice. In *The 26th Annual International Conference of the IEEE Engineering in Medicine and Biology Society*, volume 4, pages 3674–3677. IEEE, 2004.

[108] Ortega R., Connor C., Kotova F., Deng W., and Lacerra C. Use of Pressure Transducers. *New England Journal of Medicine*, 376(14):e26, 2017.

[109] Schulz-Menger J., Bluemke D. A., Bremerich J., Flamm S. D., Fogel M. A., Friedrich M. G., Kim R. J., von Knobelsdorff-Brenkenhoff F., Kramer C. M., Pennell D. J., Plein S., and Nagel E. Standardized image interpretation and post processing in cardiovascular magnetic resonance: Society for Cardiovascular Magnetic Resonance (SCMR) Board of Trustees Task Force on Standardized Post Processing. *Journal of Cardiovascular Magnetic Resonance*, 15(1):35, 2013.

[110] Leng S., Zhao X.-D., Huang F.-Q., Wong J.-I., Su B.-Y., Allen J. C., Kassab G. S., Tan R.-S., and Zhong L. Automated quantitative assessment of cardiovascular magnetic resonance-derived atrioventricular junction velocities. *American Journal of Physiology - Heart and Circulatory Physiology*, 309(11):H1923–H1935, 2015.

[111] Saba S. G., Chung S., Bhagavatula S., Donnino R., Srichai M. B., Saric M., Katz S. D., and Axel L. A novel and practical cardiovascular magnetic resonance method to quantify mitral annular excursion and recoil applied to hypertrophic cardiomyopathy. *Journal of Cardiovascular Magnetic Resonance*, 16(1):35, 2014.

[112] Maffessanti F., Gripari P., Pontone G., Andreini D., Bertella E., Mushtaq S., Tamborini G., Fusini L., Pepi M., and Caiani E. G. Three-dimensional dynamic assessment of tricuspid and mitral annuli using cardiovascular magnetic resonance. *European Heart Journal - Cardiovascular Imaging*, 14(10):986–995, 2013.

[113] Ito S., McElhinney D. B., Adams R., Bhatla P., Chung S., and Axel L. Preliminary Assessment of Tricuspid Valve Annular Velocity Parameters by Cardiac Magnetic Resonance Imaging in Adults with a Volume-Overloaded Right Ventricle: Comparison of Unrepaired Atrial Septal Defect and Repaired Tetralogy of Fallot. *Pediatric Cardiology*, 36(6):1294–1300, 2015.

[114] Leng S., Jiang M., Zhao X.-D., Allen J. C., Kassab G. S., Ouyang R.-Z., Tan J.-L., He B., Tan R.-S., and Zhong L. Three-Dimensional Tricuspid Annular Motion Analysis from Cardiac Magnetic Resonance Feature-Tracking. *Annals of Biomedical Engineering*, 44(12):3522–3538, 2016.

[115] Wu V., Chyou J. Y., Chung S., Bhagavatula S., and Axel L. Evaluation of diastolic function by three-dimensional volume tracking of the mitral annulus with cardiovascular magnetic resonance: comparison with tissue Doppler imaging. *Journal of Cardiovascular Magnetic Resonance*, 16(1):71, 2014.

[116] Leng S., Zhang S., Jiang M., Zhao X., Wu R., Allen J., He B., Tan R. S., and Zhong L. Imaging 4D morphology and dynamics of mitral annulus in humans using cardiac cine MR feature tracking. *Scientific Reports*, 8(1):81, 2018.

[117] Uretsky S., Gillam L., Lang R., Chaudhry F. A., Argulian E., Supariwala A., Gurram S., Jain K., Subero M., Jang J. J., Cohen R., and Wolff S. D. Discordance

between echocardiography and MRI in the assessment of mitral regurgitation severity: a prospective multicenter trial. *Journal of the American College of Cardiology*, 65 (11):1078–88, 2015.

[118] Mehta N. K., Kim J., Siden J. Y., Rodriguez-Diego S., Alakbarli J., Di Franco A., and Weinsaft J. W. Utility of cardiac magnetic resonance for evaluation of mitral regurgitation prior to mitral valve surgery. *Journal of Thoracic Disease*, 9(S4):S246–S256, 2017.

[119] Kozerke S., Scheidegger M. B., Pedersen E. M., and Boesiger P. Heart motion adapted cine phase-contrast flow measurements through the aortic valve. *Magnetic resonance in medicine*, 42(5):970–8, 1999.

[120] Kozerke S., Schwitter J., Pedersen E. M., and Boesiger P. Aortic and mitral regurgitation: quantification using moving slice velocity mapping. *Journal of magnetic resonance imaging : JMRI*, 14(2):106–12, 2001.

[121] Westenberg J. J. M., Roes S. D., Ajmone Marsan N., Binnendijk N. M. J., Doornbos J., Bax J. J., Reiber J. H. C., de Roos A., and van der Geest R. J. Mitral valve and tricuspid valve blood flow: accurate quantification with 3D velocity-encoded MR imaging with retrospective valve tracking. *Radiology*, 249(3):792–800, 2008.

[122] Calkoen E. E., Westenberg J. J., Kroft L. J., Blom N. A., Hazekamp M. G., Rijlaarsdam M. E., Jongbloed M. R., de Roos A., and Roest A. A. Characterization and quantification of dynamic eccentric regurgitation of the left atrioventricular valve after atrioventricular septal defect correction with 4D Flow cardiovascular magnetic resonance and retrospective valve tracking. *Journal of Cardiovascular Magnetic Resonance*, 17(1):18, 2015.

[123] Calkoen E. E., Roest A. A., Kroft L. J., van der Geest R. J., Jongbloed M. R., van den Boogaard P. J., Blom N. A., Hazekamp M. G., de Roos A., and Westenberg J. J. Characterization and improved quantification of left ventricular inflow using streamline visualization with 4DFlow MRI in healthy controls and patients after atrioventricular septal defect correction. *Journal of Magnetic Resonance Imaging*, 41(6):1512–1520, 2015.

[124] Dowsey A. W., Keegan J., Lerotic M., Thom S., Firmin D., and Yang G.-Z. Motion-compensated MR valve imaging with COMB tag tracking and super-resolution enhancement. *Medical Image Analysis*, 11(5):478–491, 2007.

[125] Kuhtz-Buschbeck J. P., Drake-Holland A., Noble M. I., Lohff B., and Schaefer J. Rediscovery of Otto Frank's contribution to science. *Journal of Molecular and Cellular Cardiology*, 119:96–103, 2018.

[126] Bastos M. B., Burkhoff D., Maly J., Daemen J., den Uil C. A., Ameloot K., Lenzen M., Mahfoud F., Zijlstra F., Schreuder J. J., and Van Mieghem N. M. Invasive left ventricle pressure–volume analysis: overview and practical clinical implications. *European Heart Journal*, 2019.

[127] Atar D., Arheden H., Berdeaux A., Bonnet J.-L., Carlsson M., Clemmensen P., Cuvier V., Danchin N., Dubois-Rande J.-L., Engblom H., Erlinge D., Firat H., Halvorsen S., Hansen H. S., Hauke W., Heiberg E., Koul S., Larsen A.-I., Le Corvoisier P., Nordrehaug J. E., Paganelli F., Pruss R. M., Rousseau H., Schaller S., Sonou G., Tuseth V., Veys J., Vicaut E., and Jensen S. E. Effect of intravenous TRO40303 as an adjunct to primary percutaneous coronary intervention for acute ST-elevation myocardial infarction: MITOCARE study results. *European Heart Journal*, 36(2):112–119, 2015.

[128] Steding K., Engblom H., Buhre T., Carlsson M., Mosén H., Wohlfart B., and Arheden H. Relation between cardiac dimensions and peak oxygen uptake. *Journal of Cardiovascular Magnetic Resonance*, 12(1):8, 2010.

[129] Steding-Ehrenborg K., Boushel R. C., Calbet J. A., Åkeson P., and Mortensen S. P. Left ventricular atrioventricular plane displacement is preserved with lifelong endurance training and is the main determinant of maximal cardiac output. *The Journal of Physiology*, 593(23):5157–5166, 2015.

[130] Arvidsson P. M., Toger J., Heiberg E., Carlsson M., and Arheden H. Quantification of left and right atrial kinetic energy using four-dimensional intracardiac magnetic resonance imaging flow measurements. *Journal of Applied Physiology*, 114(10):1472–1481, 2013.

[131] Arvidsson P. M., Kovács S. J., Töger J., Borgquist R., Heiberg E., Carlsson M., and Arheden H. Vortex ring behavior provides the epigenetic blueprint for the human heart. *Scientific Reports*, 6(1):22021, 2016.

[132] Nordlund D., Kanski M., Jablonowski R., Koul S., Erlinge D., Carlsson M., Engblom H., Aletras A. H., and Arheden H. Experimental validation of contrast-enhanced SSFP cine CMR for quantification of myocardium at risk in acute myocardial infarction. *Journal of Cardiovascular Magnetic Resonance*, 19(1):12, 2017.

[133] Heiberg E., Sjögren J., Ugander M., Carlsson M., Engblom H., and Arheden H. Design and validation of Segment - freely available software for cardiovascular image analysis. *BMC Medical Imaging*, 10(1):1, 2010.

[134] Tufvesson J., Hedström E., Steding-ehrenborg K., Carlsson M., Arheden H., and Heiberg E. Validation and Development of a New Automatic Algorithm for Time-Resolved Segmentation of the Left Ventricle in Magnetic Resonance Imaging. 2015.

[135] Bidhult S., Hedström E., Carlsson M., Töger J., Steding-Ehrenborg K., Arheden H., Aletras A. H., and Heiberg E. A new vessel segmentation algorithm for robust blood flow quantification from two-dimensional phase-contrast magnetic resonance images. *Clinical physiology and functional imaging*, 2019.

[136] Lewis J. P. Fast normalized cross-correlation. *Vision interface*, 10(1), 1995.

[137] Kayser H. W., Stoel B. C., van der Wall E. E., van der Geest R. J., and de Roos A. MR velocity mapping of tricuspid flow: correction for through-plane motion. *Journal of magnetic resonance imaging : JMRI*, 7(4):669–73, 1997.

[138] Kelly R. P., Ting C. T., Yang T. M., Liu C. P., Maughan W. L., Chang M. S., and Kass D. A. Effective arterial elastance as index of arterial vascular load in humans. *Circulation*, 86(2):513–521, 1992.

[139] Bland J. M. and Altman D. G. Statistical methods for assessing agreement between two methods of clinical measurement. *Lancet (London, England)*, 1(8476):307–10, 1986.

[140] LeBreton J. M. and Senter J. L. Answers to 20 Questions About Interrater Reliability and Interrater Agreement. *Organizational Research Methods*, 11(4):815–852, 2008.

[141] Seemann F., Baldassarre L. A., Llanos-Chea F., Gonzales R. A., Grunseich K., Hu C., Sugeng L., Meadows J., Heiberg E., and Peters D. C. Assessment of diastolic function and atrial remodeling by MRI - validation and correlation with echocardiography and filling pressure. *Physiological Reports*, 6(17):e13828, 2018.

[142] Arheden H., Saeed M., Törnqvist E., Lund G., Wendland M. F., Higgins C. B., and Ståhlberg F. Accuracy of segmented MR velocity mapping to measure small vessel pulsatile flow in a phantom simulating cardiac motion. *Journal of Magnetic Resonance Imaging*, 13(5):722–728, 2001.

[143] Chen C. H., Nevo E., Fetics B., Pak P. H., Yin F. C., Maughan W. L., and Kass D. A. Estimation of central aortic pressure waveform by mathematical transformation of radial tonometry pressure. Validation of generalized transfer function. *Circulation*, 95(7):1827–36, 1997.

[144] Claessens T. E. Nonlinear isochrones in murine left ventricular pressure-volume loops: how well does the time-varying elastance concept hold? *AJP: Heart and Circulatory Physiology*, 290(4):H1474–H1483, 2005.

[145] Heerdt P. M., Korfhagen S., Ezz H., and Oromendia C. Accuracy of a Simulation Algorithm for Modelling LV Contractility, Diastolic Capacitance, and Energetics Using Data Available From Common Hemodynamic Monitors and Echocardiography. *Journal of Cardiothoracic and Vascular Anesthesia*, 32(1):381–388, 2018.

[146] Ross J. and Braunwald E. The study of left ventricular function in man by increasing resitance to ventricular ejection with angiotensin. *Circulation*, 29:739–49, 1964.

[147] Majid P. A., Sharma B., and Taylor S. H. Phentolamine for vasodilator treatment of severe heart-failure. *Lancet (London, England)*, 2(7727):719–24, 1971.

[148] Arbab-Zadeh A. Effect of Aging and Physical Activity on Left Ventricular Compliance. *Circulation*, 110(13):1799–1805, 2004.

[149] Pahlm U., Seemann F., Engblom H., Gyllenhammar T., Halvorsen S., Hansen H. S., Erlinge D., Atar D., Heiberg E., Arheden H., and Carlsson M. Longitudinal left ventricular function is globally depressed within a week of STEMI. *Clinical Physiology and Functional Imaging*, 38(6):1029–1037, 2018.

[150] Maksuti E., Carlsson M., Arheden H., Kovács S. J., Broomé M., and Ugander M. Hydraulic forces contribute to left ventricular diastolic filling. *Scientific Reports*, 7 (1):43505, 2017.

[151] Arvidsson P. M., Töger J., Carlsson M., Steding-Ehrenborg K., Pedrizzetti G., Heiberg E., and Arheden H. Left and right ventricular hemodynamic forces in healthy volunteers and elite athletes assessed with 4D flow magnetic resonance imaging. *American Journal of Physiology - Heart and Circulatory Physiology*, 312(2):H314–H328, 2017.

[152] Strobeck J. E. and Sonnenblick E. H. Myocardial and ventricular function. Part I: Isolated muscle. *Herz*, 6(5):261–74, 1981.

[153] Pedrizzetti G., Arvidsson P. M., Töger J., Borgquist R., Domenichini F., Arheden H., and Heiberg E. On estimating intraventricular hemodynamic forces from endocardial dynamics: A comparative study with 4D flow MRI. *Journal of Biomechanics*, 2017.

[154] Shmuylovich L. and Kovács S. J. Load-independent index of diastolic filling: model-based derivation with in vivo validation in control and diastolic dysfunction subjects. *Journal of Applied Physiology*, 101(1):92–101, 2006.

[155] Opdahl A., Remme E. W., Helle-Valle T., Lyseggen E., Vartdal T., Pettersen E., Edvardsen T., and Smiseth O. A. Determinants of left ventricular early-diastolic lengthening velocity: independent contributions from left ventricular relaxation, restoring forces, and lengthening load. *Circulation*, 119(19):2578–86, 2009.

Part II

Research papers

Author contributions

	Study design	Ethical application	Method development	MR scanning	Animal experiments	Data analysis	Statistics	Figures and tables	Interpretation of results	Preparation of manuscript	Revision of manuscript	Reply to reviewers
Study I	2	0	3	0	-	2	3	3	3	3	3	3
Study II	3	0	2	3	-	3	3	3	3	3	3	3
Study III	3	0	3	2	3	3	3	3	3	3	3	3
Study IV	3	0	3	2	3	3	3	3	3	3	-	-

Not applicable	-
No contribution	0
Limited contribution	1
Moderate contribution	2
Significant contribution	3

Study I

Active participation in the study design. Designed and implemented the algorithm, performed the parameter optimization, performed time-resolved AV-plane measurements in the training and test set, performed the inter-observer and intra-observer analysis, performed statistical analysis, analyzed the results, prepared figures and tables, and drafted the manuscript.

Study II

Participated actively in the sequence implementation and study design, implemented the image post-processing, performed MR scanning on healthy controls and patients, designed phantom and performed phantom experiments, performed image analysis, performed statistical analysis, analyzed the results, prepared figures and tables, and drafted the manuscript. Was responsible for the continuous contact with the international collaboration.

Study III

Active participation in conceiving and designing the study. Designed and implemented the model, performed parameter optimization, performed time-resolved left ventricular delineations in the validation set, collected the experimental pressure data in the validation set, performed statistical analysis, analyzed all results, prepared figures and tables, and drafted the manuscript.

Study IV

Conceived and designed the study. Designed and implemented the model, performed time-resolved AV-plane measurements, performed time-resolved left ventricular delineations in the experimental data set and in part of the human data set, collected the experimental pressure data, performed part of the experimental MR scanning, analyzed all results, performed the statistical analysis, prepared figures and tables, and drafted the manuscript.

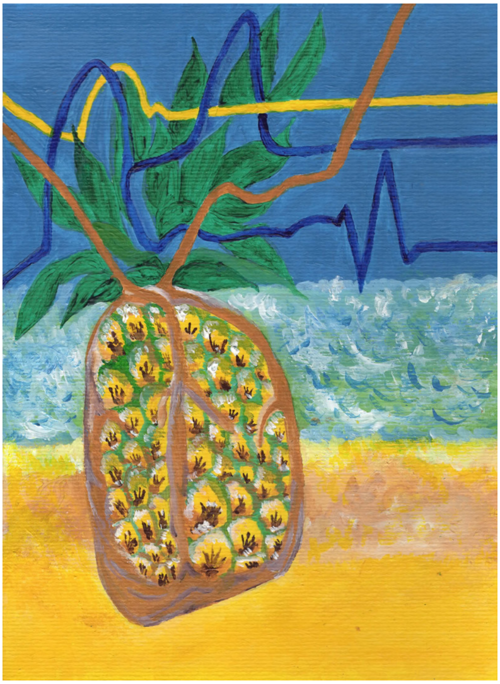

"Physiological samba"
Artist: Andrea Pettersson

Printed by Tryckeriet i E-huset, Lund 2019

LUND
UNIVERSITY

Doctoral Dissertation
ISBN: 978-91-7895-328-8 (print)
ISBN: 978-91-7895-329-5 (pdf)
ISRN: LUTEDX/TEEM – 1120 – SE
Report-nr: 5/19